RHEO-NMR AND SYNCHROTRON X-RAY DIFFRACTION CHARACTERIZATION OF NANOSTRUCTURES OF TRIGLYCERIDES CRYSTALLIZING FROM SOLUTIONS

by

Mengyu Li

Submitted in partial fulfilment of the requirements
for the degree of Master of Science

at

Dalhousie University
Halifax, Nova Scotia
April 2011

DALHOUSIE UNIVERSITY

DEPARTMENT OF PROCESS ENIGINEERING AND APPLIED SCIENCE

The undersigned hereby certify that they have read and recommend to the Faculty of Graduate Studies for acceptance a thesis entitled "RHEO-NMR AND SYNCHROTRON X-RAY DIFFRACTION CHARACTERIZETION OF NANOSTRUCTURES OF TRIGLYCERIDES CRYSTALLIZING FROM SOLUTIONS" by Mengyu Li in partial fulfilment of the requirements for the degree of Master of Science.

Dated: 20, April, 2011

Supervisor: _____

Readers: _____

_____

_____

DALHOUSIE UNIVERSITY

DATE: 20, April, 2011

AUTHOR: Mengyu Li

TITLE: RHEO-NMR AND SYNCHROTRON X-RAY DIFFRACTION CHARACTERIZATION OF NANOSTRUCTURES OF TRIGLYCERIDES CRYSTALLIZING FROM SOLUTIONS

DEPARTMENT OR SCHOOL: Department of Process Engineering and Applied Science

DEGREE: MSc. CONVOCATION: October YEAR: 2011

_____

Signature of Author

TABLE OF CONTENTS

LIST OF TABLES

LIST OF FIGURES

ABSTRACT

The characteristics of crystallized fats depend on their solid fraction (SF) and fractal structures, which are affected by shear during crystallization. Binary mixtures of trilaurin (LLL) and trimyristin (MMM) diluted in triolein were used as samples. Pure diluted LLL and MMM were also studied. Samples were examined at different crystallization temperatures either statically or at shear rates of 800, 80, and $8s^{-1}$. The sample cell combined a rheometer with a nuclear magnetic resonance (NMR) device to measure SF value and apparent viscosity. The measurements were compared to equations that describe the dependency of viscosity on solid volume fraction, to understand the effect of crystallites orientation at higher shear rates. Phase transitions during crystallization were observed by time-resolved synchrotron X-ray diffraction under similar conditions. Shear induced a strong reduction in phase onset and transition time and variations in phase distributions and the crystal size.

LIST OF ABBREVIATIONS AND SYMBOLS USED

ADC	analog-to-digital converter
ATT	attenuation of the NMR signal input
CCD	charge-coupled device
DSC	differential scanning calorimetry
FID	free induction decay
FOT	fiber optic temperature sensor
FWHM	full width at half maximum
LD	lamellar distance
LLL	trilaurin
LS	liquid signal
MMM	trimyristin
NMR	nuclear magnetic resonance
OOO	triolein
PID	proportional-integral–derivative
PLM	polarized light microscopy
RF	radio frequency
SAXD	small angle X-ray diffraction
SF	solid fraction

SF_{max}	maximum solid fraction at the end of crystallization
SR-XRD	synchrotron radiation X-ray diffraction
SBC	solid background signal
SS	solid signal
TAG	triglycerides
TD-NMR	time domain nuclear magnetic resonance
TEC	thermoelectric cooler
XRD	X-ray diffraction
WAXD	wide angle X-ray diffraction
LLL40	pure trilaurin diluted with 60% triolein by weight to obtain sample with 40% solid
3L7M40	30% trilaurin: 70% trimyristin binary triglyceride mixture diluted with 60% triolein by weight to obtain sample with 40% solid
5L5M40	50% trilaurin: 50% trimyristin binary triglyceride mixture diluted with 60% triolein by weight to obtain sample with 40% solid
7L3M40	70% trilaurin: 30% trimyristin binary triglyceride mixture diluted with 60% triolein by weight to obtain sample with 40% solid
7L3M60	70% trilaurin: 30% trimyristin binary triglyceride mixture diluted with 40% triolein by weight to obtain sample with 60% solid
7L3M100	70% trilaurin: 30% trimyristin binary triglyceride mixture
MMM40	pure trimyristin diluted with 60% triolein by weight to obtain sample with 40% solid
MMM100	pure trimyristin sample

Φ_c	crystalline fraction developed at time (t)
k	rate constant of Avrami Model (min^{-1})
n	exponent of Avrami Model
t_o	crystal growth initial time of Avrami Model (min)
$\mathrm{k_s}$	kinetic constant of crystal growth ($\mathrm{min}^{-0.5}$)
t_{os}	initial time of diffusion controlled growth dominated (min)
$\Delta\mathrm{G}$	Gibbs free energy (J)
$\Delta\mathrm{H}$	enthalpy change at constant temperature and pressure (J)
$\Delta\mathrm{S}$	entropy change at constant temperature and pressure (J/K)
T	temperature (K)
G	initial free energy of the hypothetical transition (J)
$\Delta G^*(\alpha)$	energy barrier of the formation of polymorphic form α (J)
$\Delta G^*(\beta')$	energy barrier of the formation of polymorphic form β' (J)
$\Delta G^*(\beta)$	energy barrier of the formation of polymorphic form β (J)
$\Delta G_f(\alpha)$	free energy of formation of polymorphic form α (J)
$\Delta G_f(\beta')$	free energy of formation of polymorphic form β' (J)
$\Delta G_f(\beta)$	free energy of formation of polymorphic form β (J)
m	magnetic moment
B_0	the applied magnetic field of NMR
M_z	net magnetization of the sample in NMR

λ	wavelength of the X-ray (Å)
θ	the scattering angle (°)
χ	the azimuthal angle (°)
q	the reciprocal space vector
d	lamellar distance of crystal planes (nm)
I	intensity of X-ray beam (a.u.)
ξ	the mean size of the crystal domains (nm)
$r_i(r_o)$	the radius of the inner (outer) cylinder
$\Omega_i(\Omega_o)$	the angular velocity of the inner (outer) cylinder
Re	Reynolds number
Ta	Taylor number
T_{ac}	critical value of Taylor vortex flow
η	apparent viscosity of suspension
η_s	apparent viscosity of the continuous phase (or liquid phase)
$[\eta]$	intrinsic viscosity of the medium (or solid phase)
ν	volume fraction
Φ	concentration of solids (by volume)
ϕ_M	maximum solids concentration (by volume)
μ_{app}	apparent viscosity
σ	shear stress

$\dot{\gamma}$	shear rate
K_σ	calculated correction factor based on the configuration of the experimental system (Pa/mNm)
τ	torque value (mNm)
Pe	Peclet number
D_r	rotary diffusivity
d_p	particle diameter
ψ	ratio of mass to area of the XRD peak
$A_a(A_b)$	area of the diffraction peaks of polymorphic forms a (b)
$m_a(m_b)$	mass of the crystals of polymorphic forms a (b)
$\sigma_a(\sigma_b)$	area fraction of the diffraction peaks of polymorphic forms a (b)
$S_a(S_b)$	mass fraction of polymorphic forms a (b)
A_{total}	total area of the diffraction peaks
m_{total}	total mass of the sample

ACKNOWLEDGEMENTS

I would like to gratefully acknowledge my supervisor Dr Gianfranco Mazzanti and my advisory team Drs Josef Zwanziger and Suzanne Budge for their guidance and assistance. Many thanks to my families for all the encouragements and the moral supports. To my research colleagues, Omar Qatami, Ibtesam Mohamed, and Cendy Wang, your very insightful discussions made this work possible and enjoyable. To Elizabeth Mudge and Emmanuel Anom for their valuable previous work. I am grateful to Ray Dube and the undergraduate project members for all the mathematical related assistance. My appreciation goes to my friends for their kindness and generous supports. One page is not enough to name you all.

This research was made possible through the financial contributions of Natural Sciences and Engineering Research Council of Canada (NSERC) and Advanced Foods & Materials Network (Afmnet).

CHAPTER 1 INTRODUCTION

Over the centuries of human history, people have never lost interest in discovering and creating novel methods to prepare food. People nowadays expect food to do more than just to fill their stomachs, but to bring them gustative and visual pleasure as a symbol of cultural progress. The food industry devotes every effort to satisfying the need of improving the taste and texture of food products. Luckily, science provides a platform for the understanding of food ingredients and eventually modifying and manipulating them to achieve better tasting food.

Dietary fat is one of the main nutrients humans need from food. It provides essential fatty acids, helps regulate bodily functions, and helps carry the fat-soluble vitamins. It also imparts a creamy texture by improving the manner flavours released in the mouth. It is undeniable that fat is a staple ingredient in many of our daily foods, such as chocolate, butter, margarine, spreads and baked goods. Fat crystallization, as a natural process during the formation of solid fat crystals from melted oil, occurs during the industrial manufacturing of most of the fat-based foods. It is an important determinant in food quality, texture, and shelf-life (Metin and Hartel, 2005). To meet the current various market demands for fat-based products, approaches from physics, chemistry and biochemistry have been used to better understand and control the crystallization behaviour of fats required for the development of the desired quality (Sato, *et al.*, 1999).

Previous research studies have demonstrates that the sensorial attributes of many fat-based foods are derived from the structures of their crystalline network (Narine and Marangoni, 1999, Wright, *et al.*, 2000, Mazzanti, *et al.*, 2005). Several factors play an important role in determining their structure, such as the solid content of the lipid, crystal microstructure, and the type of polymorph present. These factors are influenced by processing conditions such as crystallization temperature, cooling rate, and shear rate.

This research aims to observe the behaviour of nanostructure and microstructure during the crystallization of a multicomponent lipid system under several constant shear rates using novel technologies. Controlled shear was offered to mimic the industrial manufacturing of many food products, such as chocolate, ice cream, butter and shortenings. The complexity of natural

fats within the common foods limits the accuracy resulting in a huge uncertainty. Hence, most research completed on lipid crystallization focused on unitary fat components (normally the main component or critical one) as a good starting point. Several well-known models have been modified for this study to fit the experimental data from a diluted binary mixture system. The findings from this research should be of academic and industrial interest, as it more closely approximates the situation occurring in the food industry offering valuable results for a binary mixture fat network under shear.

1.1 Objectives

The aim of this study is to gain a better and wider understanding of the characteristics of the samples crystallizing under shear. To do this, rheological measurements were performed and combined with Nuclear Magnetic Resonance (NMR) and X-ray Diffraction (XRD) systems to characterize the behaviour of the diluted binary mixtures during the crystallization. The development of this method has been used to estimate the phase composition in a crystallizing binary triglyceride mixture under shear and static conditions at the end of cooling. As far as we are aware, no comprehensive study has been carried out on the subject. Thus,

The specific objectives of this research include:

- To find the effect of shear on accelerating the crystallization process by identifying the onset time of each phase present during the crystallization.
- To determine the kinetic behaviour parameters of the binary mixture during the crystallization by applying the Avrami Model (Avrami, 1939, 1940, 1941), developed for the crystal growth, and the $\sqrt{t}$ dependence kinetic model (Mazzanti, *et al.*, 2008), developed for the diffusion regime of crystal growth.
- To demonstrate the use of rheological methods to estimate effects of shear on the in-flow structure of the crystals.
- To investigate the phases formed under shear flow and if possible estimate ratios of area and mass fraction.
- To observe the orientation effect on the crystal under shear and demonstrate the shear effect on the particle (crystal) size by combining the XRD and rheological measurements.

1.2 Hypotheses

Based on the published theories and experiments on edible fat crystallization statically and under shear conditions, several hypotheses have been present to be achieved in this work:

- Shear accelerates the crystallization process.
- The fat crystals can be oriented under shear. The orientation effect can be observed by XRD measurements.
- Shear reduces the particle (crystal) size.
- The Avrami Model (Avrami, 1939, 1940, 1941) can describe the isothermal crystallization kinetics.
- During the crystallization growth stage, the viscosity of the suspension can be described by the Krieger-Dougherty Model.
- Solid solution of the binary mixtures can not be found in the polymorphic form β, but can be expected to be found in the polymorphic form β'.

CHAPTER 2 LITERATURE REVIEW

2.1. Fat Crystallization

Fat crystallization is an aggregation process of fat molecules combining into particles, larger clusters, until a three dimensional network forms (Figure 2-1). Marangoni group (Acevedo and Marangoni, 2010) has recently published the work on observing the nanostructure of triglycerides crystals using cryogenic transmission electron microscopy. The captured images showed the primary structure of the platelet-like crystals (Unruh*, et al.*, 2002) have approximate size of 150×60×30nm to 370×160×40nm which was depended on supersaturation conditions.

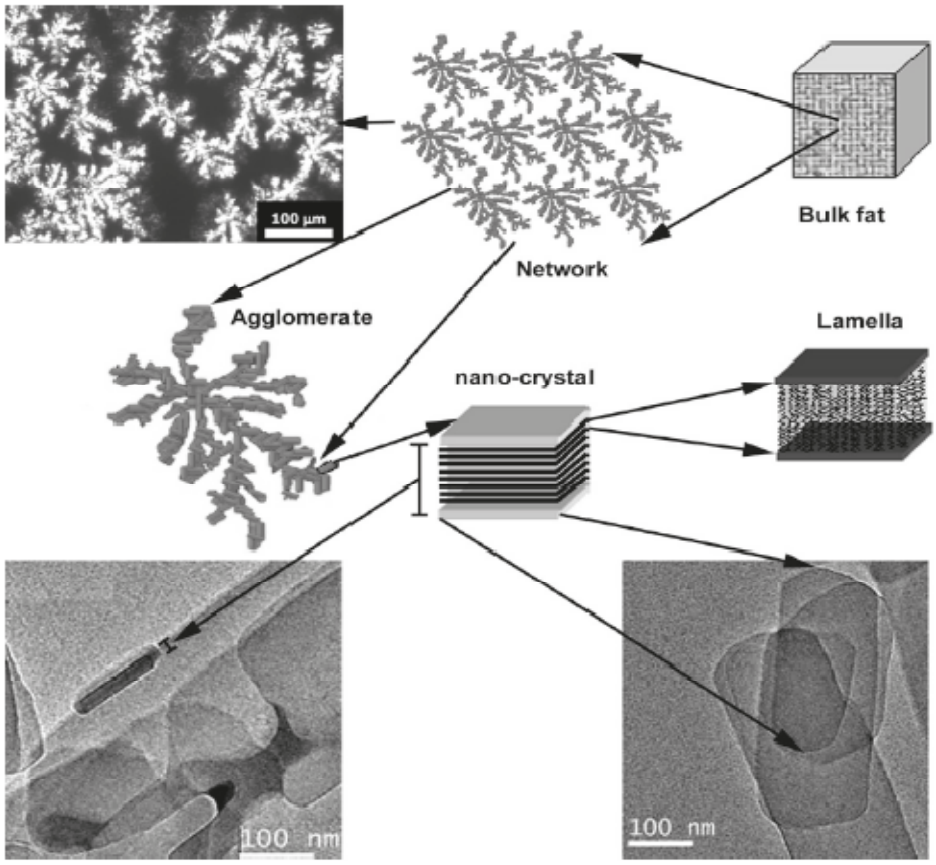

Figure 2-1 Schematic representation of the different levels of structure in a bulk fat (Acevedo and Marangoni, 2010).

The fat crystal network determines the firmness and solid-like properties of most fat-based food products (Narine and Marangoni, 1999, Wright, *et al.*, 2000, Mazzanti, *et al.*, 2005). These products are best described as dispersion systems. The solid and lipid phase can either be continuous or dispersed phase. The two main contributions of lipid phase are to supply structure, which is typically related to saturated fatty acids in the triglycerides, and to provide nutrition to the body, which is related to essential fatty acids (Flöter, 2009). Moreover, many sensory characteristics depend on the mechanical strength of the underlying fat network, such as appearance, hardness, mouth feel, and texture (Martini, *et al.*, 2002). Fat crystallization is a kinetic process in which the lipid melt must be significantly supercooled in order for crystallization to occur at a reasonable rate. Rapid cooling of the liquid fat normally cause the formation of less organized (looser packing) crystals due to the lack of time for molecules to incorporate to form a perfect crystal. On the other hand, slower cooling tends to form more ordered (tighter packing) crystals because there is sufficient time for molecules to reorganize.

2.1.1. Basic Concepts of Triglycerides (TAGs)

Triglycerides (TAGs) are the main component of edible fats constituting from 95% to 98% of the composition (Metin and Hartel, 2005). They are composed of three fatty acids units attached to one glycerol unit. TAGs with only one type of fatty acids are called mono-acid TAGs or simple TAGs, and those having more than one type of fatty acids are called mixed-acid TAGs or mixed TAGs (Sato, *et al.*, 1999). Illustrations of the typical molecular structures of these two types are shown in Figure 2-2.

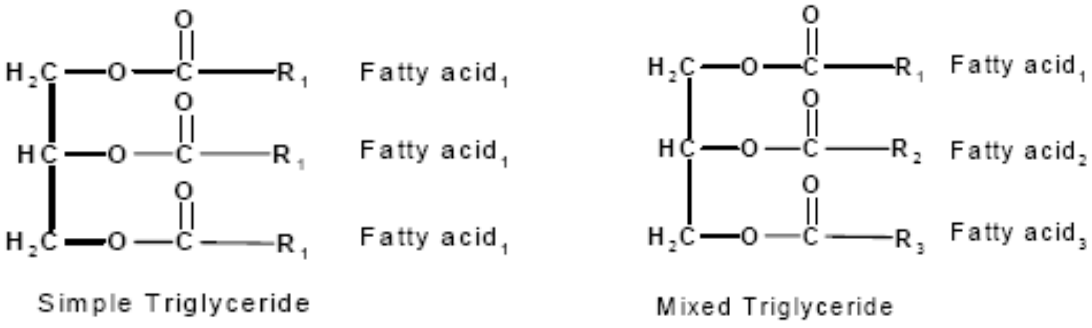

Figure 2-2 Diagrams of simple TAG and mixed TAG (Metin and Hartel, 2005).

2.1.2. Mechanism

The TAG molecules crystallize forming one longer chain with two of the fatty acids and part of the glycerol backbone, with one shorter chain having only one of the fatty acids aside. The shape of the molecule is described as a "chair" (Figure 2-3 (a)). The chain length structure produces a repetitive sequence of the acyl chains involved in unit lamellae along the long chain axis. The double chain length structure is formed when the chemical nature of the three acyl moieties are same or very similar. However, when the chemical nature of one or two of the three acyl chains is largely different, triple chain length structure is formed due to chain sorting (Lutton, 1950). The double and triple chain length structures are shown in Figure 2-3 (b).

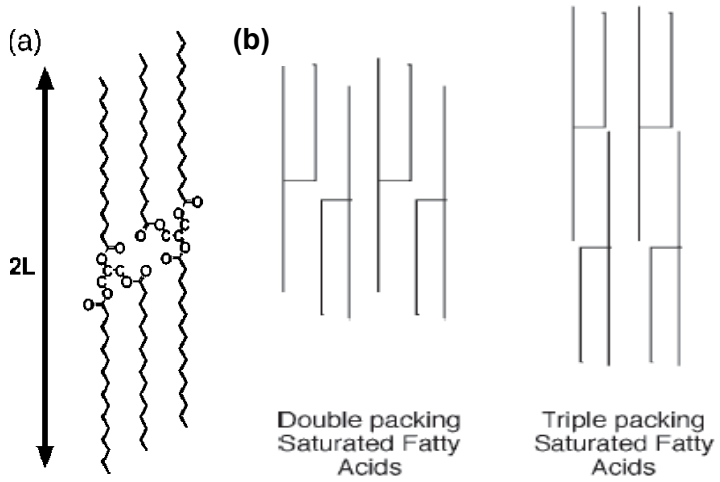

Figure 2-3 Packing arrangements of triacylglycerol molecules in the crystal lattice. (a) the "chair" structure of TAGs (Mazzanti*, et al.*, 2005); (b) the double and triple chain length structures (Hartel, 2001).

Fat crystallization must be initiated with a supersaturating process followed by two major steps: nucleation and crystal growth. It is also important to understand the nature of the liquid phase behaviours before the crystallization process.

2.1.2.1. Liquid Phase Behaviour

There have been studies demonstrating that lipids retain some degree of ordering in the liquid phase, unless the temperature is far enough above the melting point to totally destroy this ordering (Larsson, 1972, Hernqvist, 1984, Ueno, *et al.*, 1997). However, debate concerning the detail of the ordering structure in the liquid state of TAGs has lasted for many years, since Larsson (Larsson, 1972, 1992, 1997) first proposed a model representing a smectic liquid crystal nature of TAGs (Figure 2-4). This work was based on X-ray diffraction measurements. Hernqvist (1984) supported this model by incorporating Raman spectroscopy into the methods. Hernqvist's work showed that the order of TAGs melt was quite constant and the order of different segments in the hydrocarbon chains varied with different chain length. However, Larsson's model was questioned by Cebula *et al.* (Cebula, *et al.*, 1992), who claimed that a nematic phase of liquid crystals was observed (Figure 2-5), instead of the organized molecular aggregates of the smectic liquid crystals in Larsson's model. More recently, an alternative discotic model has been proposed by Corkery *et al.* (2007) purporting that triglyceride molecules exist in the liquid state with fully splayed chains ("Y" shape), forming discs structure (Figure 2-6). These discs then stacked into flexible short cylindrical rods-packing order.

Figure 2-4 Proposed structure of TAGs in the liquid state, the semctic model proposed by Larsson (Larsson, 1972).

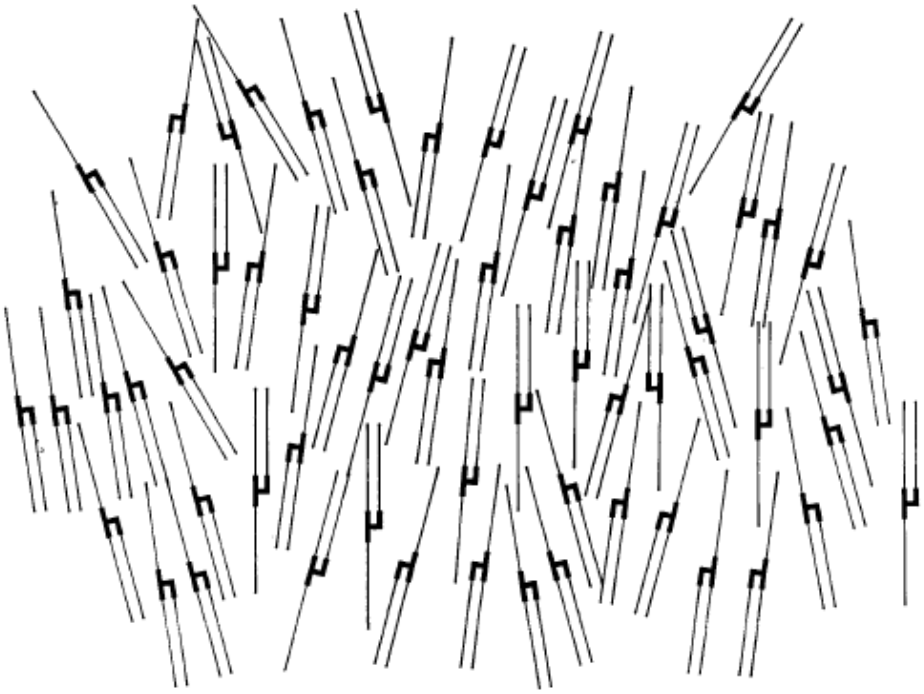

Figure 2-5 Proposed structure of TAGs in the liquid state, the nematic model proposed by Cebula *et al.* (Cebula*, et al.*, 1992).

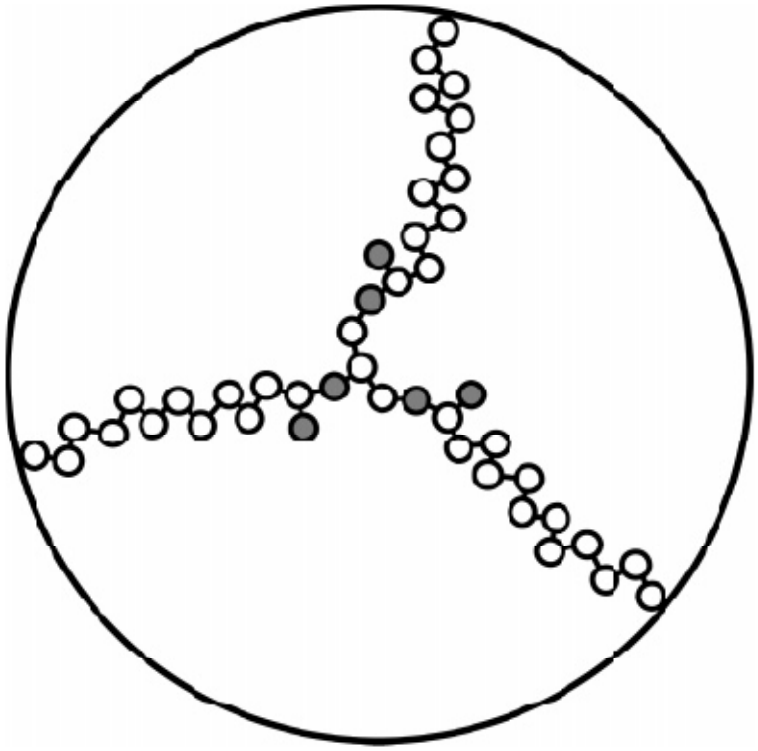

Figure 2-6 Proposed "Y" shaped structure of TAGs within each "disc" in the liquid state, the discotic model proposed by Corkery *et al.* (2007).

The natural ordering of the liquid phase leads to the formation of crystals. It may also explain the "liquid memory", a phenomenon where fat tends to form the same structure as the ordering of the liquid phase at the beginning of crystallization. It normally causes the formation of a different phase (often more stable) than the one that would appear if the fat was heated to higher temperatures to destroy the "liquid memory" (Hernqvist, 1988).

2.1.2.2. Nucleation

A nucleus is the smallest crystal which can exist in a solution at a certain temperature. Its formation requires the molecules to organize into crystal lamellae from the liquid state. The arrangement of molecules depends on several factors like the cooling rate, the crystallization temperature, and the composition of lipids (Metin and Hartel, 2005). During nucleation, some organization of molecules is expected, eventually the fat will form coherent, three-dimensional crystals (Larsson, 1972). Nuclei are formed at the beginning of nucleation process. The size and number of crystals, and the polymorphic phases formed depend on the nucleation rate. Nucleation, the formation of a crystalline phase from the liquid state, is the most important process in controlling crystallization. As previously mentioned, crystallization cannot happen at a practical rate unless the solution is super-cooled or super-saturated. Attaining these states is not necessarily sufficient to promote crystallization because of the existing energy barrier for nuclei formation. The energy barrier must be overcome prior to the nucleation; however when the nucleation happens there will be energy released associated with the latent heat of fusion, due to the lower energy state the molecules required in crystal lamellae.

Nucleation theories include primary and secondary nucleation. Primary nucleation can be classified as homogeneous and heterogeneous, where secondary nucleation occurs when crystals spawn new nuclei due to contacts between two crystals, or between a crystal and a surface such as a solid wall, or the stirrer (Hartel, 2001).

Primary Nucleation

According to classic nucleation theory, an energy barrier must be overcome to form a stable nucleus. This free energy change is positive for the formation of a nucleus. Once a nucleus

has formed, there is an associated release of energy, from the latent heat proportional to its volume. This sum of energy change reaches a maximum value at a critical nucleus size. A stable nucleus can continue to grow beyond the critical size, whereas smaller ones dissolve into the liquid phase. In other words, the critical nucleus size is the minimum size for a stable nucleus (Walton, 1969, Timms, 1995).

Homogeneous nucleation normally happens in a system of single type of molecule, where molecules come together and form dimers, and subsequently trimers by gathering additional molecules. This accumulation process continues until a stable nucleus forms. However, homogeneous nucleation rarely occurs, especially under commercially conditions due to the presence of foreign nucleation sites such as dirt, dust particles or rough surfaces.

The presence of these foreign nucleation sites reduces the energy barrier to heterogeneous nucleation (Garside, 1987, Mullin, 1993). For example, nucleation on a pitted wall results in a decrease of the surface energy needed to form a stable nucleus. These interactions at the interface between the solid particle and the liquid phase result in a local ordering of molecules, and are thought to be the key to heterogeneous nucleation mechanisms (although the exact mechanisms are not yet clearly understood).

Secondary Nucleation

The formation of new nuclei in the presence of existing solid particles is called secondary nucleation (Metin and Hartel, 2005). This is influenced by numerous factors including the degree of supercooling (the driving force for crystallization), impurities (foreign nucleation sites), the number and size of existing crystals, and the roughness of the environment surface.

In the absence of shear, secondary nucleation may occur under certain circumstances due to interactions between existing crystal nuclei or with the surface of the container at a lower degree of supersaturation or supercooling than primary nucleation (Walstra, 1987). In most commercial processes where shear is involved during crystallization, secondary nucleation may occur attributed to the crystals interacting with each other, the wall surfaces, or the stirrer (Mullin, 1993). The agitation may also lead to fracture or breaks within the structure of existing crystals thereby forming secondary nuclei (Figure 2-7).

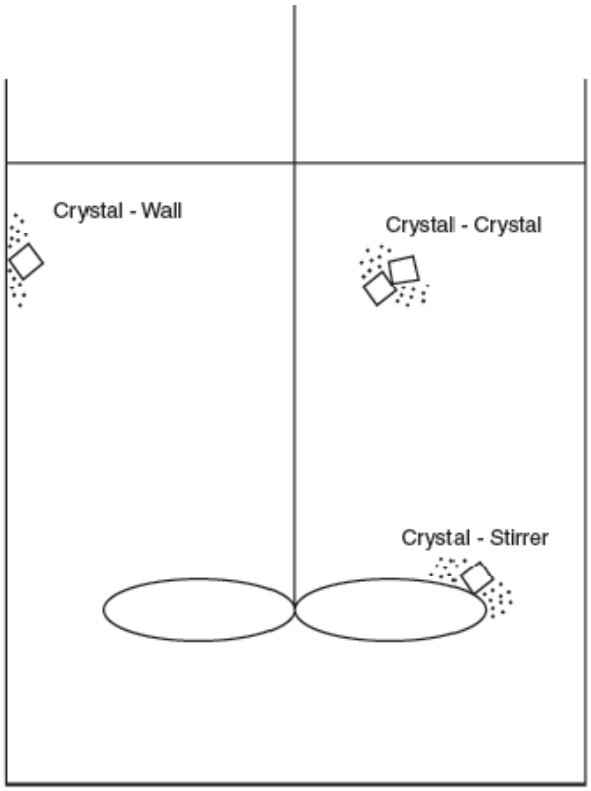

Figure 2-7 Potential sources of contact nuclei in a stirred crystallizer (Hartel, 2001).

2.1.2.3. Crystal Growth

Once the nuclei reach the critical nucleus size, they grow by the incorporation of other molecules from the liquid phase, which is called crystal growth. When a new TAG molecule migrates from the liquid phase to the surface of the existing crystal, its configuration and location are the determinants of the probability of it binding into the lattice or returning to the liquid state. The growth unit, either one molecule or a cluster of molecules can find an appropriate site for incorporation in to the lattice. If a site is found, there will be a release of latent heat after the incorporation. The energy generated must to be taken away from the surface in time so that the temperature will not be increased to the point where no further growth can occur. The process continues as long as there is a driving force for crystallization (Metin and Hartel, 2005).

The crystal growth rate depends on several factors including the degree of supercooling, the rate of molecular diffusion to the crystal surface, the difference between the rates of attachment and detachment of molecules at the interface, the nature of the crystal-melt interface

and the structure of the crystal surface (Garside, 1987, Fisher and Kurz, 1992). In multicomponent fat systems, the growth rate is reduced by the competition to the vacant sites adherence between similar TAG molecules. The crystal growth is affected by lipid composition, temperatures, and shear rates (Mazzanti, *et al.*, 2005). Chain length also has been found to have an effect on crystal growth rate, with an increase in the chain length of component triglycerides causing a reduction in the linear growth rate (Mazzanti, *et al.*, 2005). Eventually crystal growth ceases when the system attains phase equilibrium or the entire system is crystallized (Hartel, 2001).

2.1.2.4. Avrami Model for Crystallization

The Avrami equation is the most universally used approach to describe isothermal crystallization kinetics in the study of fat crystallization. This kinetic formulation was developed independently by various researchers in the 1940s. This is why it is also called the Johnson-Mehl-Avrami-Erofeev-Kolmogorov (JMAEK) equation (Kolmogorov, 1937, Johnson and Mehl, 1939, Erofeev, 1946). This work was then popularized by Avrami in three of his articles published between 1939 and 1941 (Avrami, 1939, 1940, 1941). This model describes the changes in mass (or volume) of the crystals as a function of time as described by Eq. (1). This equation is valid over the entire crystallization process including nucleation and crystal growth:

$$\Phi_c = 1 - \exp(-kt^n) \quad (1)$$

where Φ_c is the crystalline fraction developed at time t and constant temperature, k is the Avrami rate constant, and n is the Avrami exponent. The Avrami rate constant k represents a combination of nucleation and growth rate constants. It is primarily dependent upon the crystallization temperature (Kawamura, 1979). The Avrami exponent n is a function of the number of dimensions in which growth takes place and provides qualitative information on the nature of the nucleation and growth processes. Based on the Avrami theory of crystallization, n should be an integer form from 1 to 4. A value of 4 represents the transformation having contributions from three dimensions of growth and one constant nucleation rate. Site saturation can lead to n values of 3, 2 or 1 for surface, edge and point sites, respectively. However, as an adjustable parameter, n can be non-integral. The random nucleation and unhindered growth at

the beginning of the crystallization leads to high values for n. Once the nucleation sites are consumed the formation of new particles will cease, meaning site saturation may lead to lower n values.

In the Avrami simplified framework Nucleation is either instantaneous, with nuclei forming all at once early prior to growth, or sporadic, with the number of nuclei increases linearly with time. Christian (1965) has illustrated some expected n values for various transformation (liquid to crystals) situations. An n value around or greater than 4 suggest heterogeneous nucleation and indicates the effect of sporadic nucleation on the development of new crystals. A value of 3 also indicates spherulitic growth but from instantaneous generated nuclei. An n of 2 represents high nucleation rate and plate-like growth, however the growth is primarily two dimensional. Toro-Vazquez *et al.* (2000) found the values of n around 4 or greater were obtained in all cases when the blends of 26, 42, 60, and 80 (wt/vol) palm stearin in sesame seed oil were tested. Similar magnitudes have been obtained by Metin and Hartel (2005) in blends of cocoa butter with 5 and 10% of anhydrous milk fat.

Transformations often follow a characteristic s-shaped (sigmoidal) profile where the transformation rates are low at the beginning and the end but rapid in between. The initial slow rate is due to the time required for nucleation. Once a great number of nuclei begin to grow into particles, the transformation is rapid. Near the end of the crystallization process, there is little untransformed material, which slows down the transformation rate. Eventually, the remaining particles contact each other where the growth ceases.

Recently, experimental data of researches on fat crystallization revealed that crystallization process happened in two distinct growth regimes, depending on time. Avrami plots for the oil blends resulted in more than one of the crystal growth rates (Toro-Vazquez, *et al.*, 2002, Narine, *et al.*, 2006, Mazzanti, *et al.*, 2008). The first regime, including the transformation from liquid to solid, was very well described by the Avrami equation model:

$$SF = SF_{max}\{1 - e^{-[k\cdot(t-t_0)]^n}\} \quad (2)$$

where SF is the solid fraction (%), SF_{max} is the maximum solid fraction at the end of the crystallization, and to is the initial time when the crystal growth starts. However, the Avrami model no longer satisfies the description of the crystal growth as the rapid growth rate slows

down. Instead, the growth behaviour after a certain time t_{os} is well described by a square root of the time dependence, defined as:

$$\frac{\partial C_{SF}}{\partial t} = \frac{k_s}{2\sqrt{t - t_{os}}} \quad (3)$$

where k_s is the kinetic constant ($min^{-0.5}$) the typical value of which lies in the range of 0.14 to 0.54 reported by Mazzanti *et al.* for milk fat (2008).

When the final stage of crystallization dominated by diffusion, the crystal growth rate is linearity related to the square root of time. Diffusion controlled reactions are ones that occur so quickly that the reaction rate is the transport rate of the reactants through the medium. In the final stage of fat crystallization, the crystallization rate is the rate of the crystallizable material remaining in the medium encounters each other or other crystals, since most of the crystallizable material is already out of the solution.

2.1.3. Polymorphism

Polymorphism is the ability of a molecule to take more than one crystalline form depending on its arrangement within the crystal lattice (Metin and Hartel, 2005). It can also be understood as the ability to form different unit cell structures in a crystal, originating from a variety of molecular conformations and molecular packing. In lipids, different polymorphs are caused by difference in hydrocarbon chain packing and variations in the tilt angle of the packing. Polymorphism is influenced by the molecular structure and also by the external factors like temperature, pressure, rate of crystallization, impurities, and shear rate (Sato, 2001).

2.1.3.1. Polymorphic Types and Sub-modifications

Natural fats contain a huge variety of fatty acids, which display wide and complex polymorphisms during crystallization. Triglycerides, the main component of natural fats, share the same character, with three main fat crystal polymorphs α (hexagonal sub-cell), β′ (orthorhombic sub-cell), and β (triclinic sub-cell), in order of increasing stability.

A sub-cell is defined as the cross-sectional packing mode of the aliphatic chains in TAGs (Martini, *et al.*, 2002), as shown in Figure 2-8. In the solid state, the hydrocarbon chains pack together, constructing one of the specific sub-cell structures. The sub-cells are described by a letter indicating the symmetry (e.g., O for orthorhombic, T for triclinic, M for Monoclinic) followed by a symbol indicating whether a parallel (//) or perpendicular (⊥) position between the zigzag planes of the different chains.

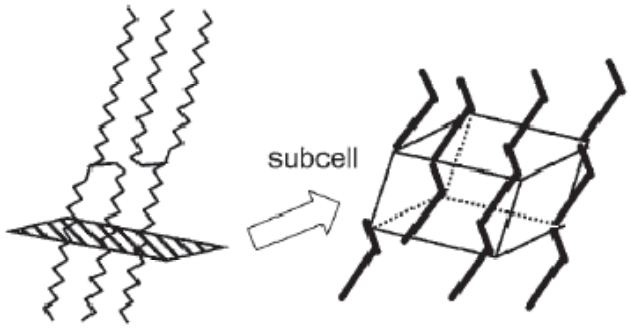

Figure 2-8 the sub-cell structures of TAGs (Sato and Ueno, 2005)

Ten types of the sub-cell have been revealed in crystalline fats and lipids (Small, 1986), among which five sub-cells are predominant; H, $O_{\perp}$, $O'_{\perp}$, $T_{//}$, and $M_{//}$ (Figure 2-9). The hexagonal type (H) presents rotationally disordered orientation of the polymethylene zigzag planes. The chain packing does not reveal specific orientation of the hydrocarbon chains, making the H sub-cell least stable compared to the other four (Sato, *et al.*, 1999). The $O_{\perp}$ type sub-cell consists of the zigzag planes nearly perpendicular to the neighbours, which are all parallel to each other in the $T_{//}$ type. Two sub-cells of $O'_{//}$ and $M_{//}$ contain the zigzag aliphatic chains arranged in a parallel manner. There are several other sub-cell structures; however, some of them belong either to $O_{\perp}$ or to $T_{//}$ (Sato and Ueno, 2005).

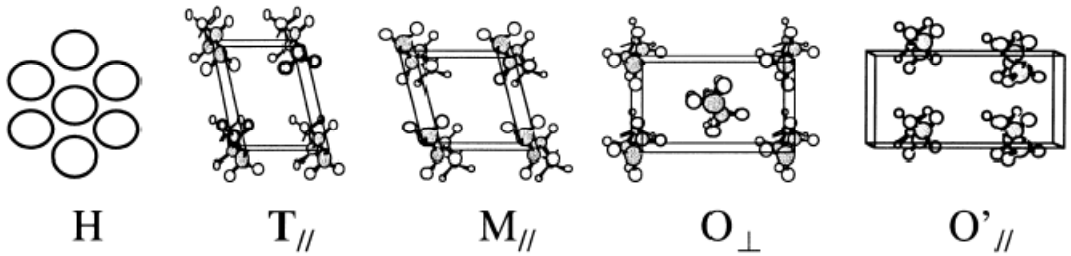

Figure 2-9 the five predominant sub-cell structures (Sato*, et al.*, 1999)

Although very few exact structures have been completely elucidated, the characteristic signatures of different polymorphic forms have been widely documented (Figure 2-10). α is an unstable form in which the hydrocarbon chains are packed in a hexagonal type sub-cell. β′ is a metastable form that has an orthorhombic perpendicular sub-cell and hydrocarbon chains that are inclined with respect to the basal plane by about 108 degrees. β is the most stable form and has a triclinic parallel sub-cell with the hydrocarbon chains inclined at about 128 degree (Takeuchi, *et al.*, 2003).

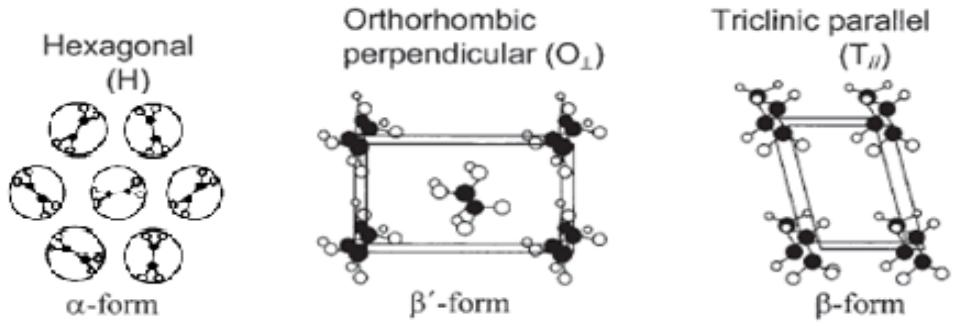

Figure 2-10 Typical sub-cell structures of TAG polymorphs. α, β', and β forms have hexagonal (H), orthorhombic perpendicular ($O_{\perp}$), and triclinic parallel ($T_{//}$), respectively (Mazzanti*, et al.*, 2005, Sato and Ueno, 2005).

Despite the fact that main polymorphic phases of monoacid triglycerides have been studied meticulously, the polymorphic sub-modification concepts are still unclear due to the difficulties of differentiating crystal imperfection from well packed crystals. Buchheim (1970) reported the existence of two β′ forms for trilaurin (LLL, C12); in one the hydrocarbon chains were vertical to the basal plane and the other had tilted chains. Later, three types of β′ form for trilaurin and two for trimyristin (MMM, C14) were reported based on their different melting points (Hagemann and Rothfus, 1983). The existence of two β′ and β forms for tripalmitin (PPP, C16) were proposed by Kellens's research on the X-ray diffraction and polarized light microscopy (Kellens, *et al.*, 1990, Kellens and Reynaers, 1992). SOS (1,3-distearoyl, 2-oleoyl-sn-glycerol), a mixed-acid TAG, has been proved to have five polymorphic forms in which two β forms are present (Sato, 2001). Additionally, more than one sub-modification within the main polymorphic forms has been identified in some natural fats. For instance, six different

polymorphic forms have been identified in cocoa butter, in which two β′ and two β forms are included (Wille and Lutton, 1966).

2.1.3.2. Morphology and Thermodynamic Stability of Polymorphic Forms

The three main polymorphic forms are distinguished by the increasing angle of tilt from α to β′ and finally to β, with a resultant thinning and tighter packing of the molecular layers in that order (Table 2-1). The morphology of the crystal is determined by internal and external conditions, both of which would be different in the three polymorphic forms of triglycerides. The hydrocarbon chain packing of the β form is denser than the α form. The denser packing gives increased stability of the polymorphic form. In addition, stable forms have higher melting point and higher heat of fusion than the less stable forms.

For the LLL/MMM system in this work, the thermal behaviour of LLL and MMM was studied by several research groups, including Hagemann and Rothfus (1983), Lutton and Fehl (1970), and recently Takeuchi *et al.* (2003) as shown in Table 2-1. The slight disagreement between these literatures may be due to the difference in cooling and heating rates employed or the formation of polymorphic sub-modifications.

Table 0-1 Melting temperature and enthalpy of fusion for the polymorphic forms of LLL/MMM

TAG	Polymorphic form											
	Melting point (˚C)									Heat of fusion (kJ/mol)		
	α			β'			β			α	β'	β
	x	y	z	x	y	z	x	y	z	x	x	x
Trilaurin	14	15.2	15	30,34,40	34	35	46	46.5	46.5	72	86	116
Trimyristin	31	32.8	33	54, 56	50.1	47	58	56.2	57	97.1	109	144

[x] Lutton and Fehl (1970), [y] Hagemann and Rothfus (1983), [z] Takeuchi et al (2003)

The Gibbs free energy determines the thermodynamic stability of the present polymorphic form;

$$\Delta G = \Delta H - T\Delta S \quad (4)$$

where ΔH is the enthalpy change, T is the temperature and ΔS is the change in entropy at constant temperature and pressure. The phase transition occurs naturally as the free energy decreases (negative ΔG), and reaches the equilibrium with ΔG becoming zero. As the free energy increases, ΔG becomes positive and the transformation is not possible under the specified conditions. Since the crystal Gibbs energy is highest for α, in between for β′, and lowest for β, the driving force of crystallization is always highest for β, and vice versa for β′ and α. The difference in Gibbs free energy between polymorphic forms is the driving force for the phase transition. This applies to the crystallization from both solution and melt as the molecules become more tightly arranged in the crystal lattice.

2.1.3.3.Variations of Polymorphic Transition

The crystallization normally starts from the presence of thermodynamically unstable phases followed by reorganization to more stable phases, which is from α to β′ and then to β in polymorphic transition. This phenomenon was described by Mutaftschiev (1993), without considering the effect of external influences like temperature fluctuation, pressure changes, etc. or the kinetic factors such as supercooling or supersaturation, which could cause the direct transition from α to β in a crystallization process instead of from α to β′ and then to β (Takeuchi, *et al.*, 2003), as known as the Ostwald step rule.

The dependence of phase transformations and polymorphic stability between polymorphic types on the Gibbs free energy has been explained by Rousset (2002) as shown in Figure 2-11.

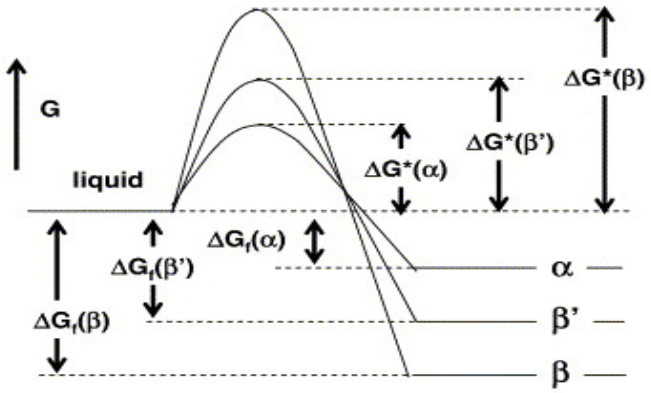

Figure 2-11 Energy barrier diagram for the 3 main polymorphic forms of a TAG at a given condition below their melting temperatures (Rousset, 2002)

This diagram shows a hypothetical transition starting from the initial free energy G of the liquid to the three main polymorphic types α, β', and β, which depends on the energy barrier $\Delta G^*(\alpha)$, $\Delta G^*(\beta')$, and $\Delta G^*(\beta)$ also the free energy of formation $\Delta G_f(\alpha)$, $\Delta G_f(\beta')$, and $\Delta G_f(\beta)$. Because the rate of nucleation is related to the height of the energy barrier on the reaction path, α will nucleate at a much faster rate than β even though the change in free energy is greater for β, $(\Delta G^*(\beta) - G)$ than α, $(\Delta G^*(\alpha) - G)$, according to this reaction pathway the height of the energy barrier for β is greater than that for α (Rousset, 2002).

Lipids exhibit monotropic polymorphisms, where unstable forms are the first to crystallize in a supercooling situation because of their lower energy barrier to overcome, followed by the metastable forms and eventually reach the most stable polymorphic forms. Transition of unstable to stable forms can be achieved by a slight temperature increase above the melting point of the less stable form. The temperature change causes the melting of the unstable form, and then solidification in a more stable one. It also can be achieved without melting involved. The difference of energy could be the driving force for the transition. During the process, the chair structure of TAG molecules remains (Sato, 2001). The arrangement of layers for α form does not change when it is transformed to β' form, although the tilt angle and the lateral chain packing changed. The $\beta' \rightarrow \beta$ transition is perhaps the most important economically because it is associated with the swelling or bloom of saturated triglycerides in many food industries like chocolate, shortening, spread, and margarine. Swelling changes appearance and texture, which cause marked deterioration of market quality in products containing hydrogenated

fats. The phenomenon is believed to occur with rapid formation of the β form (Sato and Garti, 1988).

The rate of phase transition depends on the length of the fatty acid chain with larger for a short chain and smaller for a long chain. Natural fats usually take a slow phase transition because of the large number of TAGs contained. As mentioned earlier, the α form presents during a rapid cooling process, but it is generally very unstable and quickly changes to β′ form. After that, the β′ form is maintained for an extended time, which, in many natural fats, are long periods of time (hours to months) because of compound or solid solution formation (Walstra, 1987), although the β form will be eventually formed in most of the natural fats.

2.1.4. Binary Mixture System of TAGs

Polymorphism has been well studied at a molecular level for pure systems of major TAG components. However, in food and material industries, fats form a multi-component system consisting of different types of TAG species. Hence, the next step in approaching multi-component systems is to study the binary systems of major TAGs, which reveal the nature of molecular interactions between the component materials at macroscopic and microscopic dimensions. (Minato, *et al.*, 1997)

Miscibility of the metastable polymorphs of α and β′ phases was observed in TAG binary mixtures which C_n differed by 2 whereas immiscibility occurred in all polymorphic forms for when C_n differed by 4 and 6. In the LLL/MMM system, miscible phase behaviour occurred in metastable α and β′ forms, whereas the most stable β form exhibited a eutectic phase. This research performed experiments using the pure triglycerides trilaurin (LLL) and trimyristin (MMM) and their binary mixtures (Takeuchi, *et al.*, 2003).

2.2.Techniques Used in Fat Crystallization Studies

Basic methods for studying the polymorphism of fats include both thermal and optical analytical methods. Typically, differential scanning calorimetry (DSC), X-ray diffraction (XRD), nuclear magnetic resonance (NMR), neutron diffraction, infrared absorption spectroscopy and

polarized light microscopy (PLM) have been used extensively to study the crystallization and polymorphism of triglycerides and their mixtures in the past several decades. In this work of research, time domain nuclear magnetic resonance and synchrotron X-ray diffraction technology were used combining with rheological information recorded by a rheometer (measuring head) to better understand the fat crystallization of the binary system under shear flow condition.

2.2.1. Nuclear Magnetic Resonance Technology

The signal in NMR spectroscopy results from the difference between the energy absorbed by the spins which make a transition from the lower energy state to the higher energy state, and the energy emitted by the spins which simultaneously make a transition from the higher energy state to the lower energy state. The signal is thus proportional to the population difference between the energy states in each thermodynamic phase of the material. In this work, the fat crystals in a solution exhibit two phases: solid phase and liquid phase. The proportional difference between solid and liquid phases is called the solid fraction (SF), which is defined as the ratio between the solid NMR signal and the total signal due to both solid and liquid nuclei of the sample.

Fats melt over a range of temperatures because of the molecular diversity and their polymorphic characteristics. The melting profile is given by the change in solid fraction at different temperatures. The determination of SF is an essential experimental parameter in the research of crystallization to display the stability and structure of fats. Measurement of SF by NMR is considered as a powerful tool for studying the molecular conformations of the TAGs in a crystalline state and the overall crystallization behaviour, since one big advantage of NMR is that it can rapidly and non-destructively measure the ratio of hydrogen nuclei in the solid and liquid phases. NMR's quick and accurate measurement also brings great benefit to the manufacturer like the baking, confectionery, etc. (Saitô, 1986).

2.2.1.1. Principles of NMR

Originally, nuclear magnetic resonance (NMR) is a phenomenon occurring when the nuclei of certain atoms are immersed in a static magnetic field and exposed to a second oscillating magnetic field. It is experienced by only some type of nuclei, dependent upon whether they possess a property called nuclear spin (Hornak, 1997).

Nuclear spin is a property of nature possessed by protons, electrons, and neutrons. It comes in multiples of $\pm 1/2$. Individual unpaired electrons, protons, and neutrons each possess a spin of $1/2$. For instance, the Hydrogen nucleus is composed of a single proton. It has positive charge, and nuclear spin. The combination produces a magnetic moment (m). The magnetic moment of hydrogen nuclei causes them to behave like tiny magnets with north and south poles. In a fat sample, hydrogen atoms are normally randomly oriented, which means there is a distribution among the quantum states. However, when placed in a magnetic field the orientation of the hydrogen nuclei change so that their magnetic moments are aligned either with or against the magnetic field (B_0). A slight excess align with the applied magnetic field (B_0)creating a net magnetization (M_z) in the sample. Since the external magnetic field (provided by a permanent magnet) is much greater than the sample's net magnetization, it is impossible to detect the sample's small magnetization in this state. It must be, thereby, separated from the external magnetic field by applying a secondary magnetic field. A Radio Frequency (RF), low-energy electromagnetic pulse applied along the $+\mathrm{X}$ axis to the aligned nuclei instantaneously creates a secondary magnetic field that causes the magnetic moments to tip away from the equilibrium state. The length of the pulse determines if it is a 180° pulse which inverts the magnetization or a 90° pulse which align their axes of rotation (or precession) perpendicularly to the external field. These nuclei will eventually realign in the applied magnetic field, but this process takes time. Once the hydrogen nuclei are in an excited state, they exchange energy with each other and with their surroundings. The former causes the de-phasing of the nuclei, also known as spin-spin relaxation. The latter causes them to relax back to their equilibrium state, either aligned mainly with or against the magnetic field. The realignment generates a small but detectable excess oscillating magnetic field in the $\mathrm{X}-\mathrm{Y}$ plane perpendicular to the external magnetic field. After the pulse, the signal is detectable for microseconds to seconds. These oscillations induce an

alternating voltage (the NMR signal) in a detection coil, and thus the kinetics of the realignment can be monitored.

2.2.1.2.NMR Approaches in Solid Fraction Determination

There are two approaches to measure SF by NMR, indirect and direct. The indirect approach is based on the liquid component measurement, thus reading only the liquid signal at two temperatures, when the sample is completely melted and when it is tempered and uses the ratio to determine the SF. However, this approach requires more information, like the mass and density of the sample, and also keeping the volume of the sample constant. According to these limitations, the indirect approach is known as a more complicated method compared to the direct one, which calculates the ratio between the solid and liquid components directly without any further work required (VanPutte and Enden, 1974).

The NMR signal decays because of relaxation. The decaying signal is called the FID (free induction decay) signal. It is the signal caused by relaxation of the hydrogen proton magnetic spins back to equilibrium state after the power radio-frequency excitation of the sample. In the solid phase, where the nuclei have limited mobility, oscillations are heavily damped, and the signal decays relatively quickly (about 10-40 μs). In a liquid, however, the surroundings are more mobile, thus causing less damping and a slower decay of the signal. The FID signal shape can therefore be used to distinguish between solid and liquid components of a sample. This characteristic is exploited in the direct technique, where a first measurement (proportional to the sum of the solid and liquid nuclei) is made quickly after the pulse, and a second reading (of only the liquid nuclei) is made at a later time (70 μs), when the solid component has decayed.

The detector is “blinded” for a short time after the application of the electromagnetic pulse, which is called “dead time”. It lasts usually for a few microseconds while resonance processes damp in the disturbed sensor circuit. Therefore some of the signal from the solid fat, which is already decaying during this time, is lost before the first measurement can be made. In many systems, an extrapolation factor (Called F factor (f)) can be determined by measuring samples with known SF, so the calibration accounts for the inevitable loss at short times

(VanPutte and Enden, 1974). The F-factor allows predicting the FID amplitude value (S) immediately after the RF pulse. The SF value is often determined by taking two points of measurement, point S (corresponding to total solids plus liquids) and point L (corresponding liquids only). The equation is shown in the plot below (Figure 2-12):

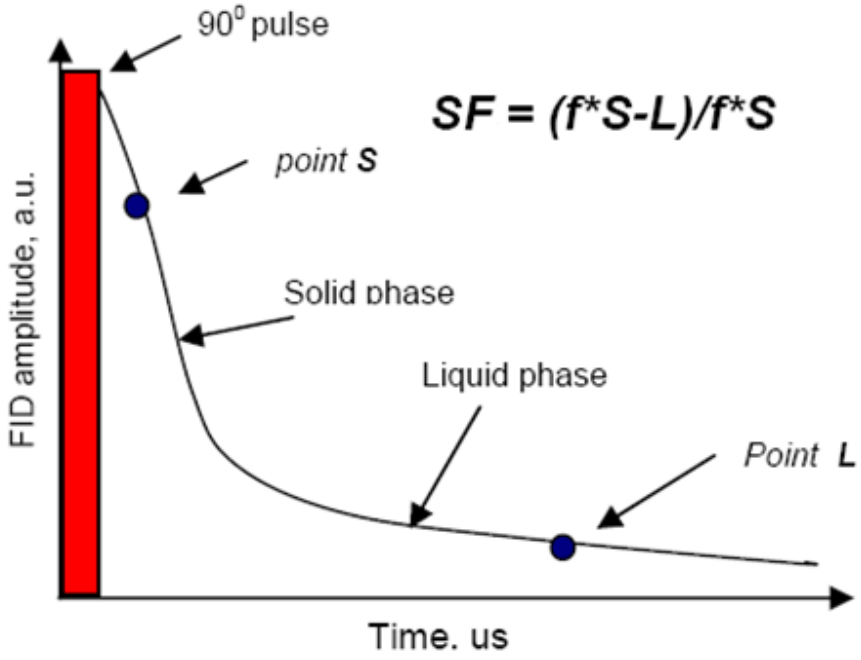

Figure 2-12 Principle of SF Determination Using FID (ResonanceSystemsLtd., 2007)

2.2.1.3.Time Domain Nuclear Magnetic Resonance Technology

Time Domain Nuclear Magnetic Resonance (TD-NMR), which was used in this research, is a type of NMR that deals only time domain NMR signals but not frequency domain ones. It does not deal with spectroscopy or magnetic resonance imaging (MRI). This is due to that fact that TD-NMR has no spectral resolution or strong enough pulse sequences to guarantee clear MRI. TD-NMR instruments are commonly known as small in size, low field and low resolution, and designed to detect hydrogen or fluorine nuclei (Todt, *et al.*, 2001).

TD-NMR is also known as low-resolution NMR. The first one in quality control/quality assurance (QC/QA) started in early 1970's in cooperation between Unilever Research (The Netherlands) and Bruker Analytik GmbH (Germany). The objective was raised to build a small

table-top time-domain NMR analyzer for the solid-to-liquid ratio analysis of fat compositions. The method, based on the first TD-NMR analyzers, was an immediate success and was introduced in all major fat facilities world-wide (Todt, *et al.*, 2006). Since then, TD-NMR analyzers have been produced by a number of commercial companies, with thousands installations across almost all industrial sectors.

In most cases, TD-NMR analysis is quantitative and rapid (normally within seconds or minutes). It is non-destructive and non-invasive. Because of all of these and its ease of use, it is widely used for routine analysis in agriculture, food, chemical, pharmaceutical and medical industries. For instance, in the rubber industry, TD-NMR is used for measuring the cross-link density of the polymer chains, which strongly influences the mechanical properties of the products (Guthausen, *et al.*, 2000). Fat contents of the commercial margarine products from Unilever were measured by TD-NMR and compared with the results from the chemical analysis in one of the Kamlowski group's work (Guthausen, *et al.*, 2004). The processed NMR signal was linearly correlated with the fat content obtained by the chemical analysis. The correlation coefficient between NMR Fat% and reference values was 0.991-0.996. The linear correlation allowed the application of NMR for fat measurements.

2.2.2.Synchrotron Radiation X-ray Diffraction (SR-XRD)

X-ray diffraction has been used as a powerful tool to monitor polymorphic form transformations of various TAG mixtures back from 1940s (Clarkson and Malkin, 1948). Many X-ray diffraction studies of edible fats have been conducted under static conditions providing better understanding of the nanostructure of crystals (Kellens, *et al.*, 1991, Ueno, *et al.*, 1997, Mazzanti, *et al.*, 2003, Metin and Hartel, 2005).

2.2.2.1.Principles of X-ray Diffraction

The X-rays used for XRD have one wavelength after passing the monochromator. Normally, when a beam of X-rays enters the sample surface and hit a crystal, most of the X-rays go through, yet some of them are reflected by the crystals in the sample, due to interaction with

the electrons of the atoms. These X-rays are scattered in all directions so most of them are cancelled out by destructive interference, but there are some directions where they will add through constructive interference to produce a diffracted beam. When diffracted, the single beam of X-rays is split so the X-rays come out of the sample in several beams at different angles to the sample. The detected position and strength of these beams is called the diffraction pattern. Each polymorphic phase reflects X-rays slightly differently and so has a different diffraction pattern. A mixture gives a pattern that is made up of all the patterns of each compound.

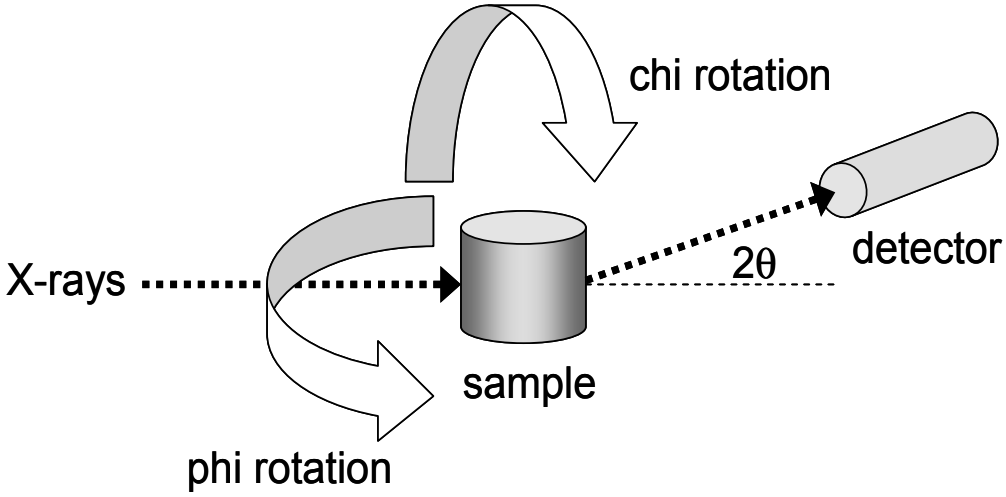

Figure 2-13 Diagram showing the sample rotation planes of $\boldsymbol{\phi}$ and $\boldsymbol{\chi}$ (Guthrie, 2008).

The atoms of a crystal, represented as spheres in Figure 2-14 can be viewed as forming different sets of planes in the crystal. For a given set of lattice plane with an inter-plane distance of d, the condition for a diffraction (peak) to occur can be simply written as:

$$n\lambda = 2d\sin\theta \quad (5)$$

where λ is the wavelength of the X-ray, θ is the scattering angle and n is an integer representing the order of the diffraction peak. The equation that determines the angle at which constructive interference occurs is known as Bragg's law, which was an extremely important discovery (Bragg, 1913). The law holds true if the atoms are replaced by molecules or collections of molecules, such as colloids, polymers, proteins and virus particles.

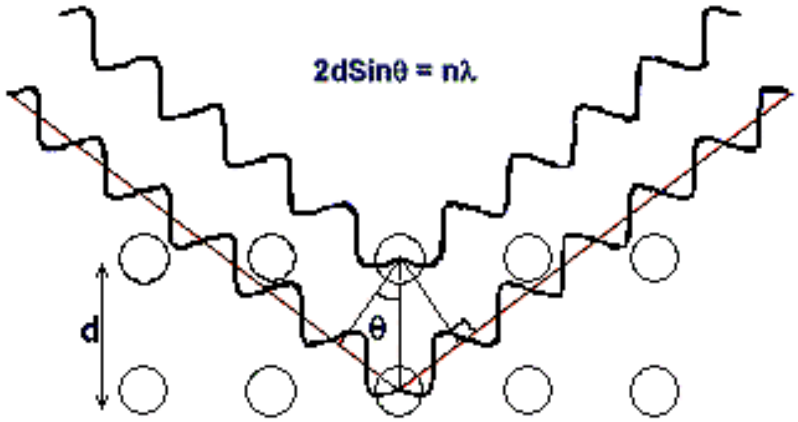

Figure 2-14 Schematic representation of X-ray scattering from a crystalline material

To analyze X-ray diffraction data is often convenient to look at the diffraction measurement in terms of the reciprocal space vector q rather than the diffraction angle 2θ, which is the angle between the incoming beam and the outgoing beam: $q = \frac{4\pi}{n\lambda}\sin\theta$. Therefore, $q = 2\pi/d$, according to Bragg's law. The value of q is independent of wavelength λ, hence diffraction patterns taken at different wavelengths can be compared directly.

2.2.2.2.Previous Studies of X-ray Diffraction in Polymorphism

In the case of polymorphism, X-ray diffraction technique is the most definitive method for determining the internal structure of crystals by providing detailed crystallographic information of TAG molecules in the lattice. Typical X-ray diffraction patterns of fats exhibit two groups of diffraction lines corresponding to the long and short-axis spacings. The height of the chair structure can be found by X-ray diffraction as the long spacing, which represents the planes formed by the methyl end groups. The short spacing, on the other hand, is the distance between the molecules in the chair structures, which provides information about the lateral structure, or the sub-cell structure. Unfortunately, it is almost impossible to form large enough single crystals from triglycerides or triglyceride mixtures. Thus the material is treated as a powder.

The short spacings refer to the cross sectional packing of the hydrocarbon chain and are independent of the chain length(Larsson, 1966). They are referred to as the fingerprint region, since the polymorphic form can be distinguished from each other based on these peaks alone. Each polymorphic form has different short spacing. α form contains a single strong and very broad line at ca. 4.15Å; β′ form has two strong lines at 4.2Å and 3.8Å, often accompanied by two weaker ones; and β form has a strong line at 4.6Å (Larsson, 1997). A very similar result of the short spacing values of triglycerides trilaurin and trimyristin was reported by Takeuchi *et al.* (2003) determined by WAXS spectra. The three basic polymorphs are characterized by distinct wide angle diffraction patterns. α was identified by a single peak at 0.42 nm, β′ by the closely spaced peaks at 0.42 and 0.38 nm, β by a strong peak at 0.46 nm and the closely spaced peaks at 0.39 and 0.38 nm.

Lamellar distance of triglycerides (long spacing), on the other hand, are very much dependent on the chain length and molecular structure of triglycerides, like the angle of tilt of the molecules. They may present valuable information about the phase transitions and can also be used to identify the polymorph in cases where the material is better known. Lamellar distances of pure trilaurin and trimyristin, which are investigated in this work, have been published by several research groups summarized in Table 2-2.

Table 0-2 Lamellar distance of trilaurin and trimyristin determined by X-ray diffraction

TAG	Polymorphic form								
	Lamellar distance , LD (nm)								
	α			β'			β		
	x	y	z	x	y	z	x	y	z
Trilaurin	3.55	3.56	3.5	3.29	3.29	3.2	3.12	3.12	3.1
Trimyristin	4.03	4.12	4.1	3.67	3.77	3.7	3.55	3.58	3.6

[x] Lutton and Fehl (1970), [y] Lutton, *et al.* (1948), [z] Takeuchi et al (2003)

2.2.2.3.Synchrotron X-ray Diffraction

One of the most exciting methodologies that have recently been applied to fat polymorphism is synchrotron radiation XRD (SR-XRD). Synchrotron radiation is electromagnetic radiation generated by the acceleration of ultra relativistic charged particles through magnetic fields in a circular storage ring. It is characterized by brightness and intensity several orders of magnitude higher than conventional X-ray sources, high collimation (i.e., small angular divergence of the beam), low emittance (i.e., the product of source cross section and solid angle of emission is small), widely tuneable in energy/wavelength by monochromatization and a high level of polarization (Rowe and Mills, 1973).

SR-XRD was used to follow changes in polymorphic forms in real time. It has made it possible to perform real-time (in situ) observations of polymorphic transformations. As a powerful probe, it has been used to determine the crystal morphology, phases, crystallization kinetics, and polymorphism of triglycerides and their binary mixtures (Minato, *et al.*, 1997). With a temperature control system and a shearing device attached, it is possible to perform crystallization experiments at rapid rates of temperature variation under shear. Mudge and Mazzanti (2009) reported the polymorphic transitions of the cocoa butter determined using synchrotron X-ray diffraction with an identical shearing system constructed of Lexan. However, access to synchrotron XRD is still limited to a select few laboratories around the world.

2.3. Crystallization under Shear

Shearing and tempering are widely used in the food industry during the fat crystallization with the famous example, chocolate. There is no doubt that chocolate quality is highly dependent on proper tempering and the shear applied. Similarly, processing conditions profoundly affect the consistency and spreadability of butter and margarine (Mazzanti, 2005). Therefore, understanding the crystallization kinetics associated with shearing would assist in process and equipment design and optimization for the entire food industry.

As a regular industrial manufacturing process, shear is used to enhance the rate of heat transfer, and to obtain a homogeneous final product in the industry as people discovered these benefits decades ago. Feuge *et al.* (1962) showed the mechanical working during the

crystallization of cocoa butter produced a quick transition to a more stable polymorphic form back to 1962; however, study of shear effects on the crystallization behaviour is still in the infancy with only a few such studies appearing recently, most of them studying on commercial fats and materials like milk fat, cocoa butter, chocolate and so on. This is a very new field and previously unknown and important phenomena have recently been shown to be common to major commercial fats.

Garbolino *et al.* (2000) applied ultrasonic measurements to the determination of the crystallization onset temperature of a sample of confectionery coating fat (hydrogenated and fractionated mixture of soybean and cottonseed oils) under shear since both of the common methods, differential scanning calorimetry (DSC) and nuclear magnetic resonance (NMR) methods, request specific instrumental designs to incorporate into a controlled shear device, which were difficult to achieve. With the inner cylinder of the rheometer programmed to rotate at constant rates (0, 64, 256, and 512 rpm), Garbolino's group managed to conclude that the onset temperature increased significantly with shear rate, implying lipid crystallization can be accelerated by mixing. They also claimed that there was a phase transition detected in the sheared sample as abrupt changes in all of the measured parameters. However, Saggin and Coupland (2004) believed that ultrasonic velocity and reflectance were strongly dependent on solid fat content but were not significantly affected by differences in crystal microstructure.

Commercial milk chocolate bars (30.2% fat, 7.0% protein, 58.1% carbohydrate) were investigated By Briggs (2003) to understand the crystallization kinetics associated with shearing. Treatments of two shear rates (15 and $30s^{-1}$) covering four tempering times using a controlled stress rheometer showed that a 100s time difference of the induction time between shear rate 15 and $30s^{-1}$, higher shear rate trigger the crystallization process early at the same tempering temperature.

In the work done by Mazzanti *et al.* (2003) dynamic and static experiments were carried out in a Couette shear cell consisting of two concentric cylinders with the inner one static while the outer one rotates. Different edible fats, cocoa butter, milk fat, stripped milk fat, and palm oil were studied on the shear effects on the crystallization behaviour and structure. Crystalline orientation and phase transition acceleration induced by shear (90 and $1400s^{-1}$) were demonstrated by using synchrotron X-ray diffraction. Later, the same researchers reported

similar shear-induced phase transition acceleration from α to β′ of palm oil under shear rates from 45 to 2880s^{-1}; however, there was no obvious change in the onset time of nucleation for phase α. They believed that the phase α nuclei forming many small crystallites which can easily transform to the β′ form under shear might be the explanation for the accelerated phase transition (Mazzanti, *et al.*, 2005). Another group (MacMillan, *et al.*, 2002) who studied cocoa butter got the same conclusion that increased shearing rate significantly raises the temperature at which the polymorphs are observed resulting in an associated reduction in induction times. However, the formation time of polymorph III remains relatively constant as shear rate increased (0.2 to 22s^{-1}). Much higher shear rate (45 to 720s^{-1}) was applied to cocoa butter showing accelerated phase transitions compared to static experiments according to Mudge and Mazzanti (2009). However, the viscous heating of the sample became not neglectable because that a shear rate of 720s^{-1} delayed phase transition in their work likely due to the temperature change.

Concentric cylinder viscometer was also chosen by Dhonsi and Stapley (2006) as a shearing device (shear rates from 1 to 50s^{-1}) and a monitor of viscosity measurement of mixtures of cocoa butter, sugar and lecithin. It was found that induction times were shear dependent at higher crystallization temperature (23ºC), with higher shear rates producing higher melting polymorphs. Similar results were demonstrated by Sonwai and Mackley (2006) that the induction time of cocoa butter form V to develop decreased from 31 to 21, 10, 6, and 0 min as the shear rate increased from 84 to 180, 240, 600, and 3000s^{-1}, respectively at 20°C. De Graef *et al.* proposed in their recent papers (2008, 2009) that using rheological parameters, the comparison between static and dynamic crystallization modes can be facilitated in terms of rheological variables. Shear can enhance nucleation and accelerate polymorphic transitions. Shear can also influence the further static crystallization process and alters the microstructural arrangement.

Besides the crystalline orientation and phase transition acceleration induced by shear reported by the aforementioned researches, different phases formed between the dynamic and static experiments of cocoa butter crystallization have also been discovered. It was first observed by MacMillan *et al.* (2002) that under static conditions, polymorphs III and IV were observed, while under sheared conditions (3 to 12s^{-1}) polymorphs III and V were present. Mazzanti *et al.* (2003) and Sonwai and Mackley (2006) groups found different phases present between the

dynamic and static conditions. However, they believed the initial phase was form II instead form III, or it was possible to have form II with the coexistence of form III. According to Guthrie (2008), the application of heat shear rates causes the formation of a compositionally different form V crystal with fewer defects than its lower/no shear counterparts. A prototype industrial laminar crystallizer has been recently designed (Maleky and Marangoni, 2008) to continuously crystallize edible fat in the desirable polymorphic form from the melt while being uniformly sheared.

Since shearing plays an important role in forming the structure of the crystal network and thus influencing its properties, studies on the shear effects on commercial edible fats are important to the food processing industry, whereas the complex natural fat components make it difficult to input a deeper scientific effort to explain the principles underlying the effects.

There is little study has been publish on the simplified mixture of triglycerides, which is the main components in most of the commercial fats, neither crystallization study under shear. This research based on the diluted binary mixture of triglycerides will provide valuable information for the new field as the first attempt.

2.4. Rheological Properties of Fat Dispersion in Circular Couette System

It has been commonly accepted recently that rheological data may be used to infer indirectly the influence of shear on crystallization through changes in apparent viscosity, or more directly, measured torque. The rheological data can be used to further examine the shear acceleration effect over a large range of temperature conditions and elucidate the effect of shear on the acceleration of the phase transformation.

There have been a very large number of experimental and theoretical studies of flow between concentric rotating cylinders (circular Couette flow) in the century since the earliest studies were conducted by Mallock (1888, 1896) and Couette (1890), yet not much for the edible fats industry. Most of these studies were focusing on shear effect on suspensions of hard spheres in a circular Couette system during crystallization. Some of them concluded that the nucleation rate enhanced of a shear-induced ordering (Ackerson and Pusey, 1988, Haw, *et al.*, 1998) whereas others concluded that shear suppressed crystallization (Palberg, *et al.*, 1995, Okubo and

Ishiki, 1999). The two opposite phenomena were tried to be explained by Blaak, *et al.*, (2004) that shear may induce layering in the fluid facilitating nucleation process while it may also remove matter from small crystals suppressing the birth of crystals.

However, fat dispersion during crystallization, whose crystal is now known to be platelet shaped(Acevedo and Marangoni, 2010), seems to act different from the suspensions of hard spheres that only shear-induced acceleration being reported. Garbolino *et al.* (2000) reported that the torque readings of the liquid oil are low, however, at the crystallization point, the torque increased suddenly, corresponding to the formation of a solid-in-liquid fat dispersion. The sample of confectionery coating fat behaves as non-Newtonian fluid when partially crystallized. The rheometer they used in their work was not sensitive enough to record any changes of the torque readings due to temperature. Conventionally, crystallization would be expected to initiate at the coolest part of the sample. Surprisingly, in their experiments, crystallization was initiated at the moving inner cylinder where had the highest shear rate despite the inevitable temperature gradient inferred from the reverse of sequence of echo amplitude and torque. Briggs (2003) demonstrated that traditional rheological methods may be used as a tool to investigate indirectly crystallization and directly flow properties of molten chocolate with some limitations, which is primarily excessive contraction, at higher shear rates. Toro-Vazquez *et al.* (2004) used a dynamic mechanical spectrometer to investigate the crystallization of cocoa butter under static as well as dynamic conditions. The Rheological approach led them to conclude a shear rate effect favoured cocoa butter development in the β phase, while no β phase developed under static conditions. De Graef group believe oscillatory rheology is a valuable complementary method to evaluate primary crystallization. Comparison of oscillatory rheology with DSC and pNMR (2006) elucidated that oscillatory rheology was capable of differentiating the process stages occurs just like DSC and pNMR. In their following papers (2008, 2009), it has been reiterated that the comparison between static and dynamic crystallization modes can be evaluated in terms of rheological variables. The apparent viscosity of the palm oil increased significantly at increasing isothermal time under shear when the shearing at 1 and $10s^{-1}$, while for $100s^{-1}$ only a minor increase could be noted. The obtained results were compared with crystallization data obtained via X-ray diffraction and polarized light microscopy. However, De Graef pointed out that comparison between results must be done with caution. Differences in sample weight or volume,

equipment design and its impact on the thermodynamics of the system may affect crystallization to a different extent.

2.4.1.The Flow Stability of Fat Dispersion in Circular Couette System

Shear thinning behaviour is exhibited by high polymers, polymer solutions, and many suspensions. A solid-in-liquid fat dispersion is a non-Newtonian fluid with shear thinning properties. One concern need to be noted here is that when the shear rate applied to the system is increased, instabilities in the flow may appear. Furthermore, the properties of non-Newtonian fluid make it more complicated to predict the flow behaviours. Lockett, *et al.* (1992) found that the shear-thinning behaviour of the fluid has a significant effect on the critical Taylor number.

Researches on different flow regimes in a circular Couette system revealed a surprisingly large variety of different flow states, including Taylor vortices, wavy vortices, modulated wavy vortices, and so on (Andereck, *et al.*, 1986, Pascal, 1993). These states were determined as functions of the inner and outer-cylinder Reynolds numbers:

$$R_i = \frac{r_i(r_o - r_i)\Omega_i}{\nu} \tag{6}$$

$$R_o = \frac{r_o(r_o - r_i)\Omega_o}{\nu} \tag{7}$$

where r_i (r_o) is the radius of the inner (outer) cylinder, Ω_i (Ω_o) is the angular velocity of the inner (outer) cylinder and ν is the kinematic viscosity. The other parameters in a circular Couette system then can be calculated as:

Rotary Reynolds number:

$$Re = \frac{\rho R_i \Omega (R_o - R_i)}{\mu} \tag{8}$$

Taylor number:

$$Ta = \frac{\rho^2 \Omega^2 R_i (R_o - R_i)^3}{\mu^2} \tag{9}$$

If the Taylor number has reached the critical value of Taylor vortex flow, T_{ac}, which means the flow in the Couette system becomes unstable and a secondary steady state characterized by axisymmetric toroidal vortices, known as Taylor vortex flow, emerges (Taylor,

1923). Different annulus ratio values $\eta = \frac{r_i}{r_o}$ have different T_{ac} values, $Ta_{crit} \cong 1708$ for $\eta \rightarrow 1$; $Re_{crit} = 71.7$ for $\eta = 0.60$; $Re_{crit} = 79.5$ for $\eta = 0.70$ (Recktenwald, *et al.*, 1993). In this work, it is unlikely that any instability in the flow appear due to a Taylor number smaller than the critical value.

2.4.2.Models of Suspension Viscosity

Many suspensions of rigid spherical particles are known to exhibit non-Newtonian viscosity most of which decreases with increasing rate of shear. This behaviour has been attributed to mechanisms in which the effects of Brownian motion of the suspended particles disturbed by the shear stress. There were several different models presented on viscosity of concentrated suspensions of rigid spherical particles. A large amount of data was also analyzed to support these models.

Mooney (1951) extended the Einstein's viscosity equation for an infinitely dilute suspension of spheres to apply to a suspension of finite concentration.

$$\ln\left(\frac{\eta}{\eta_s}\right) = [\eta]\nu/(1 - \frac{\nu}{p}) \tag{10}$$

where η is the apparent viscosity of suspension, η_s is the apparent viscosity of the continuous phase (or liquid phase), $[\eta]$ is the intrinsic viscosity of the medium (or solid phase), ν is volume fraction and p is called the packing fraction since the approach to infinite viscosity is usually ascribed to the attainment of the close-packed structure.

Krieger and Dougherty (1959) modified Mooney's functional analysis to be

$$\frac{\eta}{\eta_s} = (1 - \frac{\phi}{\phi_M})^{-[\eta]\phi_M} \tag{11}$$

where Φ is the concentration of solids (by volume), and ϕ_M is the maximum solids concentration (by volume).

The Krieger–Dougherty model has been shown to provide an excellent fit to data obtained for model systems (Papir and Krieger, 1970, Woods and Krieger, 1970, DeKruif, *et al.*, 1985). It is an excellent fit over the entire range between η_0 and η_∞. Comparing to several different models together with the experimental data of Latex spheres (rigid spheres), Wildemuth and Williams (1984) concluded that the Krieger-Dougherty model was the most successful one.

It has also been applied to more complex systems, like ground particles, glass rods and fibers, as reviewed by Barnes *et al.* (1989).

The maximum volume fraction ϕ_M depends on particle-size distribution and shape. It should be noted that ϕ_M is affected not by particle size, but rather by the particle-size distribution. The maximum volume fraction typically falls between 0.6 and 0.7 for mono-sized spherical particles (Larson, 1999). The intrinsic viscosity $[\eta]$ is a measure of a solute's contribution to the viscosity η of a solution. It is defined as follows:

$$[\eta] = \lim_{\phi \to 0} \frac{\frac{\eta}{\eta_s} - 1}{\phi} \tag{12}$$

where η is the viscosity of a solution, η_s is the viscosity in the absence of the solute and ϕ is the volume fraction of the solute in the solution.

The intrinsic viscosity value depends on particle size and shape. Big particles in the suspension cause large intrinsic viscosity values (Larson, 1999), so does the large aspect ratio. In this work, the intrinsic viscosity values found from the Krieger-Dougherty model provided more information of the crystal size and shape.

CHAPTER 3 EXPERIMENTAL METHODS AND MATERIALS

3.1. Research Plan

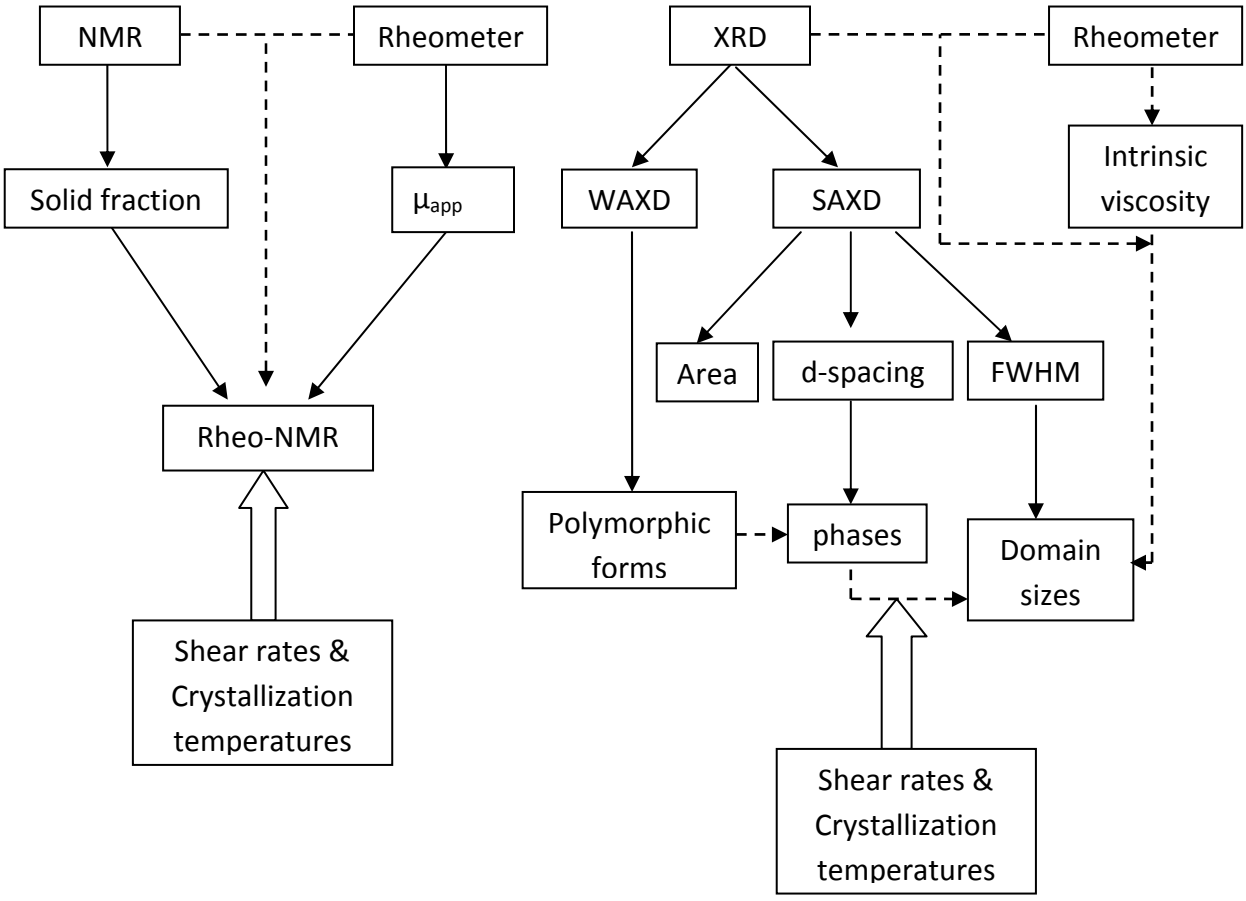

3.2. Materials

3.2.1.Sample Identification

This research was conducted using the pure triglycerides trilaurin and trimyristin and their binary mixtures. These triglycerides (TAGs) were chosen because they are extensively distributed in nature and have lower melting points compared to other more common TAGs such as tristearin and tripalmitin. In addition, these TAGs have consecutive chain length carbon numbers (12 and 14) which favours the formation of solid solutions. Both of these triglycerides are utilized in the cosmetic, pharmaceutical and food industries. Triolein was chosen as the liquid solvent, since it is very common in nature and has a melting point in the β phase of 4°C. This system thus makes a simple ternary system in which two of the triglycerides do actually crystallize while the other remains liquid. This system is expected to mimic a natural system that often has mixtures of hard (solid) and soft (liquid) triglycerides. The dilution was also intended to allow the study of the effect of shear flow during the crystallization, since there is enough liquid to keep the material in a flowing state.

3.2.2.Sample Preparation

Trilaurin (LLL), trimyristin (MMM) and triolein (OOO) samples with more than 99% purity were obtained from Sigma-Aldrich Chemical Co. and used without further purification. The binary mixtures of LLL/MMM were prepared by melting the mixtures of weighted samples in 20% intervals in composition on a weight per weight basis. The LLL: MMM ratios were 30:70, 50:50 and 70:30, denoted 3L7M, 5L5M and 7L3M. These mixtures were diluted with 60% or 40% triolein by weight to obtain samples with 40% or 60% solids, i.e. 3L7M40, 3L7M60. Pure individual triglycerides samples trilaurin and trimyristin diluted in triolein were also studied.

3.3. X-ray Diffraction Measurements

X-ray diffraction (XRD) measurements were performed at the ExxonMobil beam line X10A at the National Synchrotron Light Source (NSLS, Brookhaven National Laboratory, Upton, NY, US) to detect the whole crystallization process (Figure 3-1).

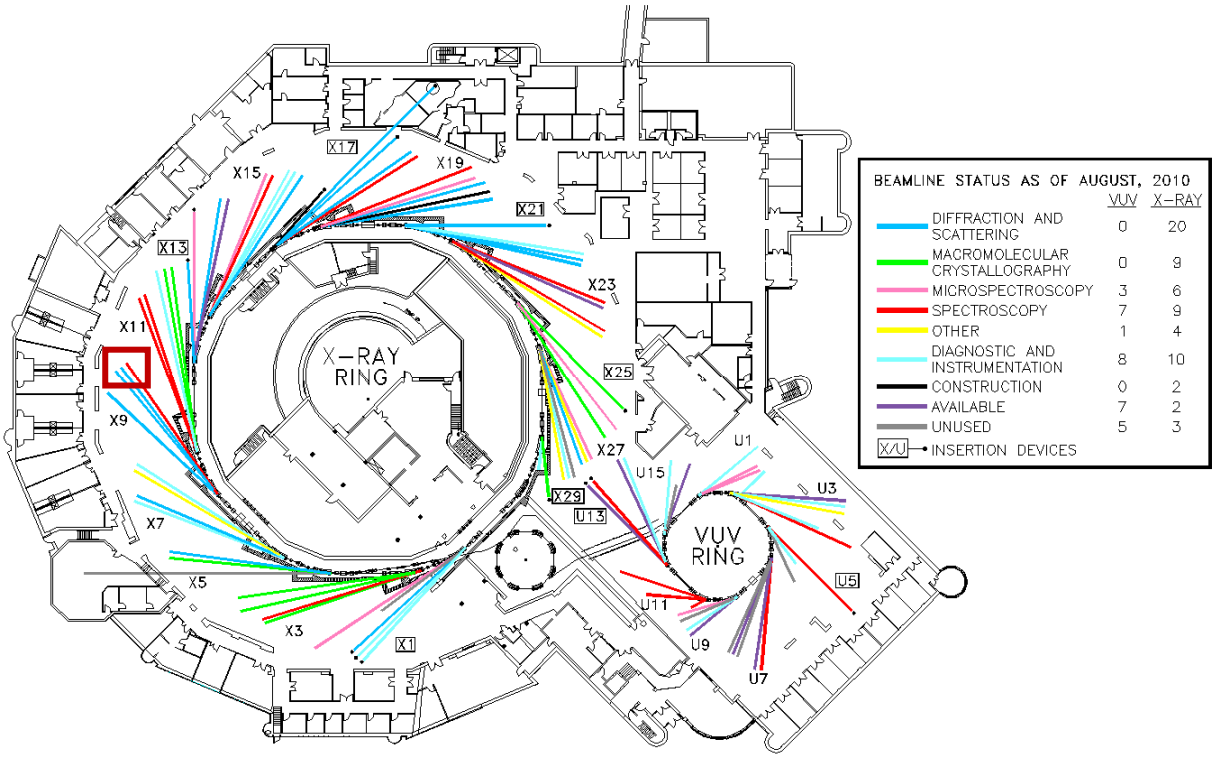

Figure 3-1 Image of the Brookhaven National Laboratory National Synchrotron Light Source showing the beam line status (BNLWebsite).

3.3.1.X-ray Beam Line Information

The synchrotron produces light by accelerating electrons to almost the speed of light. Magnets put the electrons into circular paths. As the electrons turn, photons (little packets) of light are given off. The infrared, UV, and X-rays are sent down pipes called beam lines, to work hutches where researchers run their experiments. The components of the NSLS synchrotron include an electron gun, linear accelerator, a circular booster ring (to increase the speed of the electrons), two storage rings (to circulate electrons), and beam lines. When this bright light is

aimed at a very small sample, an image of the sample's scattering properties is created on a detector camera.

The beam line has energy range of 8-17 KeV. The exact energy is selected using a monochromator with two parallel crystal surfaces. A set of mirrors aligns the beam, and then it is collimated by a set of slits. The beam is further defined downstream with two sets of slits so that when it reaches the hutch it has a size of 0.5 by 0.5 mm. Its wavelength during our experiments was $\lambda = 1.097$Å. Images of the diffraction patterns were collected to a computer by Bruker-AXS SMART software, which controls the SMART 1500 2D CCD detector camera. The distance from the sample to the detector was 1096mm for small angle XRD measurements and 90mm for wide angle ones. This distance was calibrated with silver behenate in the form (Ag-Beh), which has known d-spacings. The wavelength was calibrated using Al2O3 in a capillary and a point detector on a rotating arm centered at the crossing between the beam and the capillary. The image data were then analyzed to study the nanostructures and some microstructural aspects of the crystallizing samples.

Electromagnetic radiation, such as a beam of X-rays, carries energy. The rate of flow of this energy through unit area perpendicular to the direction of motion of the wave is called the intensity I. In absolute units, intensity is measured in $\text{joules}/\text{m}^2/\text{sec}$. However, this measurement is difficult to be carried out. Most X-ray intensity measurements are made on a relative basis in arbitrary units, such as the degree of blackening of a photographic film exposed to the X-ray beam (Cullity and Stock, 1978). Therefore, the X-ray intensity of the measurement has been presented in arbitrary unit (a. u.) in this work. Because the units were normalized to the intensity of the incident beam, they will be denoted normalized units (n. u.).

The angular resolution of the incident beam is not perfect, so the beam has a narrow but finite distribution of incident angles, which causes a broadened peak shaped diffraction pattern obtained instead of a sharp one. The broadened peak is characterized by its amplitude and a finite full width at half maximum (FWHM), seen in Figure 3-2. The FWHM of the diffraction peak is broadened by the small crystallite size and by the imperfections of the crystallite, which result in an effective coherence length of the size of the scattering domain.

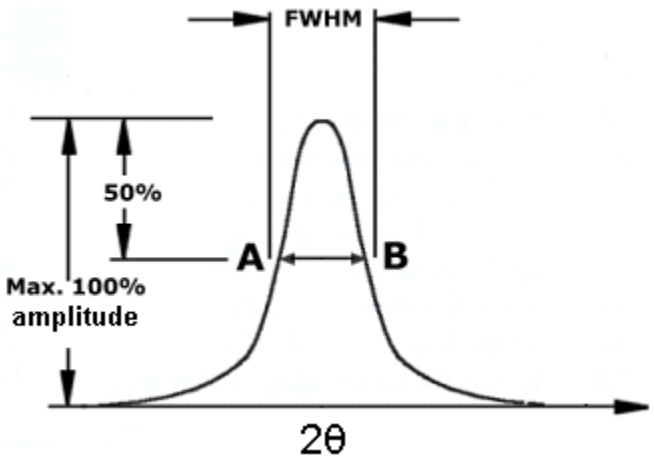

Figure 3-2 Characteristic parameters amplitude and FWHM of the intensity peak produced by X-ray scattering from a crystalline material.

The broadening due to crystal size, in a plot using 2θ as x coordinates, is given by Scherrer's approximation (Cullity and Stock, 1978):

$$\xi = \frac{K\lambda}{\beta\cos\theta} \tag{13}$$

where ξ is the mean size of the ordered (crystalline) domains, K is the shape factor, which has a typical value of about 0.9, λ is the x-ray wavelength, β is the line broadening at half the maximum intensity (FWHM) in radians, and θ is the Bragg angle.

Perfect big crystals generate narrow diffraction peaks through X-ray diffraction measurements whereas smaller or distorted crystals broaden the peaks. The difference between the two FWHM values in radians is described by β:

$$\beta = \mathrm{FWHM} - \mathrm{FWHM_p} \tag{14}$$

where $\mathrm{FWHM_p}$ is the full width at half maximum of a perfect crystal in the synchrotron very narrow beam, which makes its value negligible. Hence,

$$\beta \approx \mathrm{FWHM} \tag{15}$$

The Bragg angle, θ, in small angle X-ray diffraction measurements of this work is smaller that 1.5°.

$$\cos\theta \geq \cos(1.5°) = 0.99966 \tag{16}$$

So in this work, $\cos\theta$ value can be estimated as 1 for SAXD measurements.

Also $\sin\theta \approx \theta$ in radian when $\theta \leq 1.5^{\circ}$. Then,

$$q = \frac{4\pi}{\lambda} \cdot \sin\theta = \frac{4\pi}{\lambda} \cdot \theta \tag{17}$$

$$\Delta q = \frac{4\pi}{\lambda} \cdot \frac{\Delta(2\theta)}{2} = \frac{2\pi}{\lambda} \Delta(2\theta) \tag{18}$$

From Figure 3-2, it is clear to see that:

$$\Delta(2\theta) = \frac{\Delta q \lambda}{2\pi} = \mathrm{FWHM} \tag{19}$$

$$\xi = \frac{K\lambda}{\beta\cos\theta} = \frac{K\lambda}{\mathrm{FWHM}} = \frac{K \cdot 2\pi}{\Delta q} \tag{20}$$

The value of β was overestimated when the FWHM values of a perfect crystal was assumed as neglectable, thus $K = 1.0$ was chosen instead of value of about 0.9.

For the purpose of this thesis, the coherence length of the domains, ξ, can be estimated as:

$$\xi = \frac{2\pi}{\Delta q} \tag{21}$$

where Δq is the FWHM of the diffraction peak in q. In this work, the FWHM values represented the thickness of the domains in the direction perpendicular to the lamellae, and therefore corresponding to the smallest dimensional length of the platelet crystallites.

3.3.2.Sample Treatment for XRD Measurements

Each sample was cooled at 10°C/min from the melt at 60°C down to different crystallization temperatures between 10 and 30°C according to our estimates of the melting point for each sample depending on its composition. Then, each sample was left to crystallize both statically and under shear rates of 8, 80, 800s^{-1}. These values came from having an upper limit at the maximum speed of the rheometer at 800s^{-1} and taking two log10 reductions from it. After a certain amount of time at the crystallization temperature, normally 35 minutes for sheared

experiments and 50 minutes for static ones, the sample was heated up back to 60°C to destroy all the crystal memory and get ready for the next cycle. It was called "a cycle" for one experiment when it started from the melt to crystallization and back to the melt again. The scattering images were taken and recorded every 1.05 minutes during each cycle.

In order to define a reasonable set of crystallization temperatures for each sample, pre-tests were performed in a differential scanning calorimeter (DSC) instrument (TA instruments, Q SeriesTM 100). Crystallization is known as an exothermic process. The shape and the pattern of the exothermic peak carry some information about the crystallization process. Since this work was focusing on the observation during this process, it is designed to gather as much information as possible. This is easier to do if the measuring temperature produces a slowly rising exothermic peak. Additionally, as the time in NSLS is valuable, the experiments were designed to be finished in a reasonable amount of time, which means the crystallization process can not happen too slowly, either. Eventually, three different crystallization temperatures were chosen for each sample, which are listed in the table. The formation of the most unstable polymorph, α, if possible, was tried to be avoided in this work. Since α form appearing in 5L5M40 at 11°C, the planned temperatures for 7L3M40 and LLL40 were then decided to increase.

Table 3-1 Summary of the crystallization temperatures for each sample in the XRD experiments

Sample	Crystallization temperatures (°C)		
LLL40	12	14	16
7L3M40	12	14	16
5L5M40	11	14	17
3L7M40	15	18	21
MMM40	25	27	29

3.3.3.Couette System Configuration

3.3.3.1.Anton Paar DSR301 Measuring Head

A DSR301 measuring head (Rheometer) from Anton Paar Co. was installed into the X-ray hutch for all the quiescent and dynamic XRD experiments. The modular device consists of a

measuring head, which is equipped with a powerful, synchronous EC motor and high-precision air bearing technology, and a separate control unit. The motor drives a long shaft made of aluminum with a Lexan end to spin at a given shear rate or to oscillate at certain frequency depending on different experimental needs. The measuring head is able to measure various parameters. The ones needed for dynamic experiments were velocity (that translated into shear rate) and torque (that can be translated into shear stress).

Rheoplus is the software offered by Anton Paar Co. for the device control and data collection. Once the rheometer is initialized, a new measurement can be added in the Rheoplus software. In the "Measurement" window, the values of shear rate and experiment time needed to be set up first before performing experiments. The information includes shear rate, measure points (how many points of data needed) and interval (the time for a certain shear rate). The experiments under shear required a constant shear rate for each cycle.

3.3.3.2.Temperature Control units

In the previous works of our group, the initial Rheo-NMR prototype did not have a temperature control system with the shearing device. There was no the option of temperatures other than a fixed temperature near 40°C held by a thermostat inside the NMR. Hence, the test material chosen was a high melting point material, a blend of fully hydrogenated canola oil and liquid canola (Mazzanti, *et al.*, 2008). However, the temperature control system is essential for inducing crystallization of low melting point materials since it cannot occur at the now fixed 40°C of the pNMR, or at the room temperature (about 28°C) in the X-ray hutch. Furthermore, to achieve a constant cooling/heating rate during fat crystallization requires a well-designed temperature control system. A temperature system was later designed and built for these purposes as described by Mudge and Mazzanti (2009). Now, the new measuring head device introduced into this system made it possible to obtain rheological data during crystallization under shear for the purpose of this work.

The temperature control system is comprised of a temperature controller (5R001 Oven Industries, US), a water bath (Cole-Parmer Instrument Company®, Model: Polystat® R6L), an active heat exchanger, a Galden reservoir, a peristaltic pump (Cole-Parmer Instrument

Company®, Model: Masterflex® Tubing Pump) for Galden fluid, a thermistor and a fiber optic temperature sensor (Neoptix). The Galden fluid was chosen because of the hydrogen-free property not affecting the NMR readings, the low relative viscosity, and the wide operating temperature range which permits them to act as heat transfer liquids in extreme temperature conditions (0-70°C).

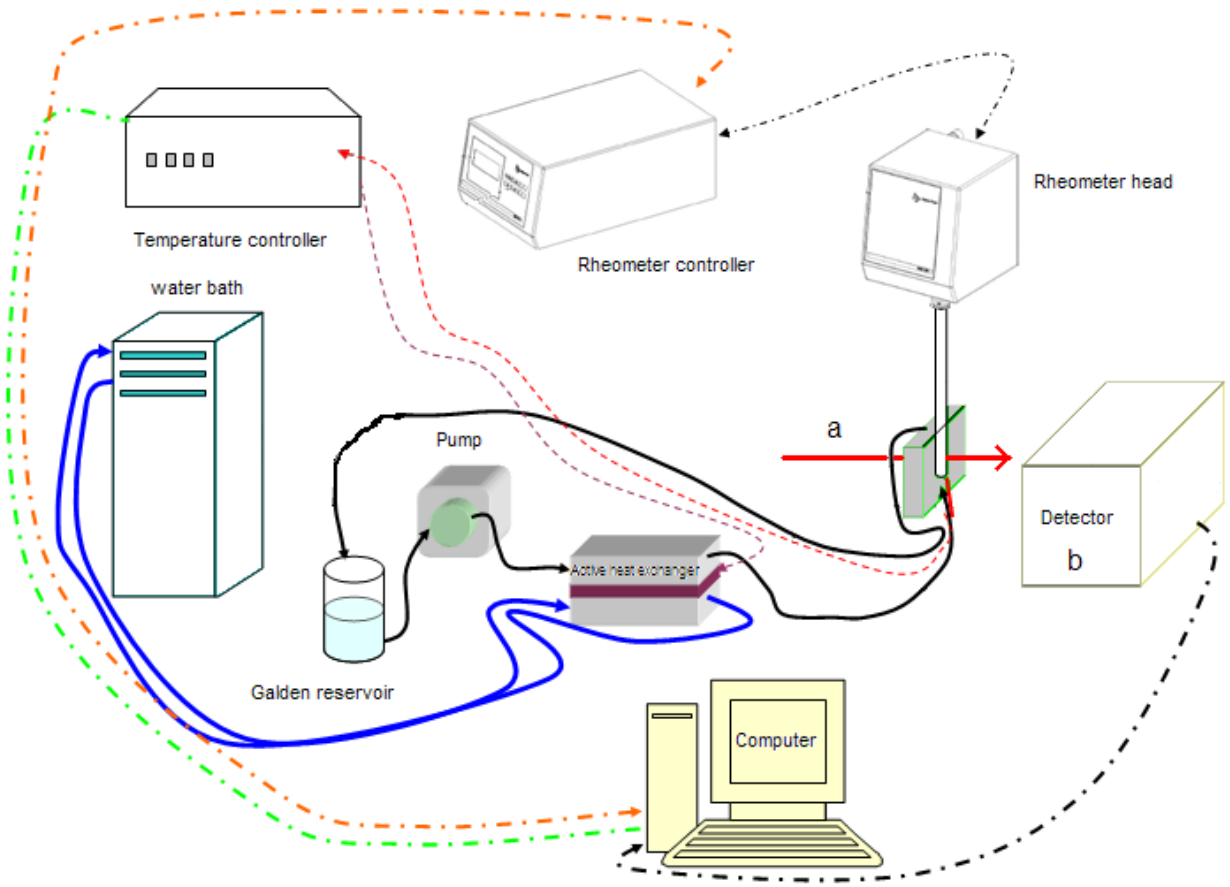

Figure 3-3 Schematic figures of the Couette system configuration. The two measuring systems, rheo-NMR and X-ray diffraction used in this work share most of the Couette system. The two differences are: a, in the figure is X-ray in the XRD measurement and is the NMR magnetic field direction in the rheo-NMR system; b, detector is CCD camera in the XRD system and is the NMR electronics in the rheo-NMR system. (Drawing by E. M. Mudge from a research report, 2008)

Temperature Controller

This device connected to a PC computer allows communication between the software and the temperature control system. It can be controlled via either LabVIEW or individual software

named “CONTROLLER MR001”, which gave commands to the temperature controller and read the feedback from it using a serial port.

Water Bath

The water fluid is connected to the heat unit for transferring the thermal energy from it. The temperature of the water bath was set at 12°C. The pipes between the water bath and the heat unit were insulated for thermal loss minimization.

Active Heat Exchanger

The heat unit is connected to the temperature controller and following its commands. There are three thermoelectric coolers (TECs) (Model: HT8-12-F2-4040-TA-RTW6, Laird Technologies, Cleveland, OH, US) built in the heat unit for heat transfer between the water and Galden fluids and the precise temperature control of the Couette system.

These ceramic plate high temperature (Wright*, et al.*, 2000) thermoelectric coolers are assembled with Bismuth Telluride semiconductor material and thermally conductive Aluminum Oxide ceramics. They were connected in parallel in the system with a 13 volt power supply and the circuit has a fuse as a protection.

Galden Heat Transfer Fluid System

Galden® heat transfer fluid is a perfluorinated polyether without hydrogen, producing no effect on the NMR signal. Grade HT135 (Solvay-Solexis) was chosen in this work because of its low viscosity (1.00 cSt) and wide operating temperature range from -50 to 125°C with a boiling point at 135°C, which permits it to act as heat transfer liquid in our working temperature conditions (0-70°C). Its thermal conductivity however is low, ca. 0.017 W/m·K.

The Galden fluid is kept in a stainless steel thermos with a glass condenser on top avoid evaporation yet prevent pressurization of the system. The Galden fluid is pumped by a peristaltic pump through the heat exchange unit and then reaches the sample holder. After flowing through the outside cylinder, the Galden fluid goes back to the container. The pipes between the heat exchanger to the sample holder were insulated for thermal loss minimization.

Fiber Optic Temperature Sensor

A fiber optic temperature sensor was chosen for several reasons. First of all, there is no metal part in the sensor, meaning no electrical power going through it. Thus, this temperature probe is not affected by, and does not affect the magnetic and radio frequency of the NMR. Second, the small size of the fiber optic temperature sensor allows us to locate it at the bottom of the sample holder to detect the temperature of Galden fluid at the entrance. Last but not least, it is controllable from a computer. The computer reads the temperature as a voltage signal (0 to10V), converts it to temperature (-20 to 100°C) and displays in the program compiled in LabVIEW software. Then a PID algorithm compiled in the program will calculate the voltage output to the TEC units, delivering the thermal energy exchange in the heat unit once the temperature controller got the feedback from the fiber optic device. The temperature reading is also on the screen of the fiber optic device.

Couette Cell

Dynamic and static experiments were carried out in a Couette cell as sample holder. It consists of two concentric cylinders made of Lexan® walls. 1.7 mL of sample was put into the internal cylinder. The calculation of the sample volume is in the appendix. The Galden fluid went through the gap between the inner and outer cylinder for temperature control. The shaft of the measuring head rotated, driven by the rheometer motor to produce a uniform shear in the sample fluid placed in the gap between the shaft and the internal cylinder. The NMR system used a glass sample tube to avoid any potential signal affecting the NMR device, while the Lexan sample tube was used in the XRD system because it allowed x-rays to go through.

Table 3-2 Summary of the features of the Couette cells in NMR and XRD system

	Outer cylinder		Inner cylinder	
	Material	Inside diameter	Material	Outside diameter
NMR	Glass	13.0mm	Glass	10.0mm
XRD	Lexan	13.0mm	Lexan	10.0mm

3.3.3.3.2D CCD Detector Camera

The 2D CCD camera had a plate of phosphor material at the very front reacting to different intensities of X-ray it received. The photo-reaction of phosphor material translated the X-ray intensity into a visible light signal that was transmitted by a bundle of tapered fibre optics located after the phosphor material. These fibre optics were extended and thinned at only one side so the size of the scattering ring is reduced dramatically by simply transferring through the tapered bundle. The small size of the bundle is coupled to a CCD chip that records the image on a 1024x1024 chip, which was 2x2 binned in our case to give a 512 x 512 pixels frame. The bundle was built so the detector camera could get the image at the right size of the CCD chip, but unfortunately it also causes some distortion during the transmission. This distortion is called warping. One function of the SMART software was to correct the misplaced pixel information by unwarping the images, recalculating the intensity of the right places in each image. A program was developed for this work to use the SMART unwarping routine.

3.4. Nuclear Magnetic Resonance Measurement

3.4.1. Rheo-NMR System Configuration

The current rheo-NMR system was designed for this research and the ones in the future in the lab at Dalhousie University. The project was directed and supervised by Dr. Mazzanti and performed by Mengyu Li and two groups of undergraduate students. The rheo-NMR system consists of a low-field table-top NMR device and the same measuring head (rheometer) used in the XRD measurements. By building the rheo-NMR system, it became possible to obtain the solid/liquid ratio of the sample from the NMR signals and the rheological information of the sample from the rheometer at the same time during experiments.

3.4.1.1. Nuclear Magnetic Resonance Device Bruker IBM PC/20B

The IBM-Bruker PC/20B NMR Analyzer (Minispec) was used in this research providing the automatic measurement of solid/liquid ratios in fat samples. The 90° pulse duration is typically 0.3 μs, and the dead time of the receiver is 0.7 μs. It operates at 20MHz (0.47T correspond to the resonance of H at 20 MHz), by beaming one or more radiofrequency pulses into a sample of the material to be analyzed; examining the resulting NMR signal from protons in the sample; and displaying the calculated quantity of interest to the user (NMR Manual).

3.4.1.2. Sample Holder and the 2-Dimension Motion Stage

A sample cell made of non-magnetic material (Aluminum) was located in between the two magnet poles with a hole in the middle for holding sample container. A 10mm glass tube with sample inside can then be introduced into that hole. With Galden fluid flowing surrounding the tube, the temperature was determined by the temperature control system.

The sample tube was located at the bottom of the measuring head connected by a metal ring screw to the measuring head, which was sitting on a trestle that was position controlled by a vertical motion stage. There are two motors moving the whole structure horizontally or vertically, controlled by another LabVIEW program written by Dr. Mazzanti. The position of the measuring head can be adjusted by the 2-dimension stage. Connected with the rheometer, the sample tube can be exactly located. This stage also facilitates the procedures of sample changes.

Normally, NMR is a rather sensitive method since it is capable of detecting these very small population differences. It is the resonance, or exchange of energy at a specific frequency between the spins and the spectrometer, which gives NMR its sensitivity. In this work, the NMR instrument had to be modified to fit with the rheo-NMR system built for the measurements, where the signal was reduced by all the extra structures added to it including the temperature control system and the shearing device, as shown in Figure 3-4.

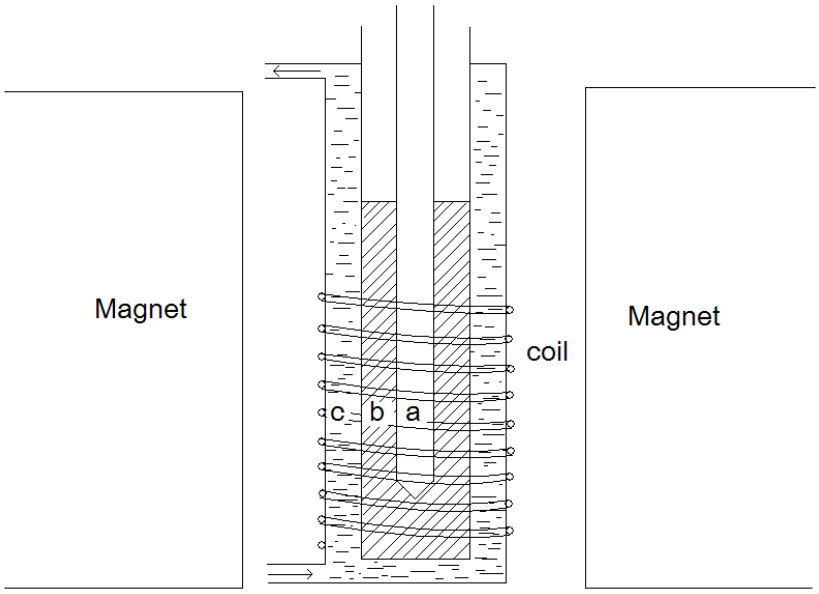

Figure 3-4 Schematic diagram of Couette system built in the Rheo-NMR system. **a** is the rheometer shalf made of Lexan, **b** is fat sample, and **c** is Galden fluid surrounded the sample tube for temperature control.

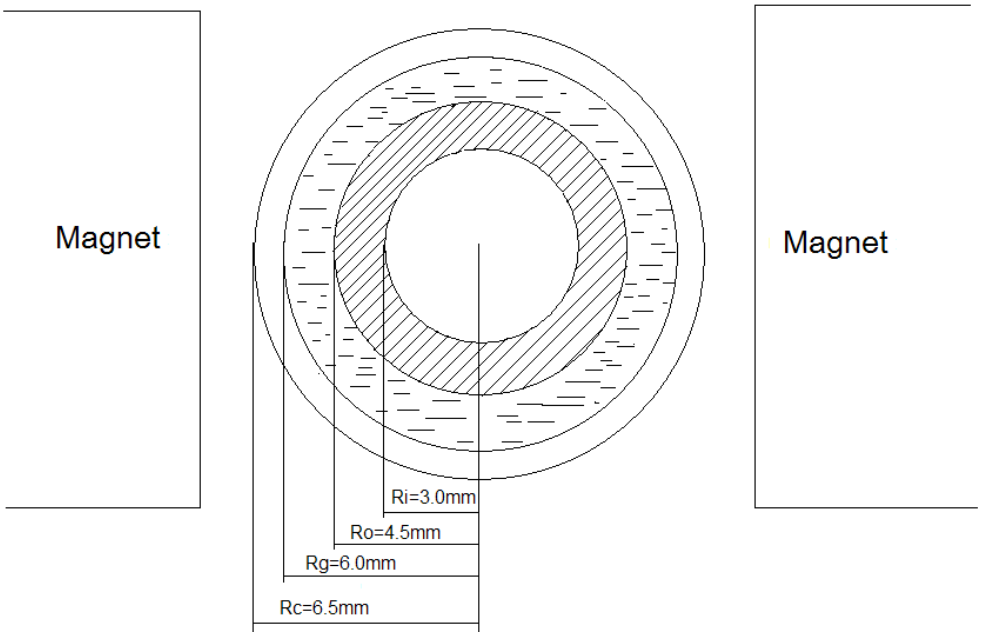

Figure 3-5 Schematic diagram of the Couette cylindrical rheometer from the top of the NMR instrument. The radius of the shaft is $\boldsymbol{R_i}$ =3.0mm. $\boldsymbol{R_o}$, which is the inner radius of the 10.0mm glass sample tube, is assumed to be 4.5mm. Outside the sample tube, the Galden fluid flows in a tube with a radius $\boldsymbol{R_g}$ of 6.0mm. The coil is chosen to use in this research is $\boldsymbol{R_c}$ =6.5mm.

Assume in a normal case, a 13.0 mm diameter sample tube has an inner diameter of 12.0 mm, which needs the volume of sample:

$$\mathrm{Vn} = \pi \cdot \mathrm{Rn}^2 \cdot \mathrm{H} = \pi \cdot (6.0\mathrm{mm})^2 \cdot \mathrm{H} \tag{22}$$

In this work, a 10.0 mm sample tube is used (inner diameter is 9.0 mm) with a 6.0mm shaft in the middle of the sample, so that the cooling fluid in the outer annulus can be circulated in the gap. Assuming the height of the sample in both cases is the same, then the volume of sample in our case:

$$\mathrm{Vo} = \pi \cdot (\mathrm{Ro}^2 - \mathrm{Ri}^2) \cdot \mathrm{H} = \pi \cdot (4.5\mathrm{mm}^2 - 3.0\mathrm{mm}^2) \cdot \mathrm{H} \tag{23}$$

The ratio between $\mathrm{V_o}$ and $\mathrm{V_n}$ represents the ratio of the amount of sample which can produce NMR signals.

$$\frac{\mathrm{Vo}}{\mathrm{Vn}} = \frac{\pi \cdot (4.5\mathrm{mm}^2 - 3.0\mathrm{mm}^2) \cdot \mathrm{H}}{\pi \cdot (6.0\mathrm{mm})^2 \cdot \mathrm{H}} = 0.3125 \tag{24}$$

From the calculation, the NMR signal in this research is reduced to about one third with respect to a full tube, which is the major loss of the signal strength.

To compensate the sensitivity loss, all the signal readings from the solid and liquid regions were averaged, instead of picking point S and L as the signal values. Furthermore, the constant value of the liquid signal calibration was found to be 1.017 by testing the standard samples given solid fraction from Bruker Corporation. It has been found that the liquid signal was stronger at the beginning and was weaken at the end of the measurement time. The correction of the two different signal values was a constant 1.017 (Figure 3-6).

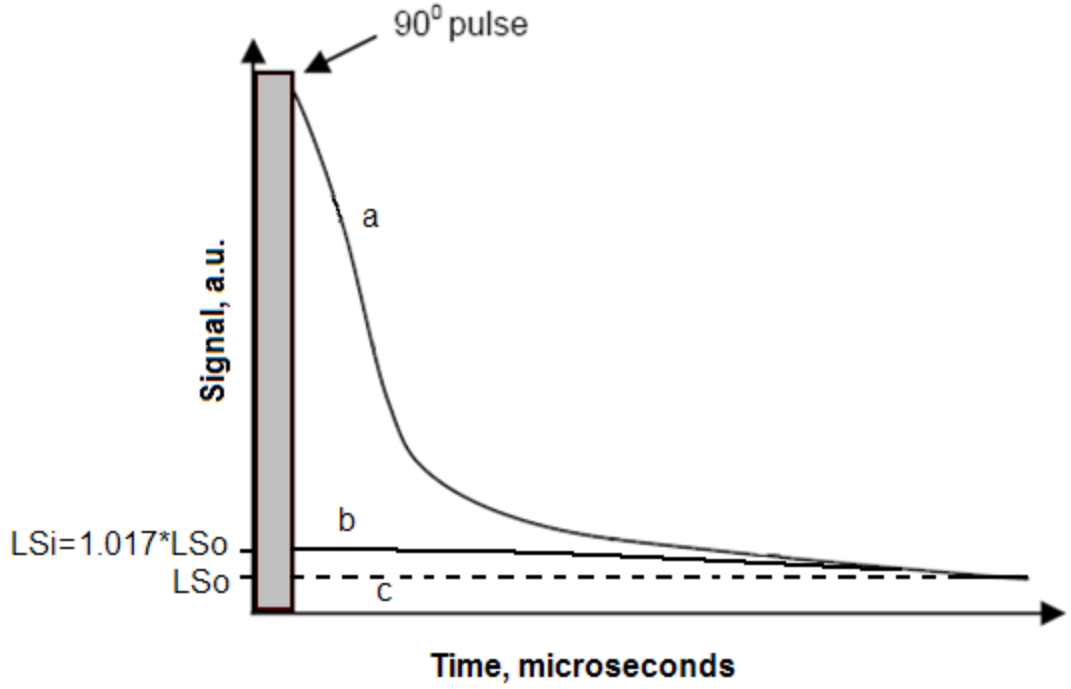

Figure 3-6 The liquid signal calibration constant 1.017 was found by comparing the initial liquid signal LSi to the liquid signal offset LSo. Curve "a" shows NMR signal of a standard sample with solid component. Curve "b" shows NMR signal of a pure liquid sample. The signal still reduces with the time prolongs, which eventually reaches the offset value line "c".

The liquid signal value correction should be included in the function of solid fraction, also two other factors: the offset value of the liquid signal, and the solid background signal produced by the Lexan shaft of the rheometer. The modified equation for obtaining solid fraction is:

$$\mathrm{SF}(\%) = \frac{\mathrm{SS} - \mathrm{SBC}}{(\mathrm{SS} - \mathrm{SBC}) + (\mathrm{LS} - \mathrm{OF}) \times 1.017} \times 100 \tag{25}$$

where SF is solid fraction, SS is solid signal, LS is liquid signal, OF is the offset value of liquid signal, the constant 1.017 is the liquid signal calibration value, and SBC is solid background signal. These values were obtained by fitting both the solid and liquid signals with Gaussian functions (Details provided in Appendix A). The rheometer shaft of the rheo-NMR system in this work was placed into the glass sample tube for both the static and shear experiments. The part of the shaft in the sample tube is made of Lexan, a polycarbonate resin thermoplastic, which

generates some solid signal in the NMR since there are hydrogen atoms in it. The signal of the Lexan shaft, adding a solid signal background to the solid signal of samples, has a considerable effect on the solid signal reading in total, which is the sum of the solid signals of the sample and the shaft. Hence, the solid signal from the Lexan shaft needs to be subtracted as a background value. Since the samples in this work contain 40% crystallizable materials and 60% solvent, SF value at the final stage of the crystallization should be close to 40.

3.4.2.Rheo-NMR Calibrations

After a pulse or pulse sequence has changed the magnetic alignment of the billions of nuclei in the sample, they transmit weak radio frequency signals as they realign themselves with the permanent magnet. This exact frequency (near 20MHz for H proton; less for the other nuclei) will induce a NMR signal of the same frequency from the sample, if the device is properly adjusted. Therefore, there are several calibrations that need to be carried out before any measurements of samples. The best vertical position of the sample holder in the rheo-NMR system is found by 3 preliminary tests. The proper value of attenuation of NMR device is determined to obtain a reasonable range of signal strength. The temperature reading devices are also calibrated before any measurement. Details can be found in Appendix A.

3.4.3.Sample Treatment for NMR Measurements

The L/M binary mixtures were used as samples. For the NMR measurements, the samples studied were 7L3M40 and 5L5M40. Each sample, of about 1.7mL, was placed into the sample tube which was located in the NMR device for measurement. The temperature of the samples was controlled by the temperature-control system which has been described in the XRD section. The samples were melted at 60°C for 10 minutes to destroy all the crystal memory which might cause crystallization to happen preferentially on a more stable form. The crystal residua in the melt change the structural preference of the crystal formation. The crystals grow much easier into the same structure as the crystal residua during crystallization. Therefore, it is crucial to make sure that all the crystal memory is destroyed during the heating so that the

possibility of having crystal residua in the system can be ruled out, and thus have no effect on the polymorphic structures of the crystals. From the temperature profile and the solid fraction data from NMR, it was clear that the solid fraction reduced to zero quickly after the temperature reached 60°C. (Detailed figures were presented in chapter 4, data analysis of the rheo-NMR measurements.) Another 10 minutes passed at that temperature before the samples were cooled down to different crystallization temperatures between 10 and 20°C at a cooling rate of 10°C /min. For sample 7L3M40, the crystallization temperatures were 12, 14, 16, and 18°C with shear rates of 800, 80, 8, or $0s^{-1}$. For sample 5L5M40, the crystallization temperatures were 11, 14, 17, and 19°C with shear rate at $8s^{-1}$. Each experiment was repeated 4 or 5 times to assess the variability between trials.

3.4.4.Rheo-NMR Data Collection

3.4.4.1.LabVIEW Program Collecting NMR Data

LabVIEW software was used to capture the signals received from the NMR device, process them and then record and save them as data sets. The program was developed by Dr. Mazzanti as a modification from the one developed by him and E. Mudge (Mazzanti, *et al.*, 2008).

For each data set, the solid signal portion (short time, about 108 μs) and the liquid signal portion (long time, about 100 ms), the original reading was cast into 250 measurement points included into the calculation. The liquid offset was obtained from the liquid signal portion, whereas the solid signal and liquid signal were obtained from the solid one described by the equation:

$$y = a \cdot e^{(-bt^2)} + c \tag{26}$$

where a is the solid signal, b is the exponential index, and c is the liquid signal. The three parameters a, b, and c were computed and saved from the LabVIEW program for further calibration.

The rheometer shaft of the Rheo-NMR system in this work was placed into the glass sample tube for both the static and shear experiments. The solid signal of the shaft had a

considerable effect on the solid signal reading from NMR since the part of the shaft in the sample tube is made of Lexan, which means the solid signal including the signal from the shaft and the sample itself. The solid background signal (SBC) was detected and calculated to get a linear function of temperature. For an attenuation value of 16,

$$SBC = -0.00362Tp + 1.07696 \quad (27)$$

Since the NMR signal is temperature dependent, this linear relation was obtained from the test of liquid sample with the Lexan shaft in it at different temperatures. It is likely that the solid signal of the sample was from the Lexan shaft because there was no solid in the sample and the glass sample tube was invisible to NMR.

Solid fraction (SF) is defined as the fraction of the solid signal and the total signal detected by the NMR device, described by the Eq. (25) as mentioned easier in section 3.4.1.2. Since the samples in this work contain 40% crystallizable materials and 60% solvent, the SF value at the final stage of the crystallization should be close to 40%.

3.4.4.2.RHEOPLUS software collecting rheological data

The rheological data were collected by the RheoPlus software which controls the measuring head. The parameters recorded in RheoPlus were the shear rates in unit s^{-1} and the electronic torque in unit of Nm. Further data analysis was carried out in Microsoft Office Excel.

CHAPTER 4 DATA ANALYSIS OF THE RHEO-NMR MEASUREMENTS

The original data sets of NMR signals and temperature profiles were saved as text files. Data was then imported to Microsoft office Excel software where further analysis was carried out. By recording the temperature profile and the NMR signal readings at the same time, the crystallization process was able to be observed simultaneously. Figure 4-1 shows an example of a single experiment, sample 7L3M40 at 12ºC under shear rate $80s^{-1}$.

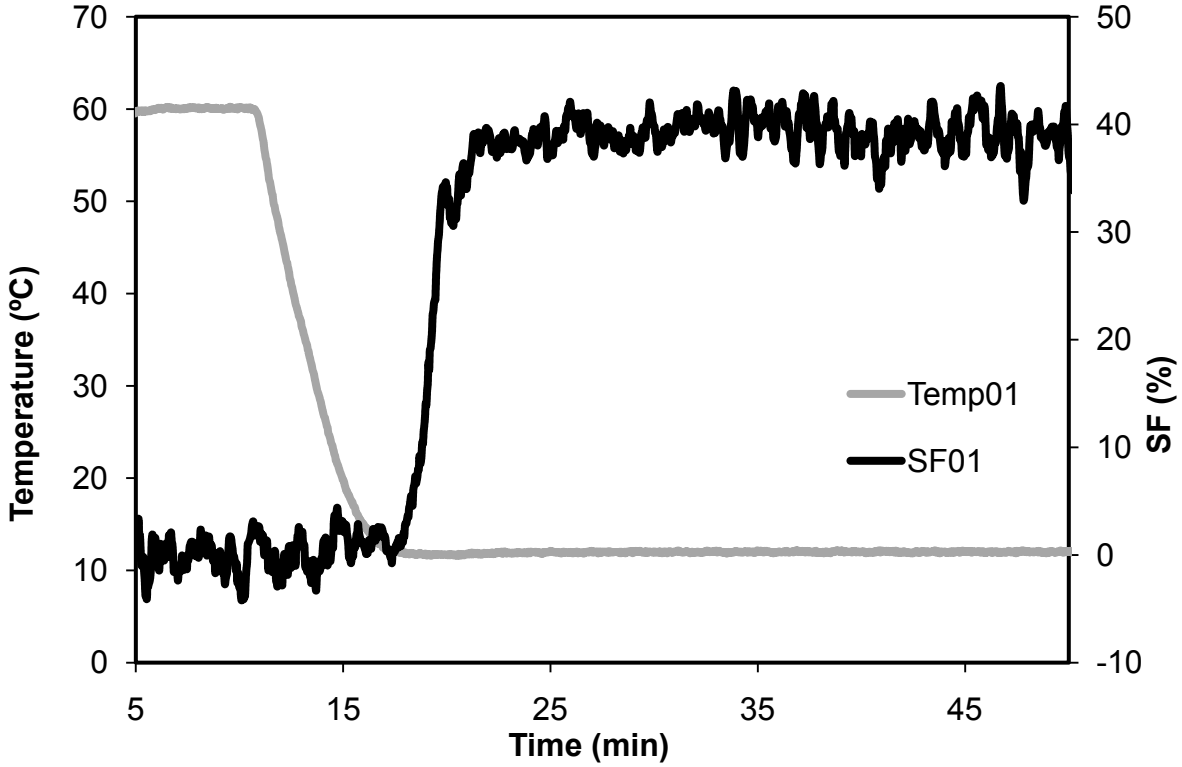

Figure 4-1 The temperature profile (Temp01) and SF value (SF01) as a function of time. The grey line is the temperature profile and the black line is the NMR signal readings.

The dramatic increase of the SF values from about the 18th minute after the experiment started showed the beginning of crystallization. The formation of crystals caused larger solid fraction readings. The binary mixture of triglycerides 7L3M40 started to crystallize less than 1 minute after the crystallization temperature was reached, in this case, 12ºC. The process lasted about 3 minute before all the crystallizable material crystallized out of the liquid solvent.

The small amount of sample produced a small intensity of the signal, which meant the signal to noise had been reduced compared to the normal operation of the NMR, as explained earlier in section 2.2.1.2. The data were smoothed by a moving average method. By getting the average of every five measuring point values (equivalent to 10 seconds), the errors between the five measuring points would have a chance to be cancelled or partially cancelled out because of their positive / negative deviation from the mean value by this method, which made the SF value curve looks “smoother”. The rheological data were analyzed using the same way of averaging.

4.1. Smoothing Average Method

Each experimental condition applied to 7L3M40 and 5L5M40 was performed more than 3 times for precision. For most of these parallel experiments, the results showed a good repetitiveness. The average values of these parallel experiments are then used to represent for all the experiments. Experiment of sample 40%7L3M under shear rate $80s^{-1}$ at crystallization temperature 12°C was used as an example to show how the smoothing average method works (Figure 4-2). This same experimental condition, which the test sample 40%7L3M was kept at 60°C for 10 minutes and then cooled down to 12°C at 10°C/min and kept at that temperature for 30 minutes, were repeated 5 times. These 5 experiments were seen as parallel experiments and named by number 01, 02, etc. For example, the temperature profile for the experiment 03 was shown as “Temp03” in the figures.

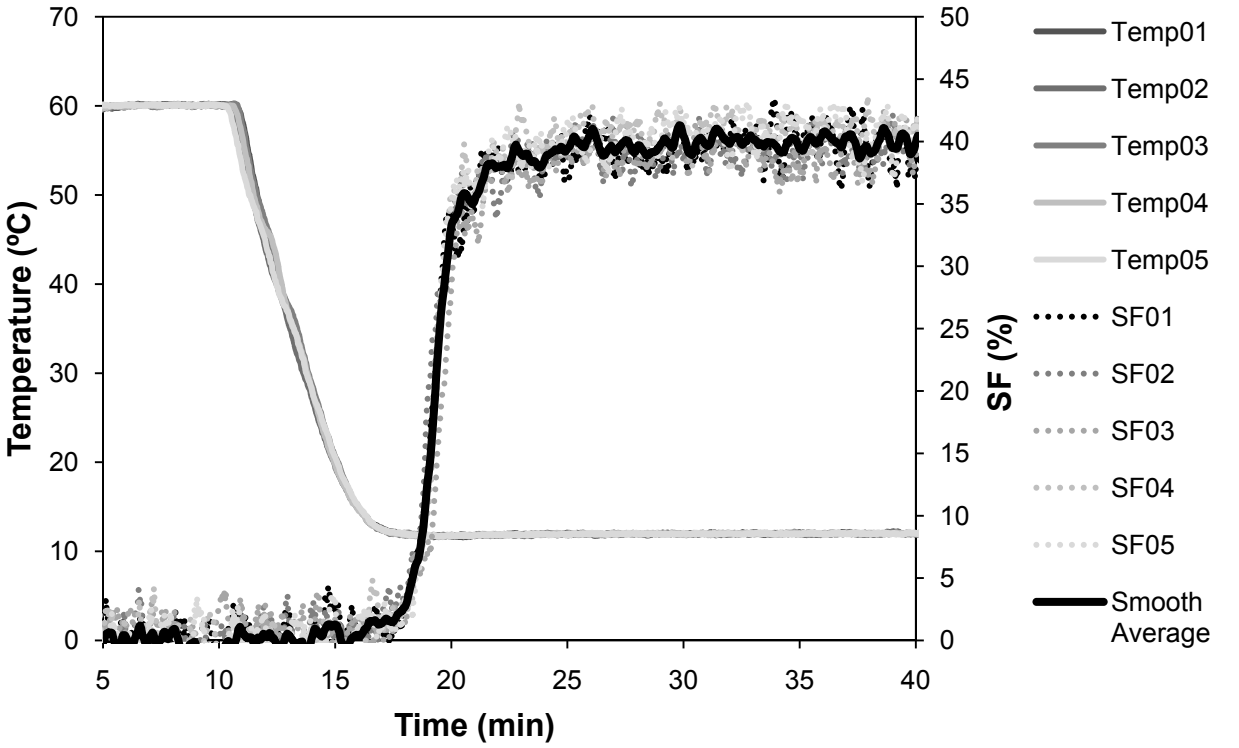

Figure 4-2 The temperature profiles and SF values as a function of time of the sample 7L3M40 at shear rate $80s^{-1}$, crystallization temperature 12ºC. Results of 5 parallel experiments were plotted from 01 to 05, with the black bold line as the smooth average result of SF values. The temperature profiles are shown as "Temp" curves in the figure, and the SF values are shown as "SF" curves.

In this figure above, the NMR signals are plotted with the temperature profiles. The smooth average (black bold curve) reduces the noise of signals from each experiment efficiently while illustrating the general trend of the signals.

For the data from the rheometer (Figure 4-3), especially for the data after the peak, the smoothing average method becomes less reliable because of the complicated crystallizing behaviours of the sample itself, especially its interaction with the walls of the Couette cell.

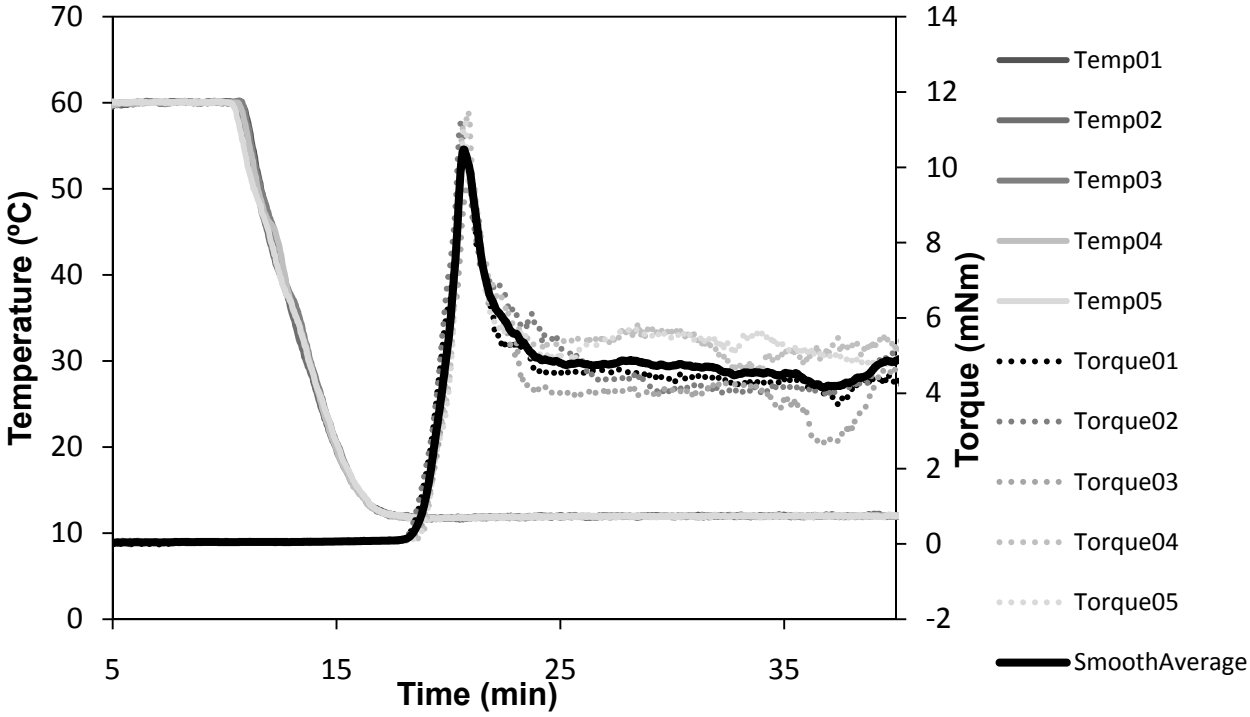

Figure 4-3 The temperature profiles and measured torque as a function of time of the sample 7L3M40 at shear rate 80s^{-1}, crystallization temperature 12ºC. Results of 5 parallel experiments were plotted from 01 to 05, with the black bold line as the smooth average result of measured torque. The temperature profiles are shown as "Temp" curves in the figure, and the torque values are shown as "Torque" curves.

However, that part of data is less interesting because the kinetic behaviour during the initial crystallization stages is the major interest in this study. There is no question that the crystallization process causes a huge jump of the torque when it started as shown in the plot about 18 to 21 minutes in accordance with the increase of SF values measured by NMR. Theoretically, the values of the torque should reach to a plateau after this process, whereas in our experiments, the distinct increase of the torque was always followed by a decrease happened rapidly which actually created a peak representing the crystals formed. Similar behaviour has been reported in the literature for other triglyceride systems (DeGraef*, et al.*, 2008, 2009). There are two potential explanations for the behaviour of the binary system. Once the crystal network is formed, the shear that continues to be applied to the system may break the crystal network structure apart very quickly instead of keeping the structure firm and well-packed. The other possibility is that the force provided by the shear might "squeeze" the fat crystal to the wall of

the sample tube, which causes the shaft spinning with touching only a small amount of the crystal structures. Either possibility can cause what has been observed in the shown figure. It is also likely that both of them happen causing the crystal network behaviour after the peak rather unpredictable. Hence, the reliability of the smoothing average method was reduced by the data, which is the unpredictable behaviour of the crystal network, not the defect of the method itself.

The standard errors of the datasets are presented in Figure 4-4. The relatively small values of the standard errors imply that the smooth average method is suitable to use to give a good description of the actual values of datasets.

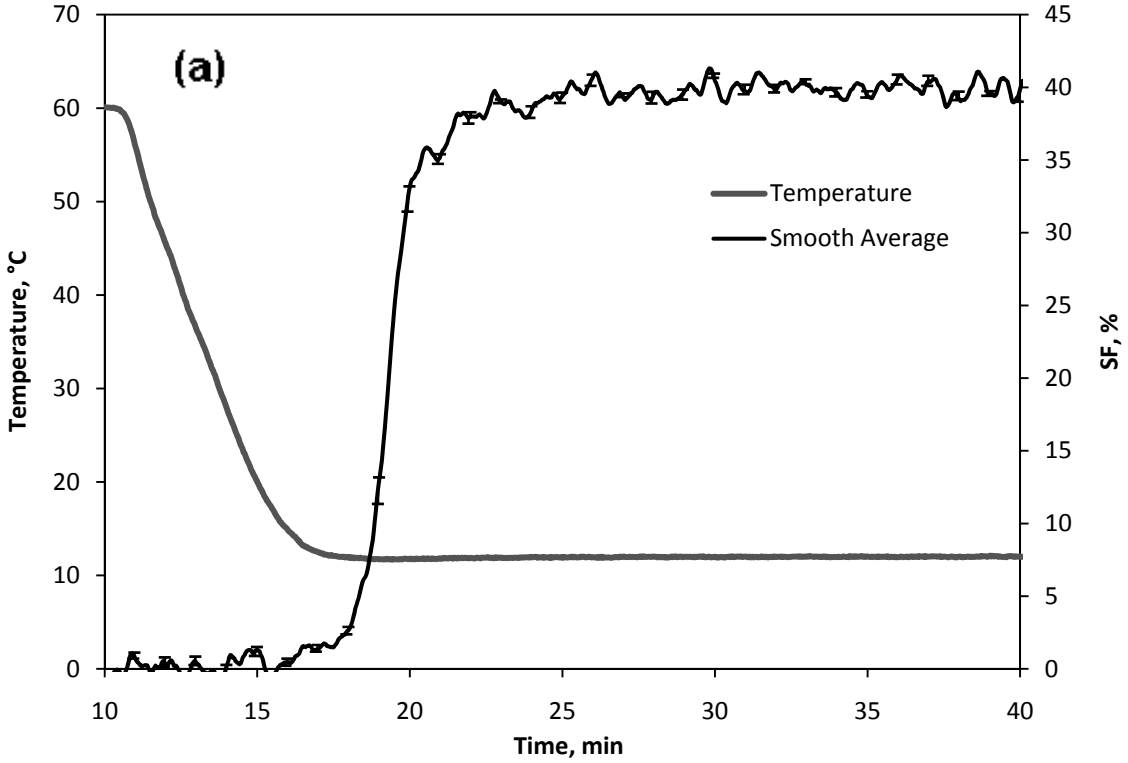

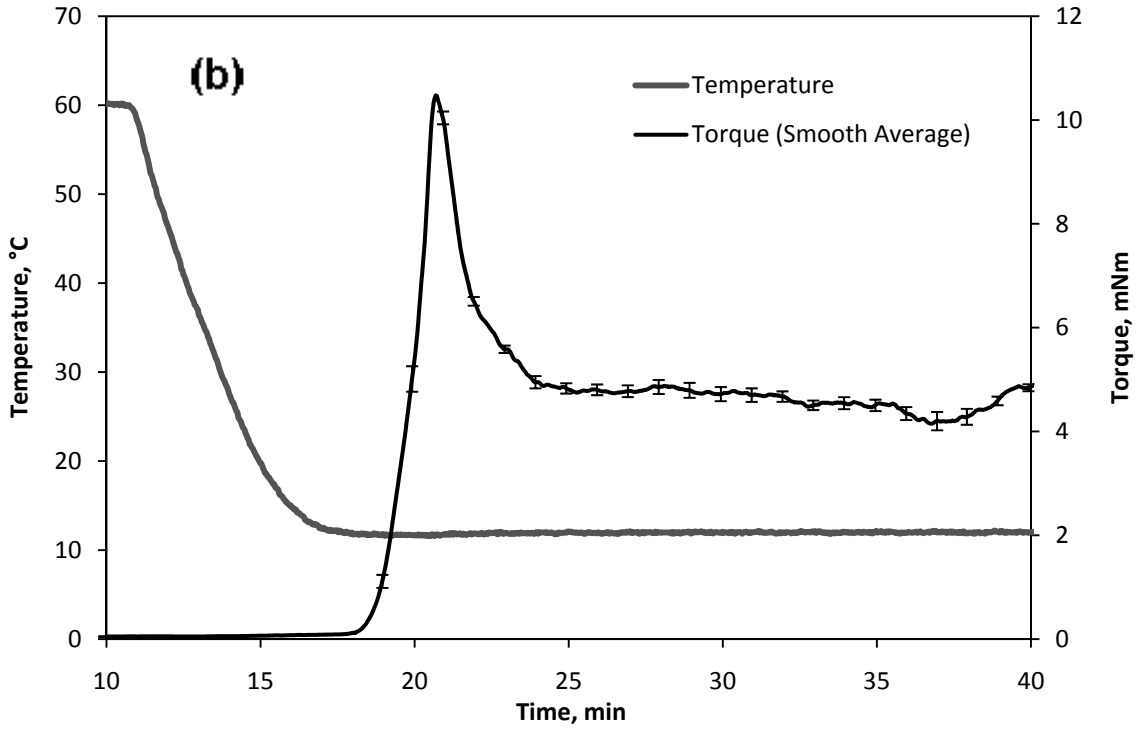

Figure 4-4 The temperature profiles and **(a)** SF values, **(b)** torque, as a function of time of the sample 7L3M40 at shear rate $80s^{-1}$, crystallization temperature 12ºC.

4.2.Apparent Viscosity Calculation

Apparent viscosity was chosen to be presented instead of measured torque because the apparent viscosity provides information about the internal properties of the sample that studied in this work.

$$\mu_{app} = \frac{\sigma}{\dot{\gamma}} = \frac{K_\sigma \cdot \tau}{\dot{\gamma}} \tag{28}$$

where μ_{app} is the apparent viscosity of the sample, σ is the shear stress, $\dot{\gamma}$ is the shear rate, K_σ is the calculated correction factor based on the configuration of the experimental system which was 440.69 Pa/mNm (see Appendix C for calculation detail), and τ was the torque value in mNm. μ_{app} was obtained by the equation for every experiment at constant shear rates.

CHAPTER 5 RESULTS AND DISCUSSION OF THE RHEO-NMR DATA

5.1.Modeling Crystal Growth

Crystal growth results from this work fit Avrami model, whose theory has already been explicated in section 2.1.2.4. Figure 5-1 shows an example of this model. The light grey line is the temperature profile; the dark grey line is the original NMR readings with the black line as the modified data by Avrami model. The model helps to obtain a fair representation of the data without the noise.

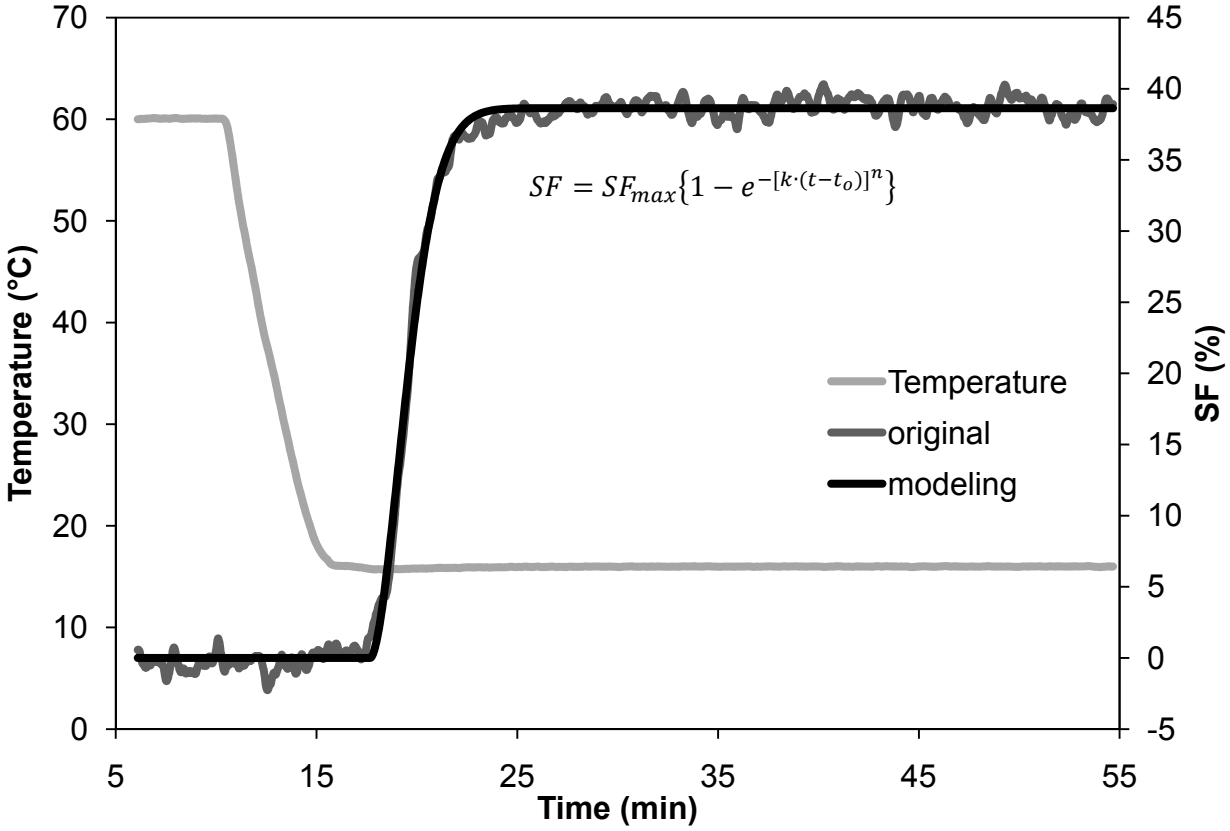

Figure 5-1 The temperature profiles and measured and modified NMR signal as a function of time of the sample 7L3M40. The shear rate was $80s^{-1}$ and the crystallization temperature was 12ºC. The light grey line is the temperature profile; the dark grey line is the original NMR readings with the black line as the modified data by Avrami model.

The sample 5L5M40 was tested only at one shear rate $8s^{-1}$ at four different crystallization temperatures, 11, 14, 17 and 19ºC. The results of the Avrami modeling for these four experiments are shown in Figure 5-2 **(a-d)**.

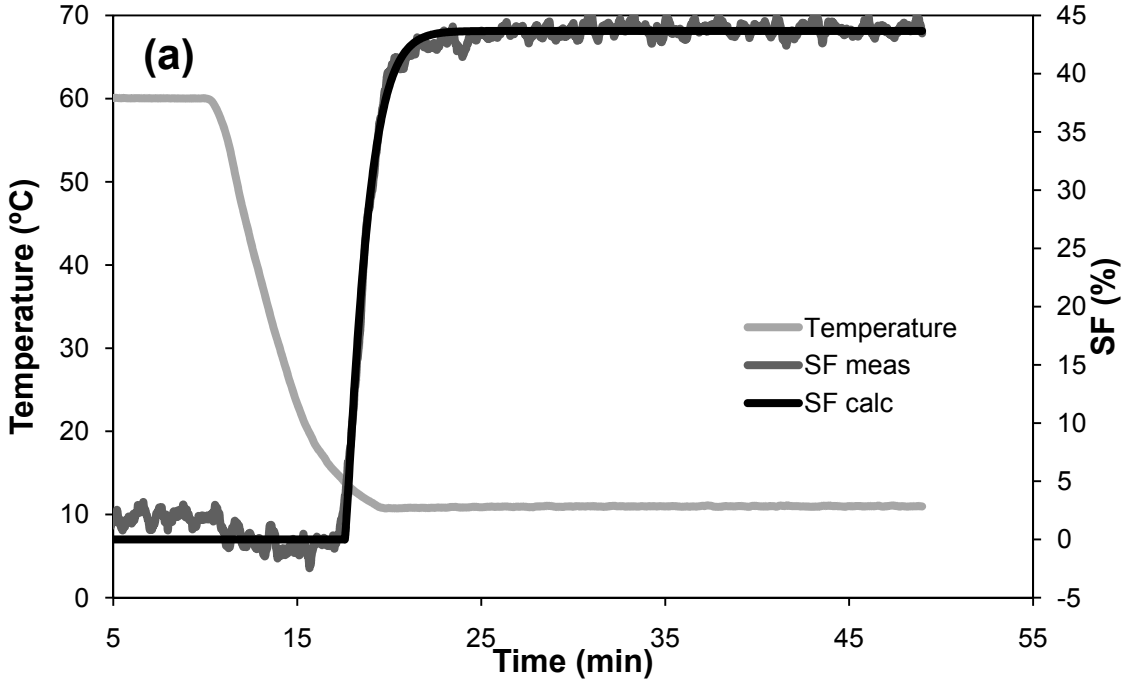

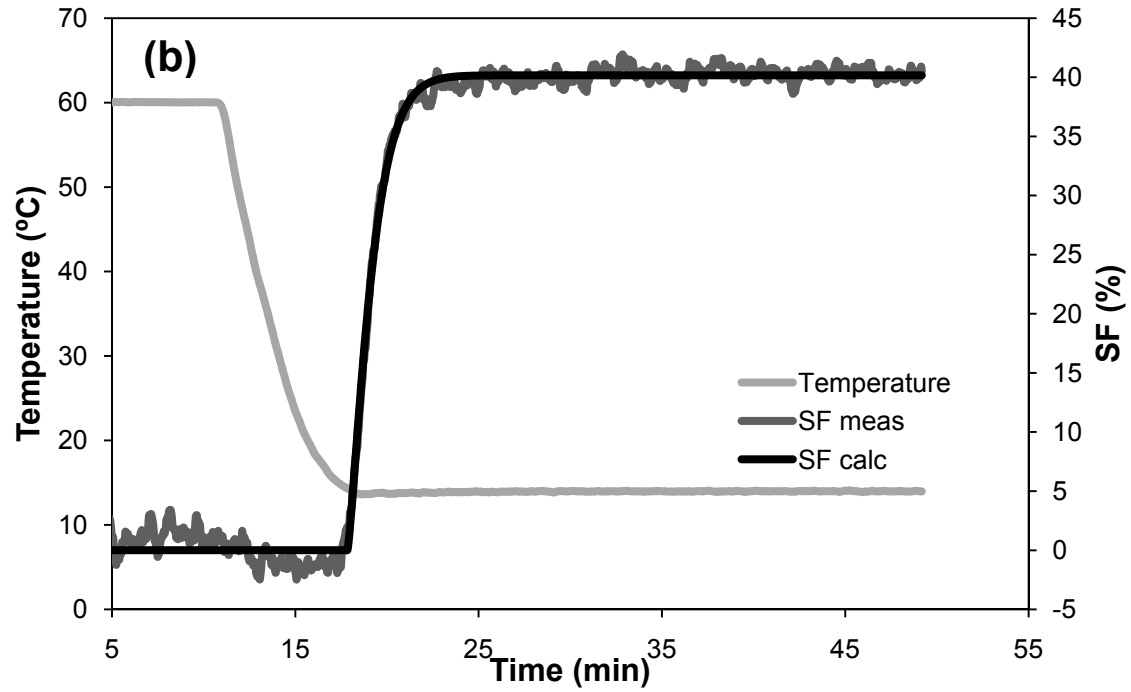

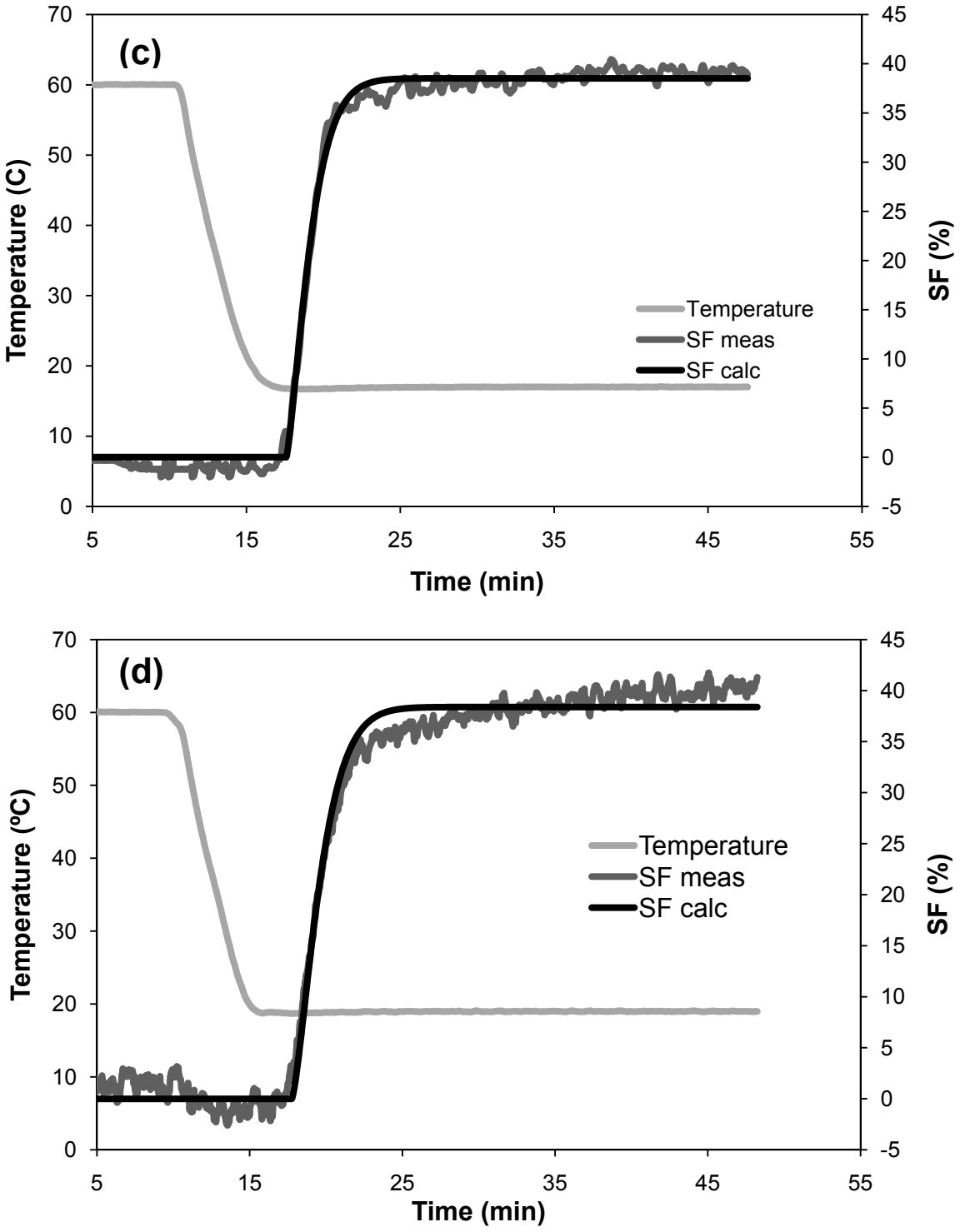

Figure 5-2 The temperature profiles and measured and modified NMR signal as a function of time of the sample 5L5M40. The shear rate was $8s^{-1}$ and the crystallization temperatures were 11ºC (**a**), 14ºC (**b**), 17ºC (**c**), and 19ºC (**d**). The light grey line is the temperature profile; the dark grey line is the original NMR readings, which is called "SF meas", and the black line is the calculated data "SF calc" using Avrami equation.

Avrami Model is found consistent with the crystal growth of 5L5M40 at 11ºC (Figure 5-2 **(a)**) and 14ºC (Figure 5-2 **(b)**) under shear $8s^{-1}$. However, for the two experiments of higher crystallization temperatures, 17ºC (Figure 5-2 **(c)**) and 19ºC (Figure 5-2 **(d)**), the Avrami Model did not satisfactorily describe the second regime. As the system got closer to equilibrium, the growth regime becomes controlled by diffusion, manifested by the kinetics following a square root of time dependence, as reported by Mazzanti *et al.* (2008). Hence, the crystal growth process was separated into two regimes. The first regime was described by the Avrami Model whereas the second one was described by the square root of time dependence. Take the experiment of sample 5L5M40 at 19ºC under shear $8s^{-1}$ as an example. Figure 5-3 **(a)** shows the first regime of the whole crystallization process with Avrami model fitting, while **(b)** shows the square root of time model of the second regime where the diffusion takes control.

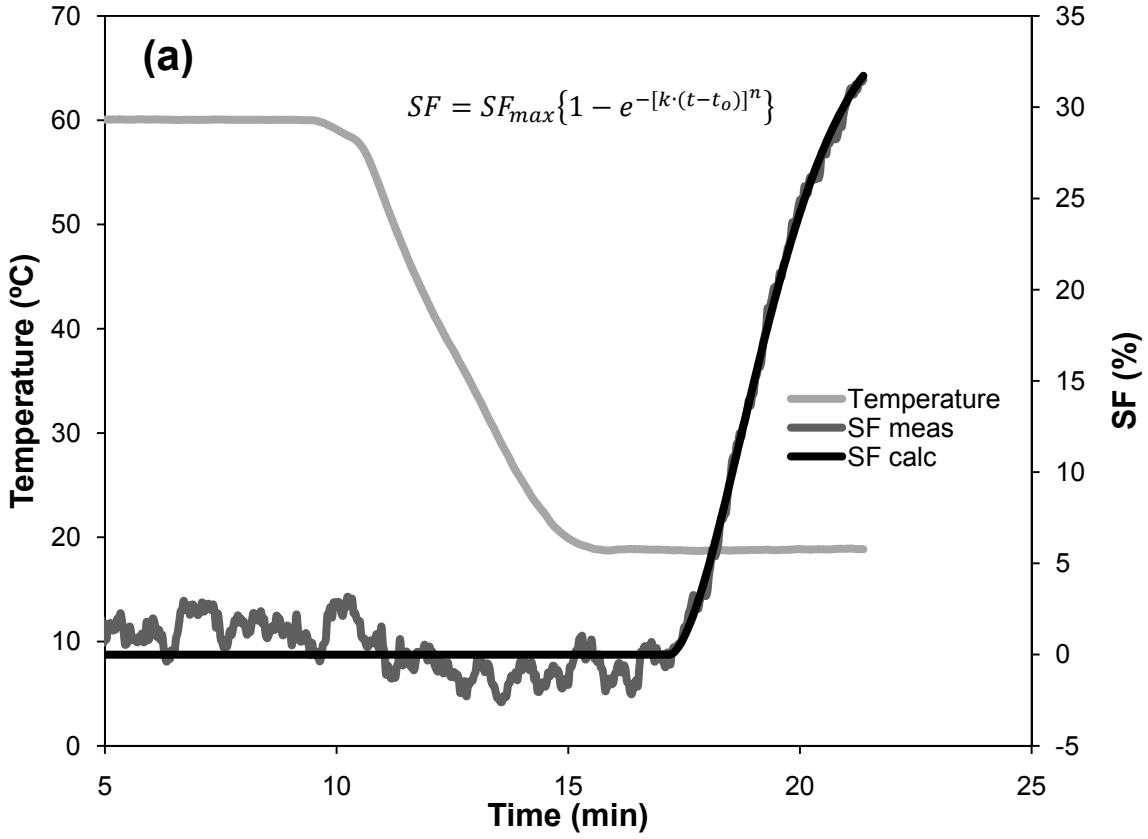

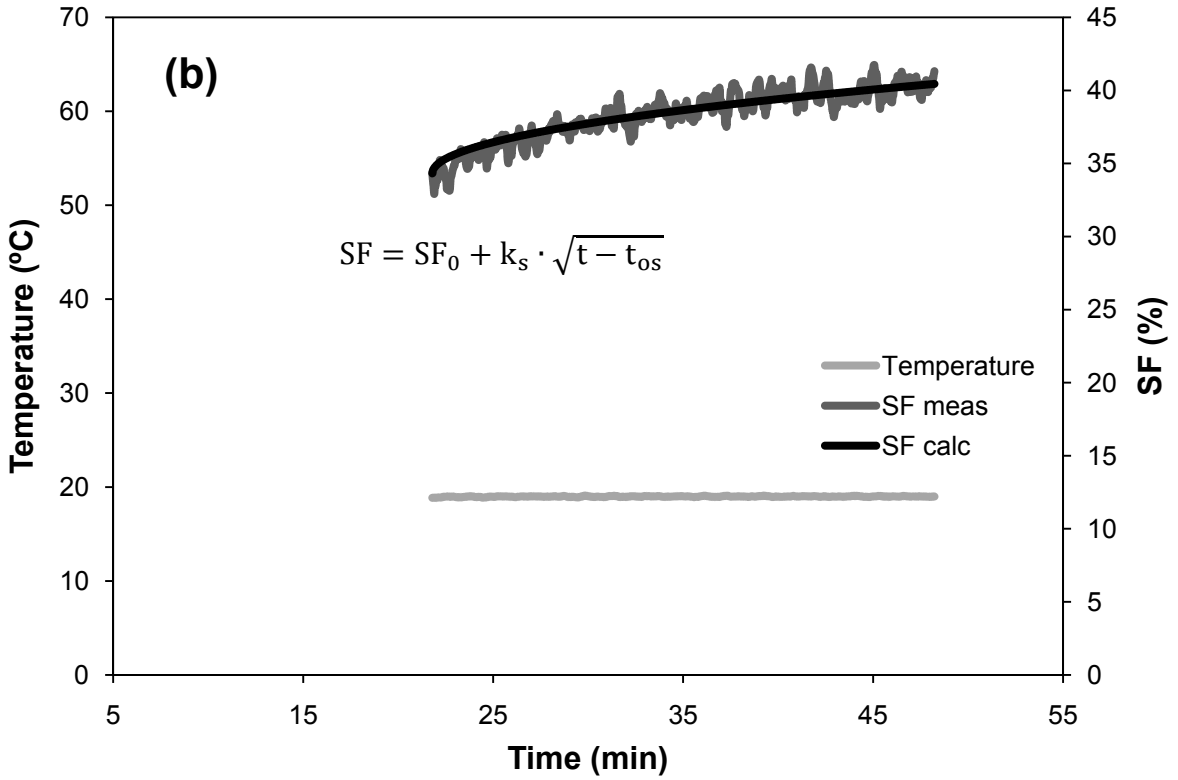

Figure 5-3 The temperature profiles and measured and modified NMR signal as a function of time of the sample 5L5M40. The shear rate was $8s^{-1}$ and the crystallization temperature was 19ºC. The light grey line is the temperature profile; the dark grey line is the original NMR readings, which is called "SF meas", and the black line is the calculated data "SF calc" using equations. **(a)** is the first regime of crystal growth fitted by Avrami equation and **(b)** is the second regime fitted by the square root of time model.

By plotting the two regimes together as a function of time, a good description of crystallization kinetics behaviour was found by combining two different models together. The results have been shown in Figure 5-4.

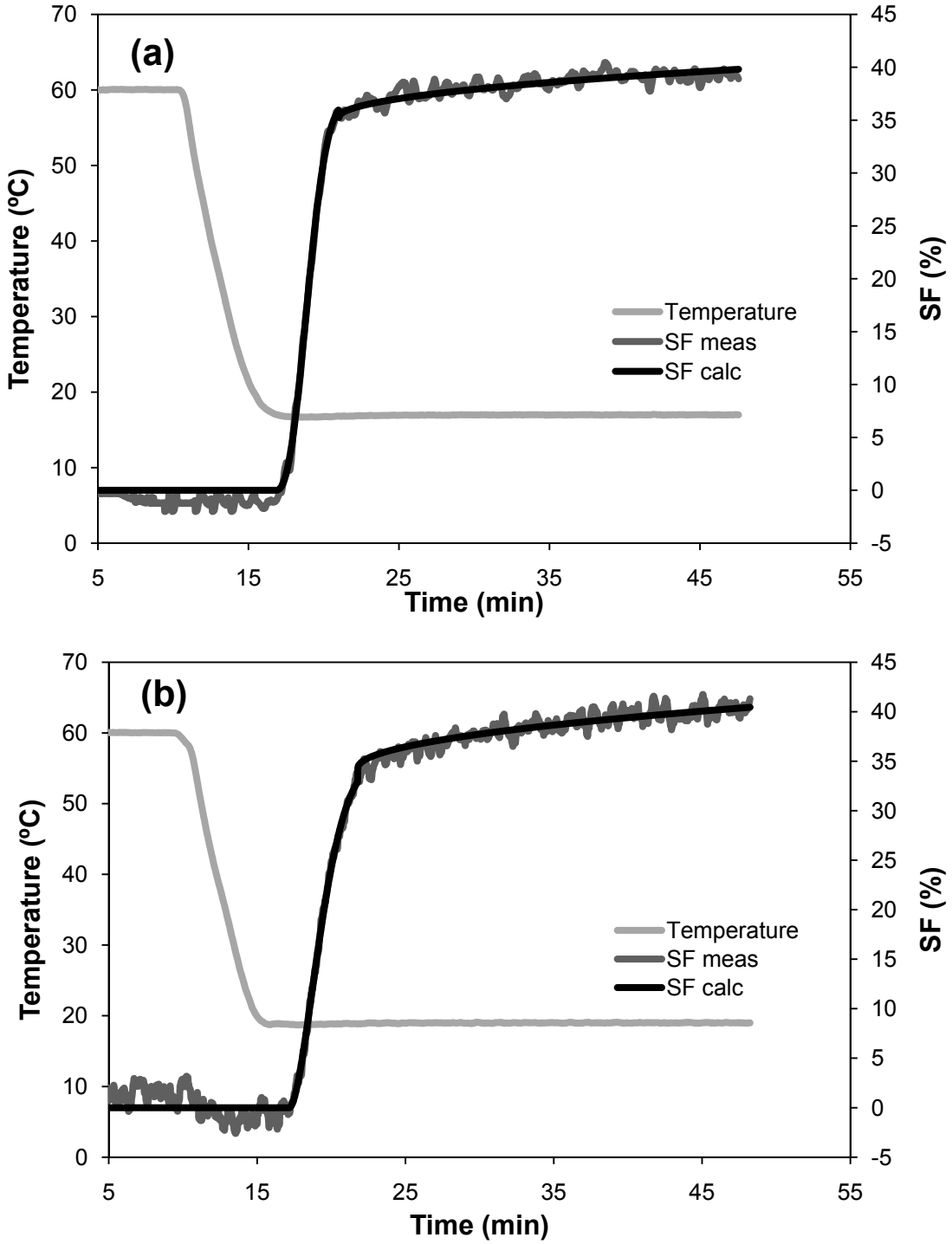

Figure 5-4 The temperature profiles and measured and modified NMR signal as a function of time of the sample 5L5M40. The shear rate was $8s^{-1}$ and the crystallization temperatures were 17ºC (**a**) and 19ºC (**b**). The light grey line is the temperature profile; the dark grey line is the original NMR readings, which is called "SF meas", and the black line is the calculated data "SF calc" using the combination of two models.

Compare Figure 5-4 **(a)**, **(b)** to Figure 5-2 **(c)**, **(d)**, the combination models performed a better description than Avrami model along in the experiments done at 17 and 19ºC under shear $8s^{-1}$. The final stage of crystallization which dominated by diffusion is observed as a linear relation as a function of the square root of time in those two experiments. Similar results have been found in experiments performed at 14 and 16ºC at shear rate $8s^{-1}$ for the other sample 7L3M40 (Figure 5-5, **(a)** and **(b)**).

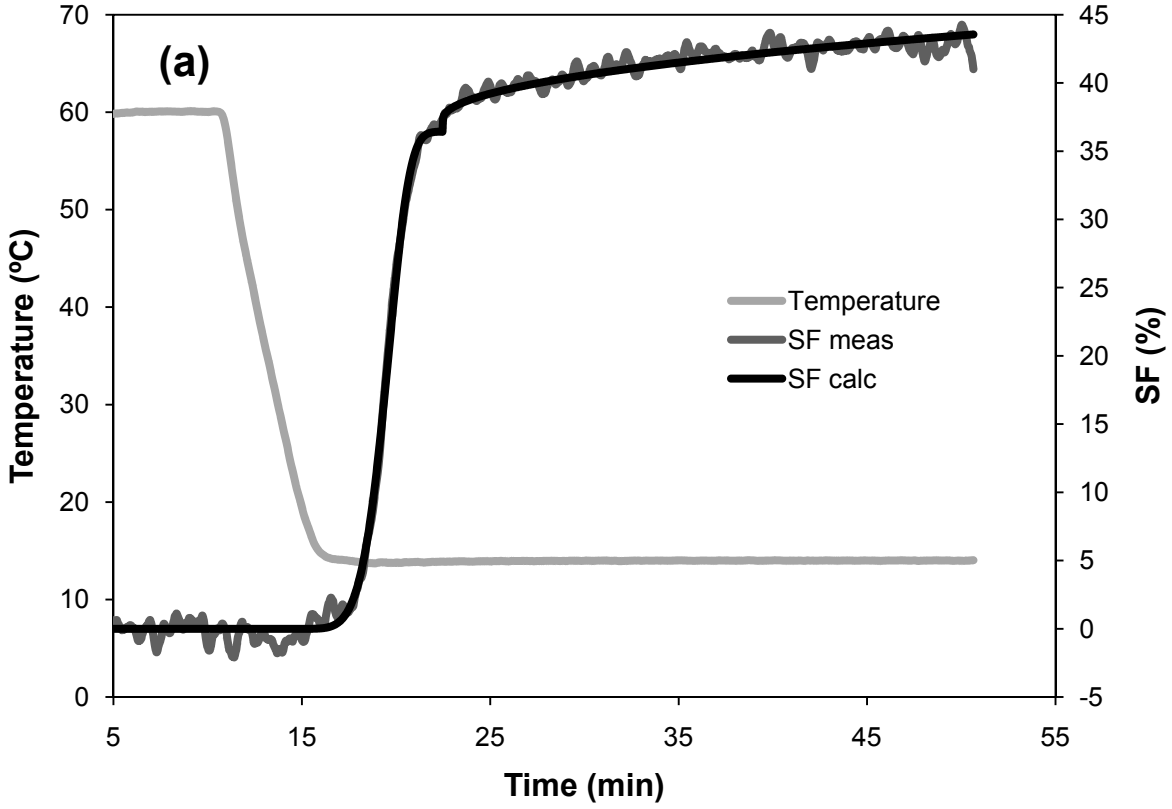

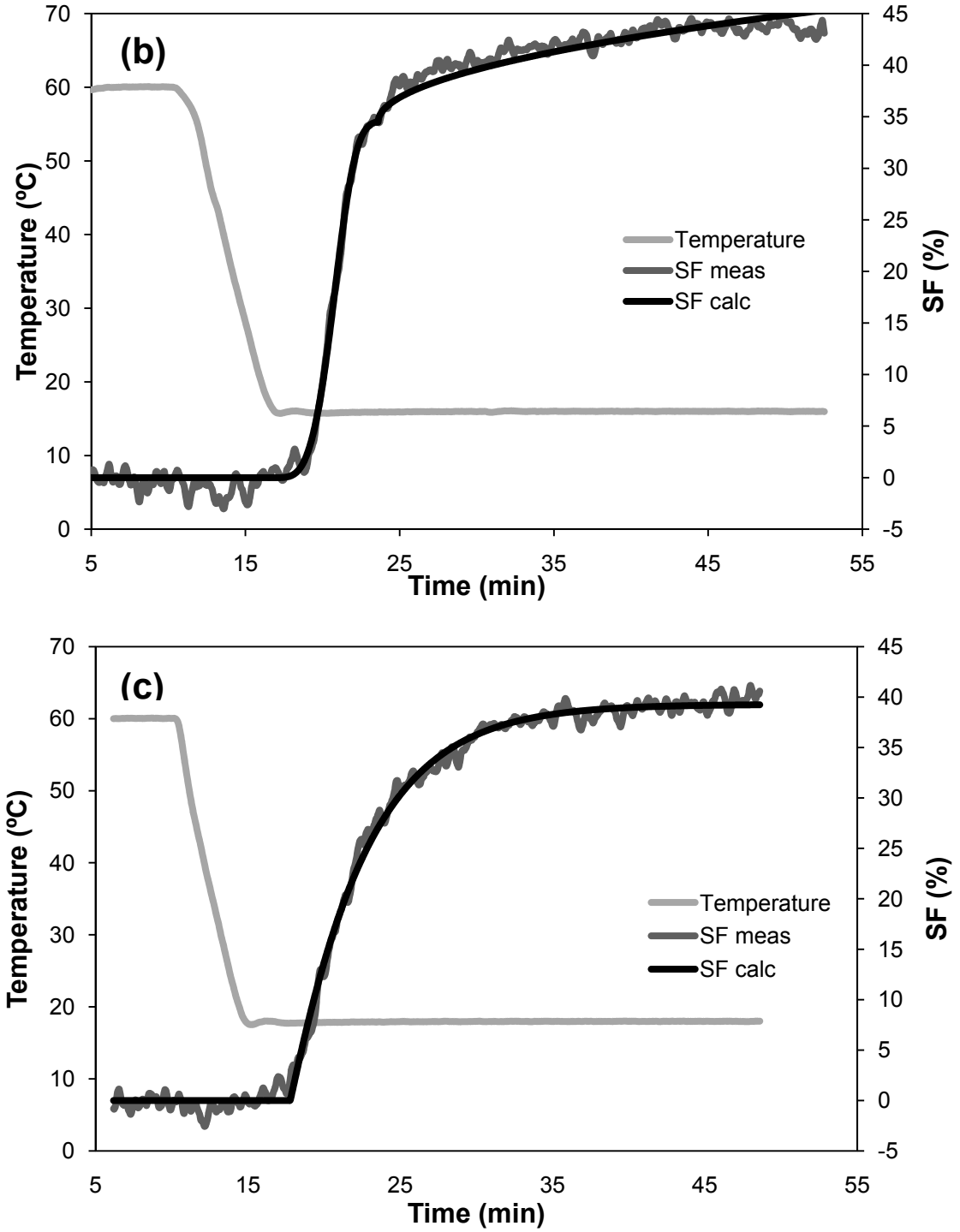

Figure 5-5 The temperature profiles and measured and modified NMR signal as a function of time of the sample 7L3M40. The shear rate was $8s^{-1}$ and the crystallization temperatures were 14ºC **(a)**, 16ºC **(b)**, and 18ºC **(c)**. The light grey line is the temperature profile; the dark grey line is the original NMR readings, which is called "SF meas", and the black line is the calculated data "SF calc" using model equation. In **(a)** and **(b)**, the data were fitted by the combination of Avrami model and square root of time equation, whereas Avrami model was the only model used in the data in **(c)** plot.

Diffusion controlled reactions are the ones that occur so quickly that the rate of reaction is the rate of transport of the reactants through the medium, which normally happen at the final stage of fat crystallization, since most of the crystallizable material is already out of the solution. However, it did only happen at certain conditions in this work, where crystallization temperatures and shear rates were both involved. The crystallization temperatures that showed diffusion controlled growth dominated were 17 and 19ºC for sample 5L5M40 while 14 and 16ºC for sample 7L3M40. Furthermore, this type of growth was only found under shear $8s^{-1}$ which was a low shear rate compared to the other two shear rates been used in the research, 80 and $800s^{-1}$.

5.2.Effect of Shear and Crystallization Temperature on k, n Values

5.2.1.Effect of Crystallization Temperature on k, n Values

The temperature dependence of the growth rate constant k and the Avrami exponent n for sample 5L5M40, presented in Table 5-1 and Figure 5-6, shows linear relations. However, the trend of growth constant k is different from that of the exponent n. The k values decreased as the crystallization temperature increased, meaning higher temperatures lower the crystal growth rates because a lower level of supercooling gives the fat sample less driving force to crystallize. Meanwhile, at higher temperatures, it can also be presumed that a smaller chance of crystals interacting with each other since they grew at a lower rate. Hence, the n values increased instead. Similar results have been found from the sample 7L3M40 at three different shear rates, 8, 80 and $800s^{-1}$, as presented in Table 5-2 and Figure 5-7.

Table 0-3 values of k and n determined from Avrami model for sample 5L5M40 at shear rate $8s^{-1}$.

sample	temperature (ºC)	k value (min^{-1})	n value
5L5M40	11	0.81 ± 0.01	1.20 ± 0.04
	14	0.68 ± 0.01	1.28 ± 0.02
	17	0.56 ± 0.02	1.34 ± 0.04
	19	0.47 ± 0.01	1.40 ± 0.01

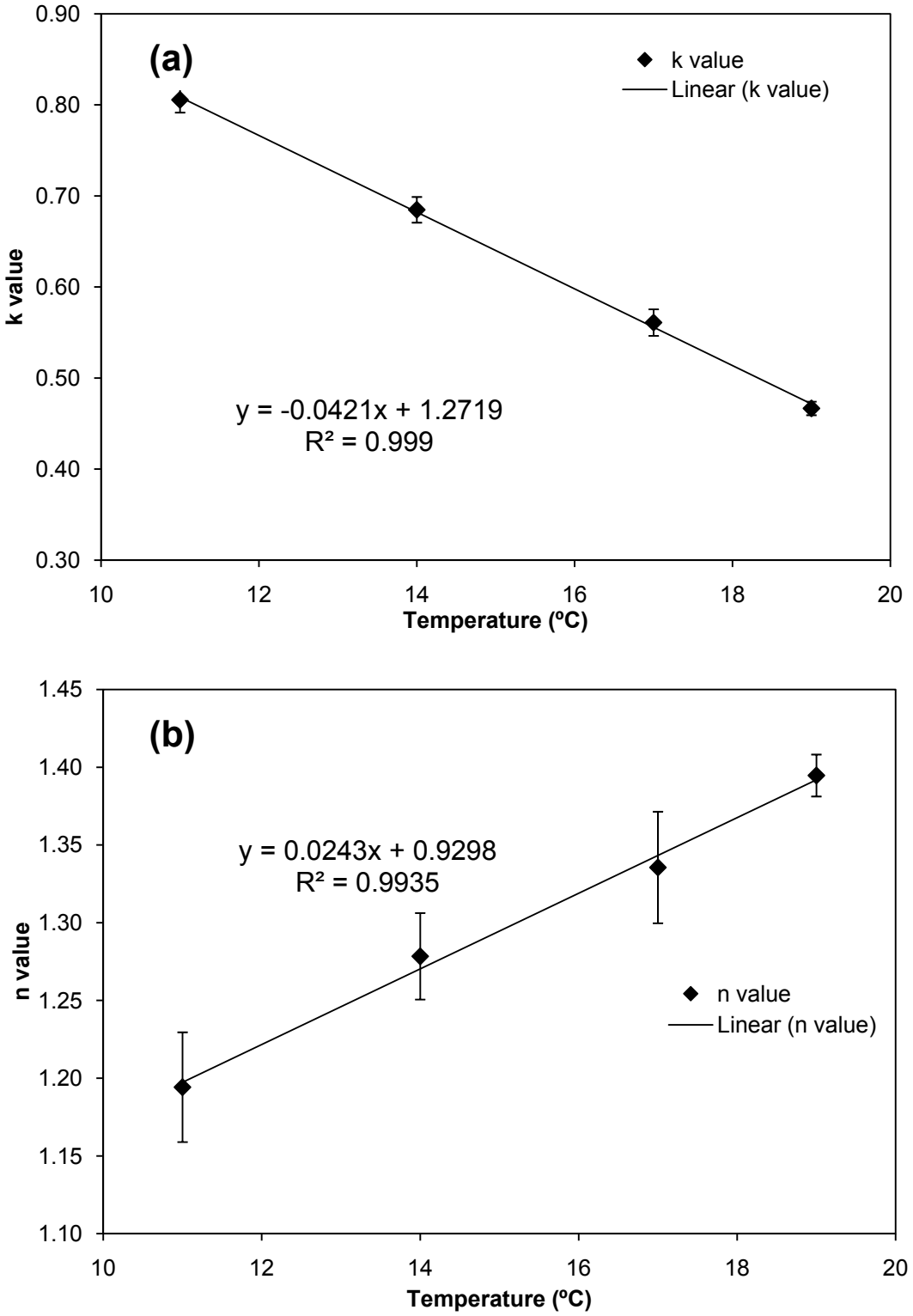

Figure 5-6 Values of ***k*** **(a)** and ***n*** **(b)** from Avrami model for sample 5L5M40 at shear rate $8s^{-1}$ as a function of temperature.

Table 0-4 values of k and n determined from Avrami model for sample 7L3M40 at shear rate 8, 80, and 800s^{-1}.

k value, (min^{-1})	8 s^{-1}	80 s^{-1}	800 s^{-1}
14ºC	0.55 ± 0.01	0.63 ± 0.02	0.75 ± 0.02
16ºC	0.38 ± 0.01	0.44 ± 0.01	0.72 ± 0.01
18ºC	0.20 ± 0.00	0.32 ± 0.01	0.63 ± 0.01

n value	8 s^{-1}	80 s^{-1}	800 s^{-1}
14ºC	0.93 ± 0.02	1.34 ± 0.03	0.58 ± 0.02
16ºC	1.01 ± 0.01	1.75 ± 0.04	0.58 ± 0.01
18ºC	1.05 ± 0.01	2.08 ± 0.06	0.58 ± 0.01

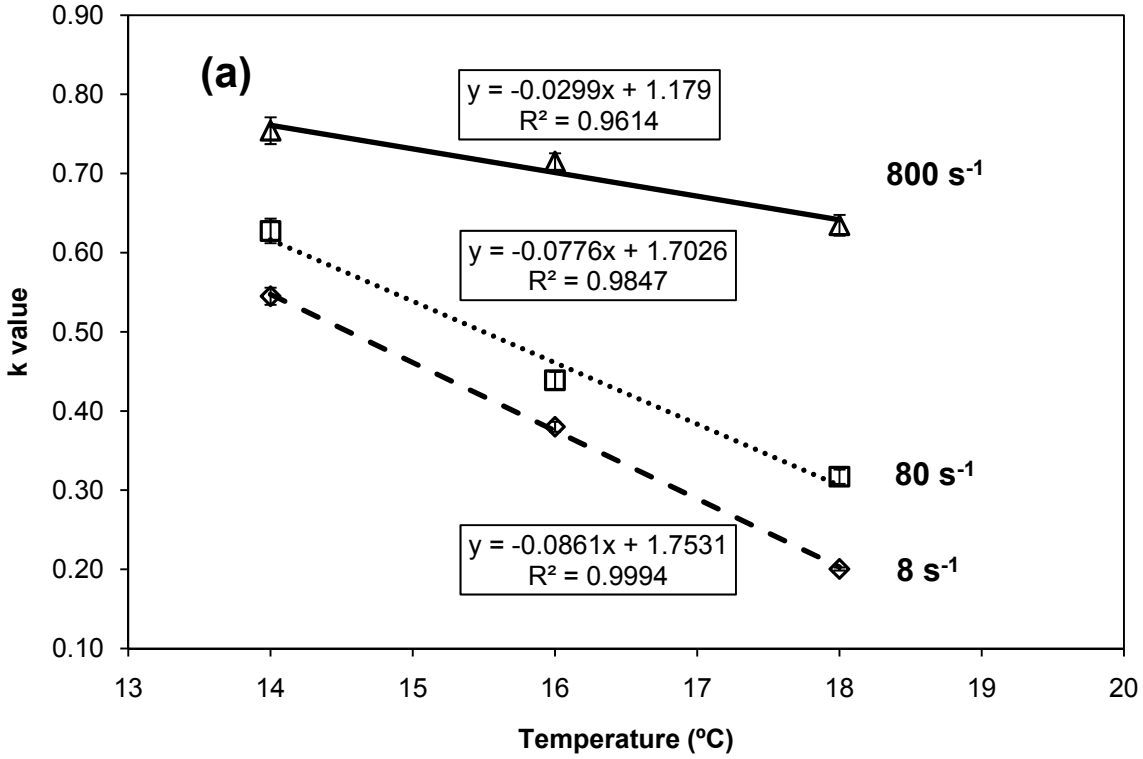

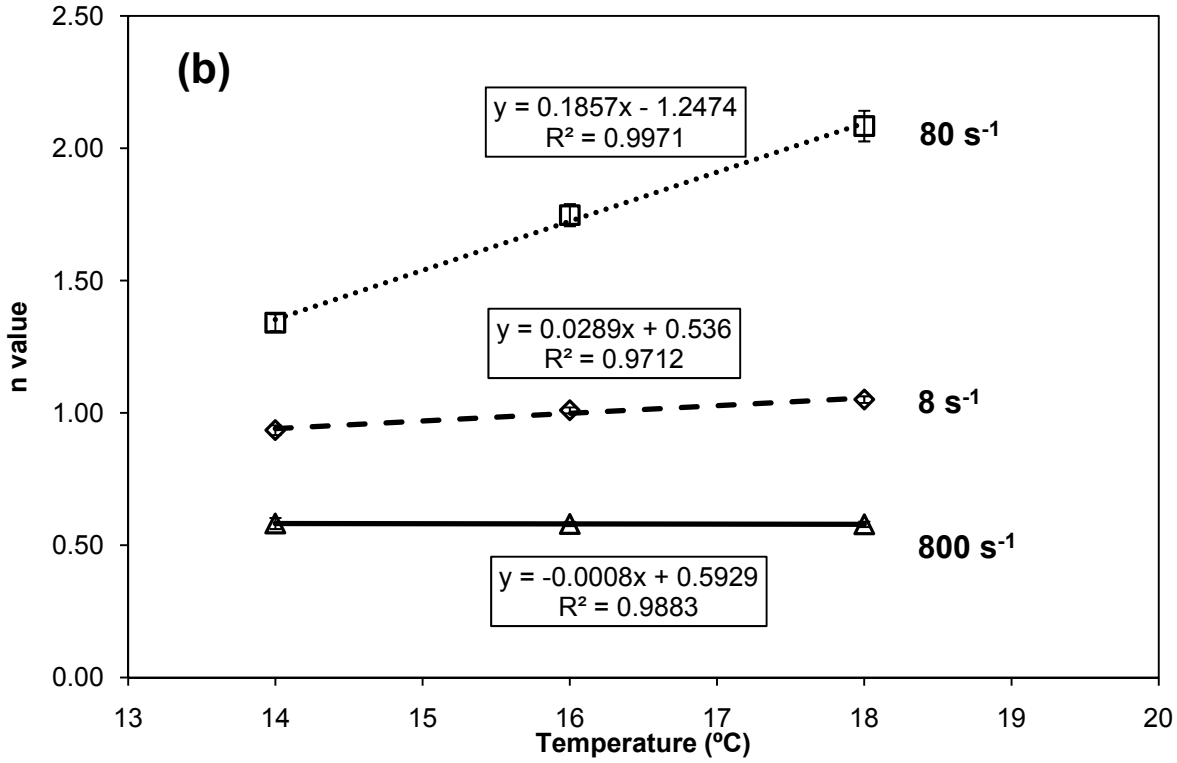

Figure 5-7 Values of $\boldsymbol{k}$ **(a)** and $\boldsymbol{n}$ **(b)** from Avrami model for sample 7L3M40 at shear rate 8, 80 and 800s^{-1} as a function of temperature.

The data from the experiments where diffusion controlled growth dominated the later times was analyzed and tabulated in Table 5-3.

Table 0-5 values of parameters for the experiments dominated by the diffusion controlled growth at shear rate 8s^{-1}.

Sample	Temperature °C	SF_{max}	k, min^{-1}	n	t_o, min	k_s, $min^{-0.5}$	t_s, min
5L5M40	17	37.0 ±0.5	0.56 ±0.02	1.34 ±0.04	16.8 ±0.2	0.9 ±0.1	21.0 ±0.0
	19	35.4 ±0.7	0.47 ±0.01	1.40 ±0.01	17.2 ±0.1	1.2 ±0.2	21.8 ±0.0
7L3M40	14	36.4 ±0.1	0.55 ±0.01	0.93 ±0.02	14.4 ±0.3	1.2 ±0.2	22.5 ±0.0
	16	34.6 ±0.2	0.38 ±0.01	1.01 ±0.01	16.8 ±0.3	2.0 ±0.1	23.6 ±0.0

This type of growth was only found at shear rate $8s^{-1}$ in this work. When the temperature arose, the SF_{max} values decreased, with initial crystal growth time t_o and diffusion regime initial time t_s delayed. The range of the k_s values obtained from our work is consistent with the one from milk fat sample as Mazzanti *et al.* reported (Mazzanti, *et al.*, 2008), which is from 0.14 to 0.54.

5.2.2.Effect of Shear on k, n Values

The shear effect on k, n values is more complicated than the crystallization temperature effect. The k and n values were presented as a function of shear rate in a logarithmic plot, seen in Figure 5-8. Immediately apparent from the Figure 5-8 **(a)** is that the k values increase when shear rates increase, with the values getting close to each other. It should be noted that the differences between k values of different crystallization temperatures at one constant shear rate become smaller when higher shear rate applied. Shear becomes dominatant to determine the k values than temperature, which means shear stimulates the crystallization more than the level of supercooling. The n values shown in Figure 5-8 **(b)** estimate the numbers of free dimensions crystals grow during crystallization. The shear rate change from 8 to $80s^{-1}$ gives the crystals more free dimensions to grow, whereas the highest shear rate in this work, $800s^{-1}$, definitely limits the dimensions for growth. One possible explanation is that there are much more crystal nuclei appeared at the high shear rate, producing more crystals during the crystallization but smaller sized ones. These small crystals with short distances from each other are able to interfere easier than bigger but distanced crystals in the other cases. Hence, the value of free dimensions n, has been reduced by the high shear. Noteworthy information is also that the n values from experiments at shear rate $800s^{-1}$ reached very similar values (around 0.58) even at different temperatures, which proves again that high shear rates dominate the kinetic behaviour of fat crystallization, rather than temperature.

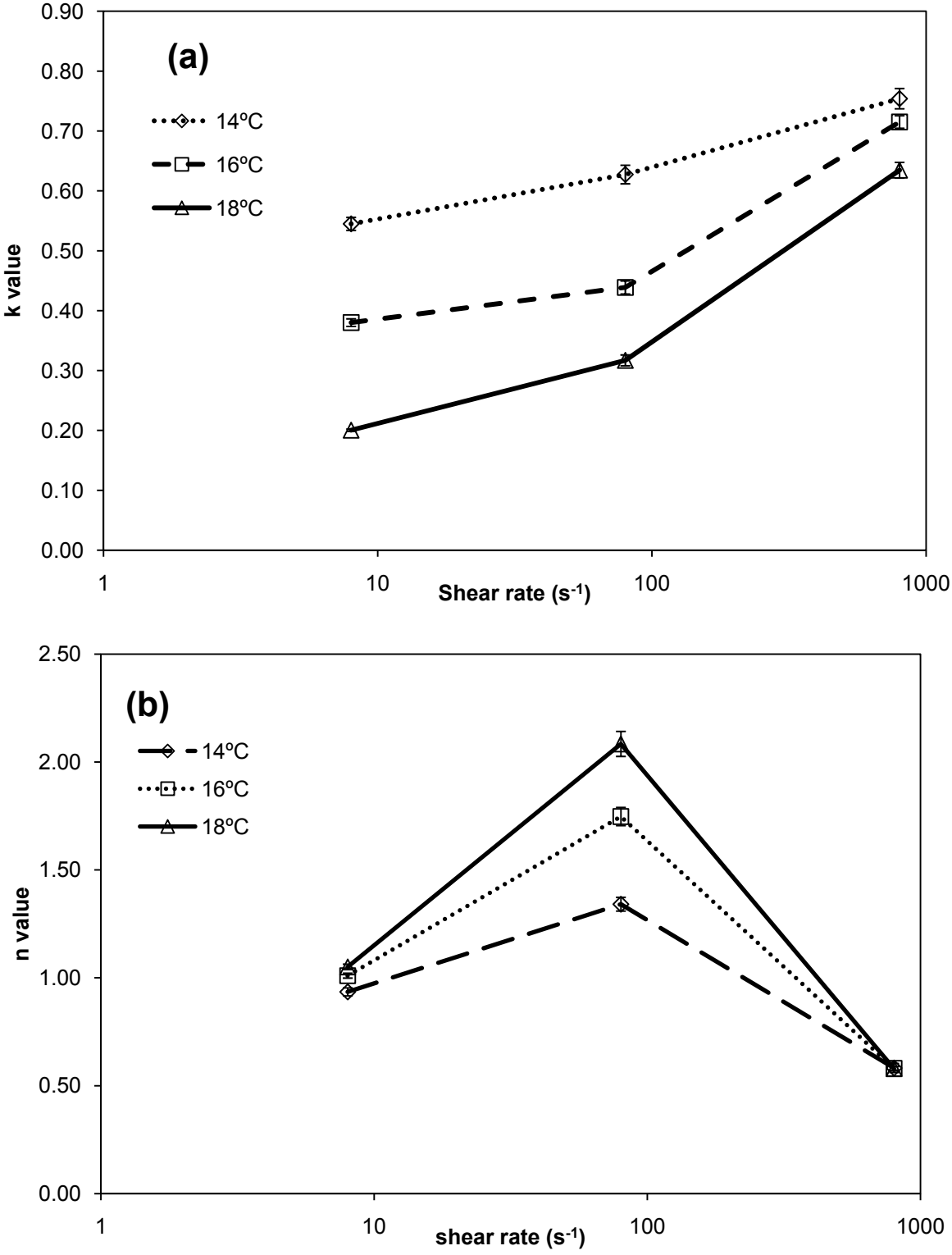

Figure 5-8 Values of ***k*** **(a)** and ***n*** **(b)** from Avrami model for sample 7L3M40 at shear rate 8, 80 and 800s^{-1} as a function of time.

5.3.Effect of Shear on the SF_{max} Values

Another parameter obtained from the Avrami Model was maximum solid fraction, SF_{max}. The crystallization temperature for sure affects the SF_{max} values that can be reached in the experiments, as seen in Figure 5-9. SF_{max} values have an inverse relation with temperatures.

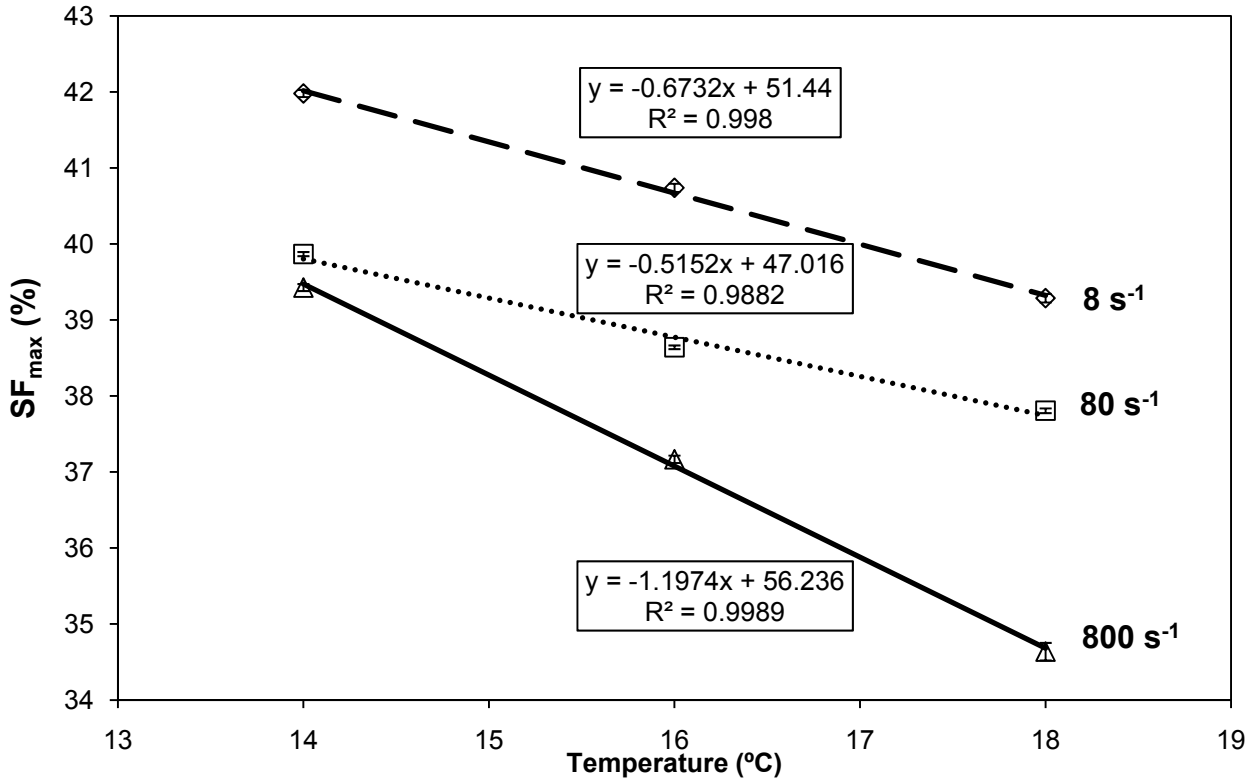

Figure 5-9 SF_{max} values for sample 7L3M40 at shear rate 8, 80 and 800s^{-1} as a function of temperature. The error bar associated with each measurement is smaller than the graphic marker.

Shear also reduces the SF_{max} values (Figure 5-10), which may imply that shear hinders crystal growth after nucleation into large particles, even though it accelerates the crystallization process and generates more crystal nuclei. There is another possibility conducing to the results. The huge amount of heat generated by the high shear might warm up the sample causing less fat crystallized.

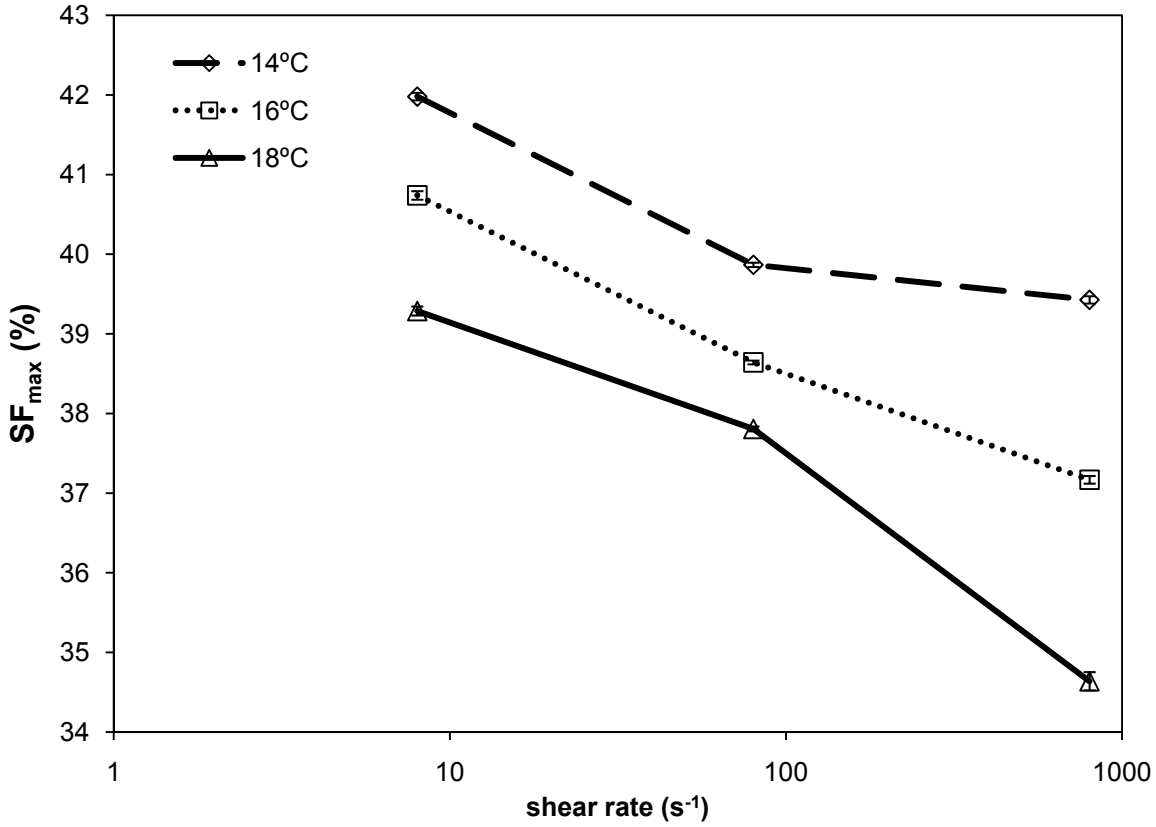

Figure 5-10 SF_{max} values for sample 7L3M40 at crystallization temperature 14, 16 and 18°C as a function of shear rate. The error bar associated with each measurement is smaller than the graphic marker.

CHAPTER 6 RESULTS AND DISCUSSIONS OF THE XRD DATA

The diffraction pattern images from the XRD measurements require several steps of data processing before the information can be abstracted from them. These steps include filtering and unwarping the images, transferring them into data set arrays by creating the radial and azimuth plots, and then fitting the diffraction peaks. The fitting process provides parameters such as d-spacing values, the area of the diffraction peak, and the full width at half maximum of the peak. The details of these steps, as well as instructions for the software involved into the XRD measurements analysis, can be found in Appendix B.

6.1.Wide Angle X-ray Diffraction Measurements

The Wide Angle X-ray Diffraction (WAXD) measurements identify polymorphic forms by numbers of diffraction peaks and their positions in q. In this work, however, the information revealed from the diffraction peaks of the WAXD measurements was limited since the background of the solvent (Triolein) and the background of Lexan created a bump hiding most of the diffraction peak information underneath. It became difficult to identify the polymorphic form using the data gathered from the diluted binary mixture. Fortunately, dry binary mixture sample powder had been tested in a capillary system before by another researcher in our group, making it possible find the diffraction pattern for each polymorphic form from those data. By comparing them with the WAXD measurement results from the dilute binary system, it was estimated that there were two polymorphic forms present in both samples 7L3M40 and 7L3M60, the β′ and β forms (Figure 6-1). The WAXD measurements for diluted Trimyristin sample, MMM40 were also compared to the pure Trimyristin sample powder. Two polymorphic forms β′ and β were present (Figure 6-2). The polymorphic form appeared at the beginning of the crystallization process is different from wild angle X-ray diffraction pattern of the β form (Figure 6-2 **(a)**), and then transferred into the β form (Figure 6-2 **(b)**).

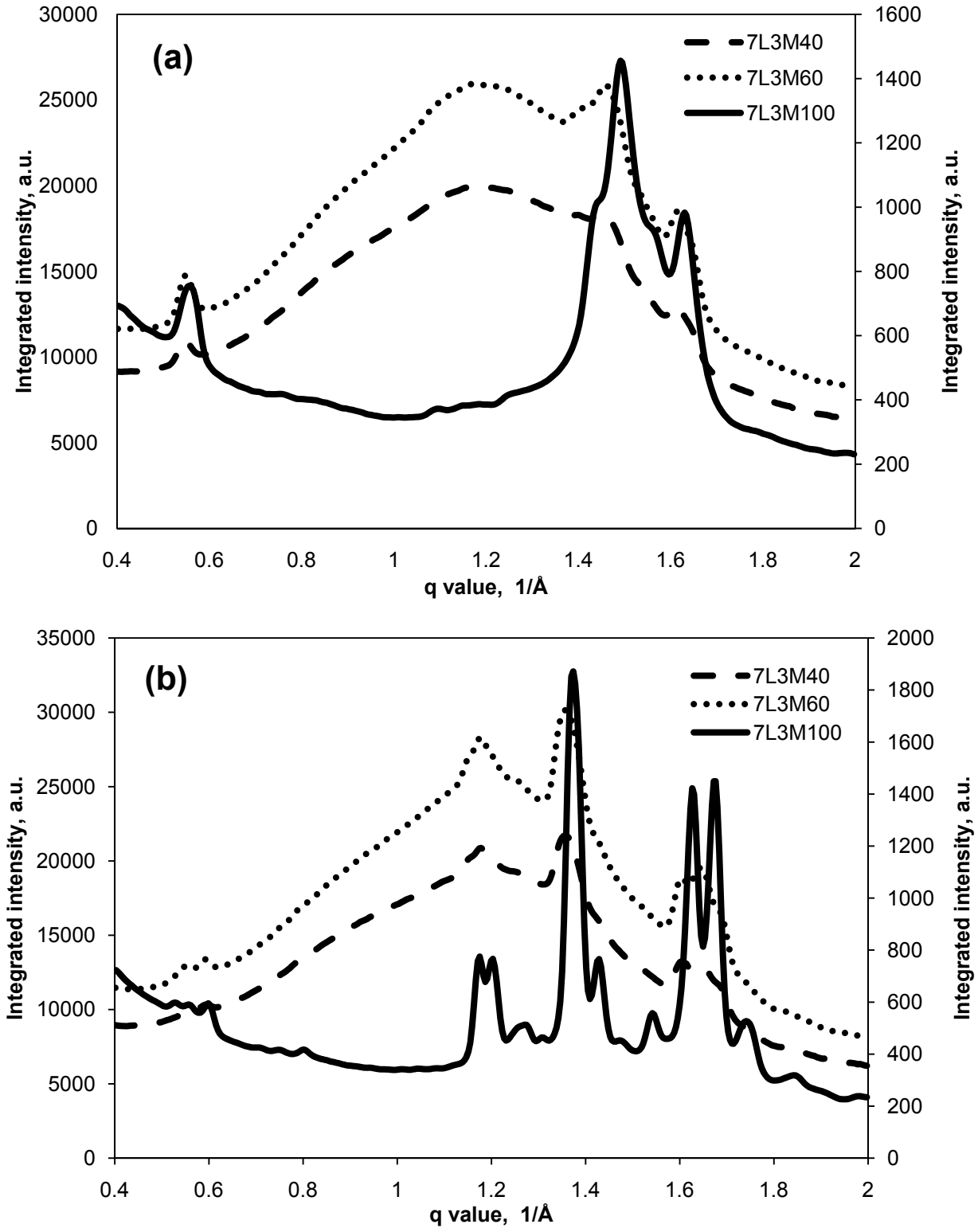

Figure 6-1 The WAXD measurements of the diluted binary mixture sample (7L3M40 and 7L3M60) and the dry binary mixture sample powder (7L3M100). **(a)** β' form, and **(b)** β form.

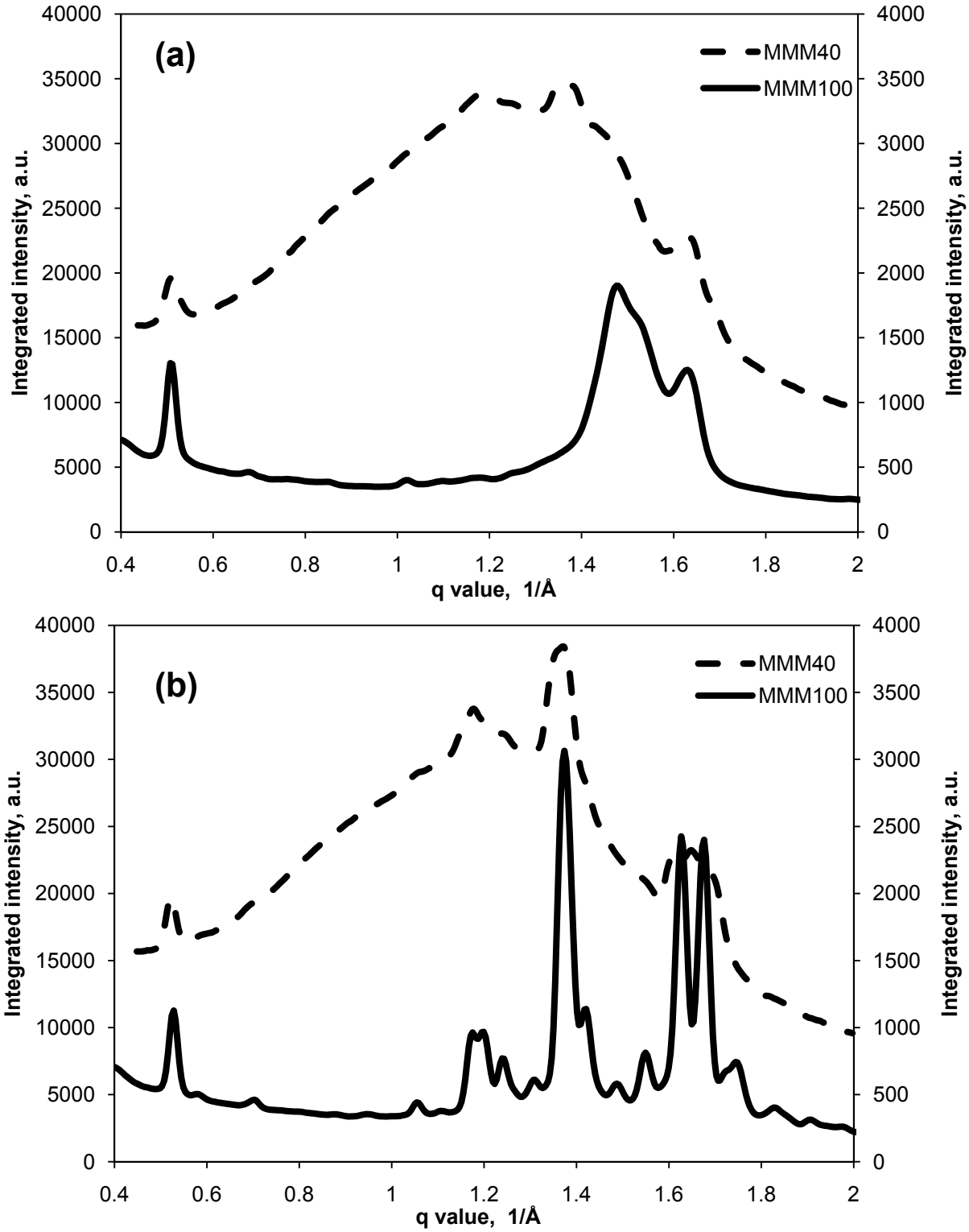

Figure 6-2 The WAXD measurements of the diluted sample (MMM40) and the dry sample powder (MMM100). **(a)** β' form, and **(b)** β form.

6.2.Small Angle X-ray Diffraction Measurements

6.2.1.Orientation

The orientation data recorded for the 3 different temperatures and 4 shear rates are all fairly straightforward. Orientation was detected at high shear rate 80 and 800s^{-1} of each sample. However, at low shear rate 8s^{-1}, sample 3L7M40 presented orientation at all the three crystallization temperatures, sample 5L5M40 was observed orientation at lower temperatures, whereas sample 7L3M40 and 7L3M60 showed no obvious orientation. Figure 6-3 shows the FWHM of the orientation diffraction peaks in degrees, whereas Figure 6-4 shows the area fraction of those peaks.

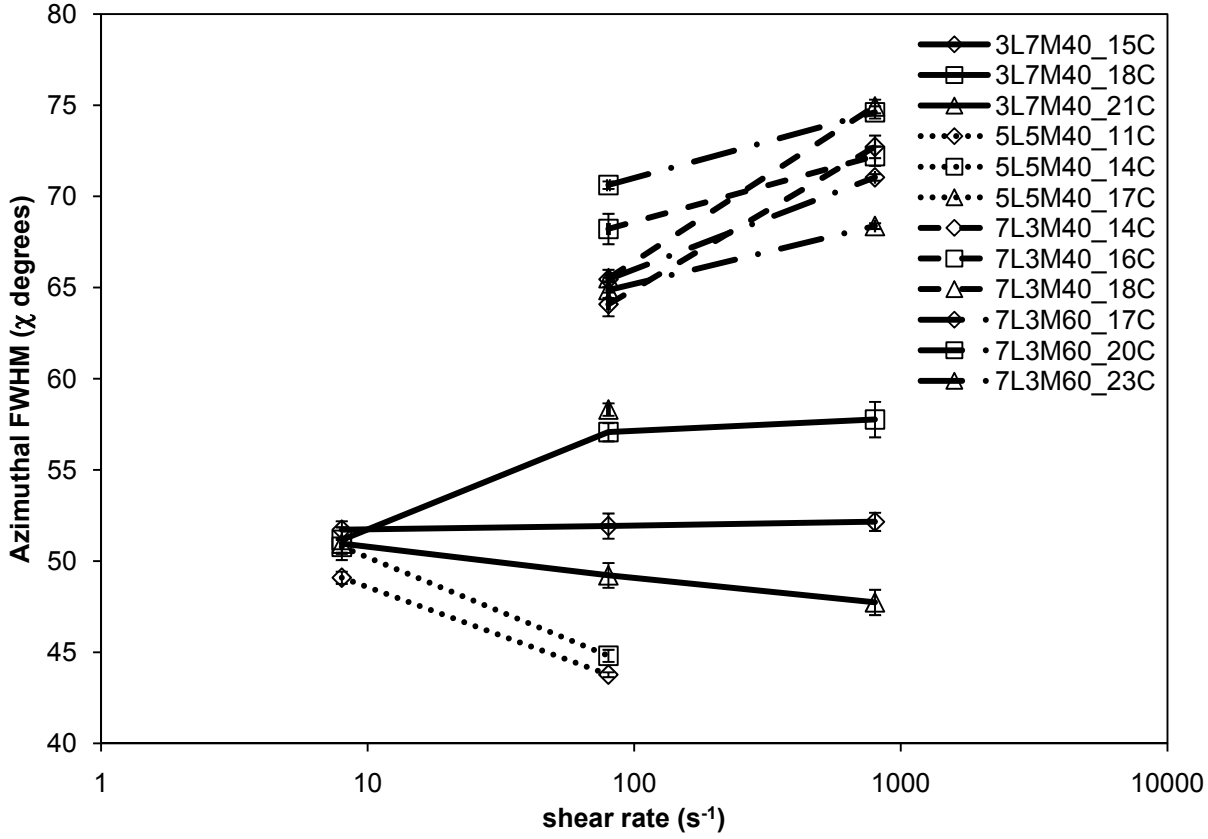

Figure 6-3 The FWHM values of the orientation diffraction peaks of the diluted samples, 3L7M40(——), 5M5L40(- - - -), 7L3M40(– – –), and 7L3M60 (— -).

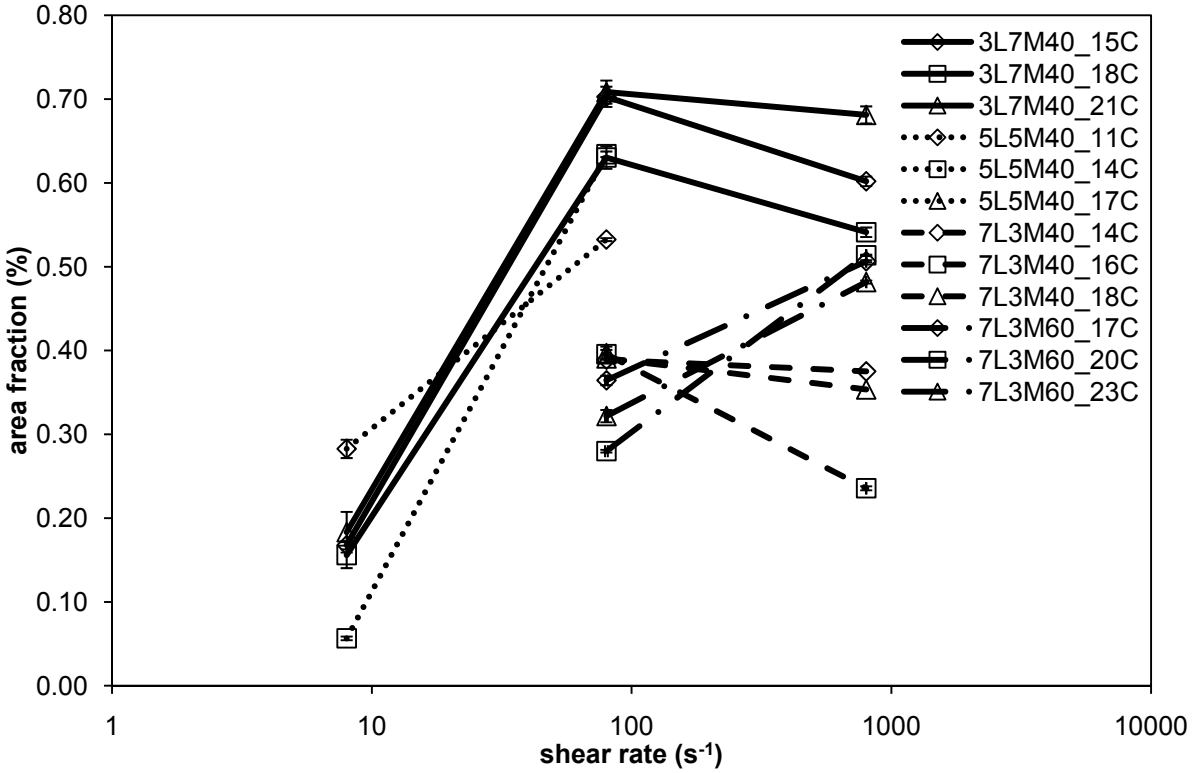

Figure 6-4 The area fractions of the orientation diffraction peaks of the diluted samples, 3L7M40(——), 5M5L40(- - - -), 7L3M40(– – –), and 7L3M60 (— -).

Normally, a narrow orientation diffraction peak (small azimuthal FWHM value) with an increased area fraction of it implies stronger orientation. Shear, as we know, can organize the particles to be oriented, which has been proved in this work. No obvious orientation was observed from any experiments performed without shear. Some of the samples, 7L3M40 and 7L3M60, did not show orientation even at low shear rate $8s^{-1}$, while all the samples experienced orientation at shear rates 80 and $800s^{-1}$.

Furthermore, stronger orientation at high shear rate was expected from this work, given what has been published on the topic (Mazzanti, *et al.*, 2003, Blaak, *et al.*, 2004, Mazzanti, *et al.*, 2005, 2005). However, the results revealed two opposite situations. The azimuthal FWHM values tend to increase with the shear rate raise for all the binary samples except 5L5M40 and 3L7M40 at high temperature, whose values tend to decrease with increasing shear rate. The area fractions of the orientation diffraction peaks of all the samples experienced enhancements when shear rate rose from 8 to $80s^{-1}$. However, both the samples 3L7M40 and 7L3M40 show reduced

area fractions of the orientation diffraction peaks when the shear rate changed from 80 to 800s-1 (sample 5L5M40 lack of data) while the sample 7L3M60 is an exception that shows an increase in the area fraction. It might be explained by the different proportion of solid component. With more crystals, it is likely to gain a more obvious orientation than the other samples. For the samples having 40% crystallisable materials inside, it is surprising that there is no apparent orientation growth from shear rate 80 to $800s^{-1}$ as it is from 8 to $80s^{-1}$. However, it is not hard to understand considering the results obtained from the rheo-NMR system having the same pattern. The high shear rate $800s^{-1}$ causes the crystals dwindle in size dramatically, therefore they are not easily oriented any more. The fat crystals studied in this research are platelet shaped particles, whose sizes can be defined by two parameters, the aspect ratio and the thickness. A large particle with big aspect ratio tends to orient more than the small one with small aspect ratio. Shear has an influence on the thickness of the crystal and also its aspect ratio. Unfortunately, there are some difficulties to measure the aspect ratio of the crystals by using the instruments occupied in this work, XRD or NMR. But it is possible to find the thickness of the particles, more preciously, the thickness of the crystal domain, by analyzing the SAXD data.

6.2.2.Thickness of the Crystal Domain

A single crystal is sometimes formed by several domain structures separated by imperfections, while very small single crystals can be made of a single coherently scattering domain. Hence, the size of the crystal is proportional to the size of the domain, or even equal to that size. For this work, the thickness of the domain can be estimated as $\xi = \frac{2\pi}{\Delta q}$, as been demonstrated in section 3.3.1.

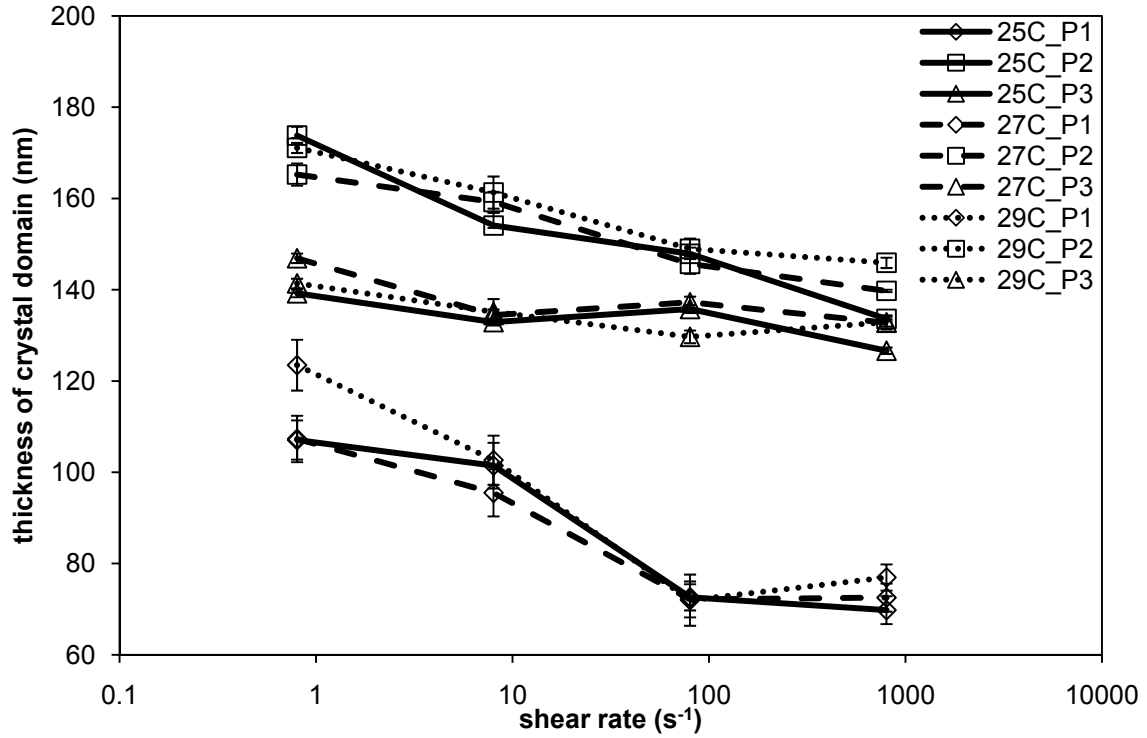

Figure 6-5 The thickness of the crystal domain obtained from the diluted sample MMM40 as a function of shear rate.

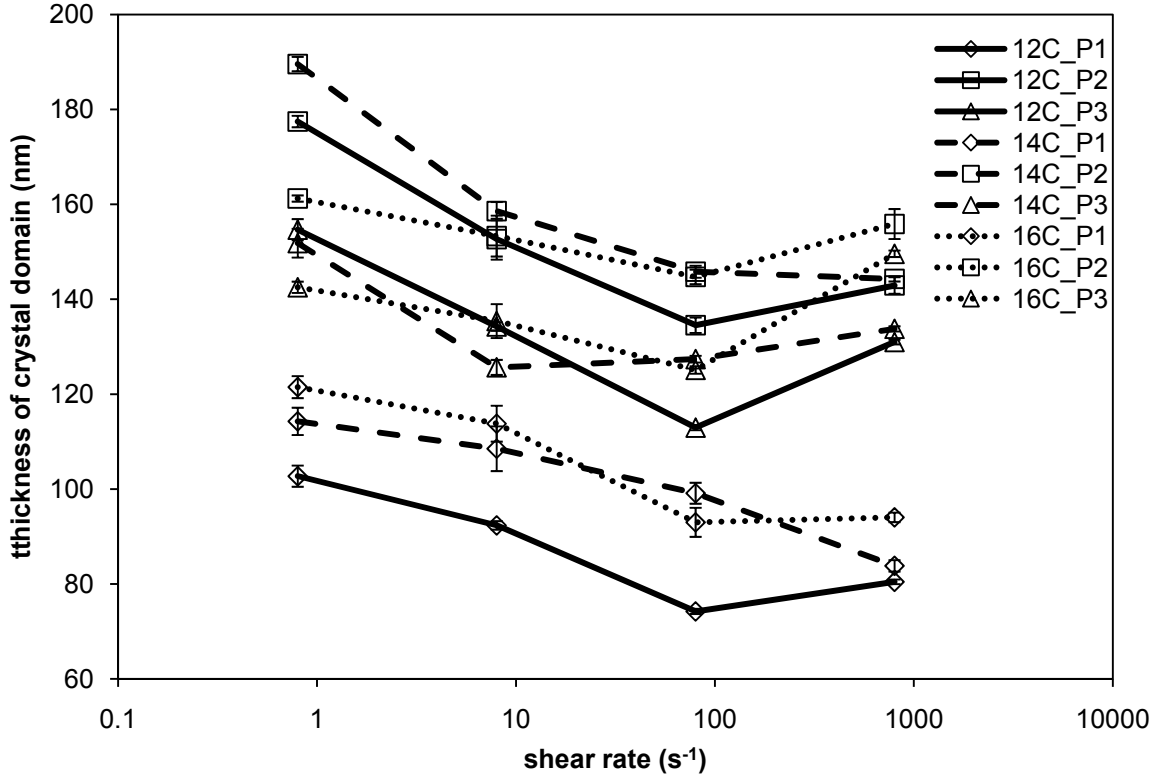

Figure 6-6 The thickness of the crystal domain obtained from the diluted sample LLL40 as a function of shear rate.

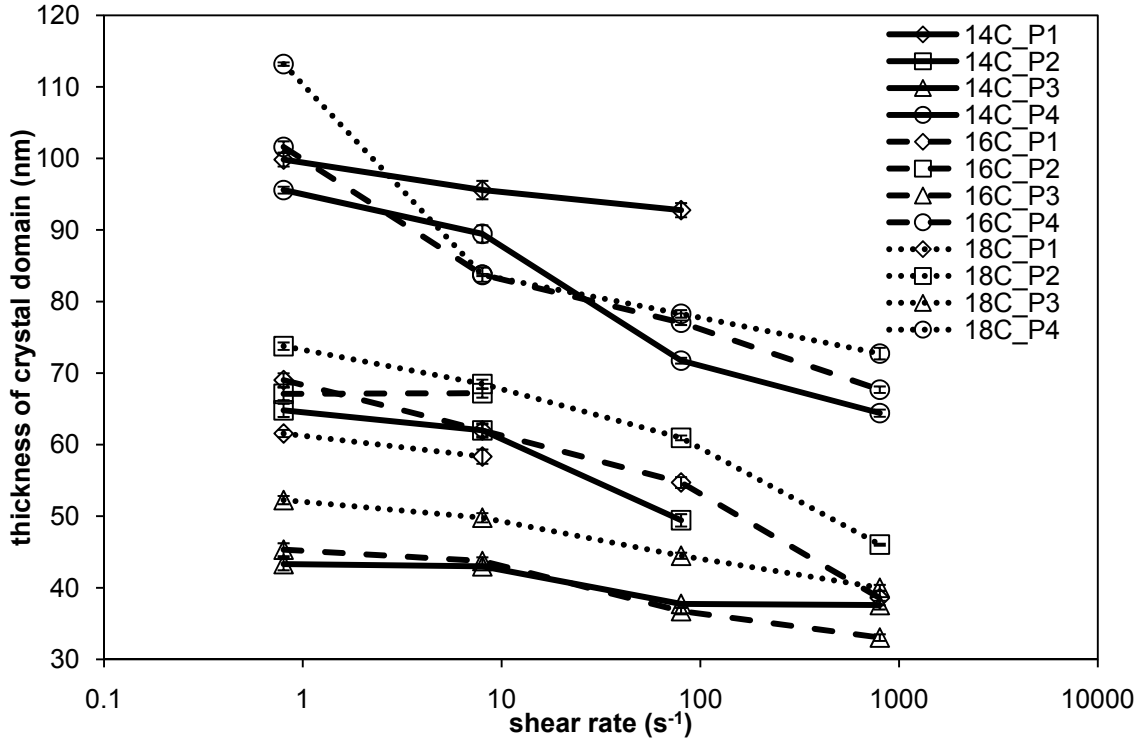

Figure 6-7 The thickness of the crystal domain obtained from the diluted sample 7L3M40 as a function of shear rate.

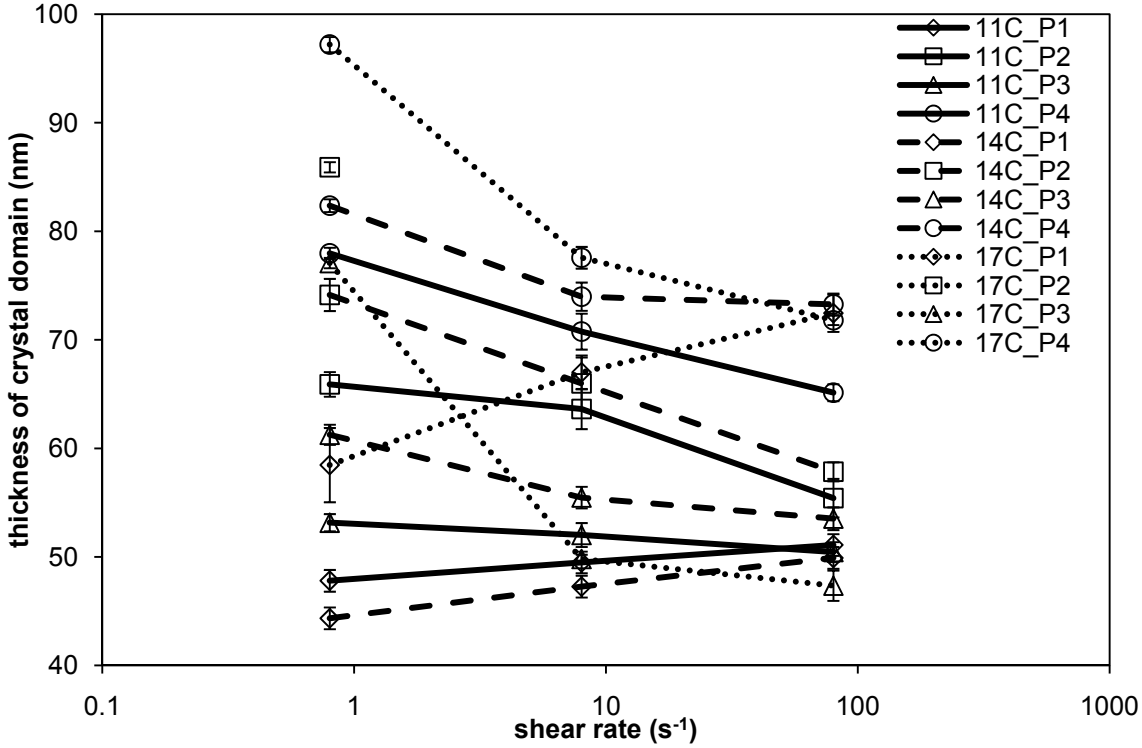

Figure 6-8 The thickness of the crystal domain obtained from the diluted sample 5L5M40 as a function of shear rate.

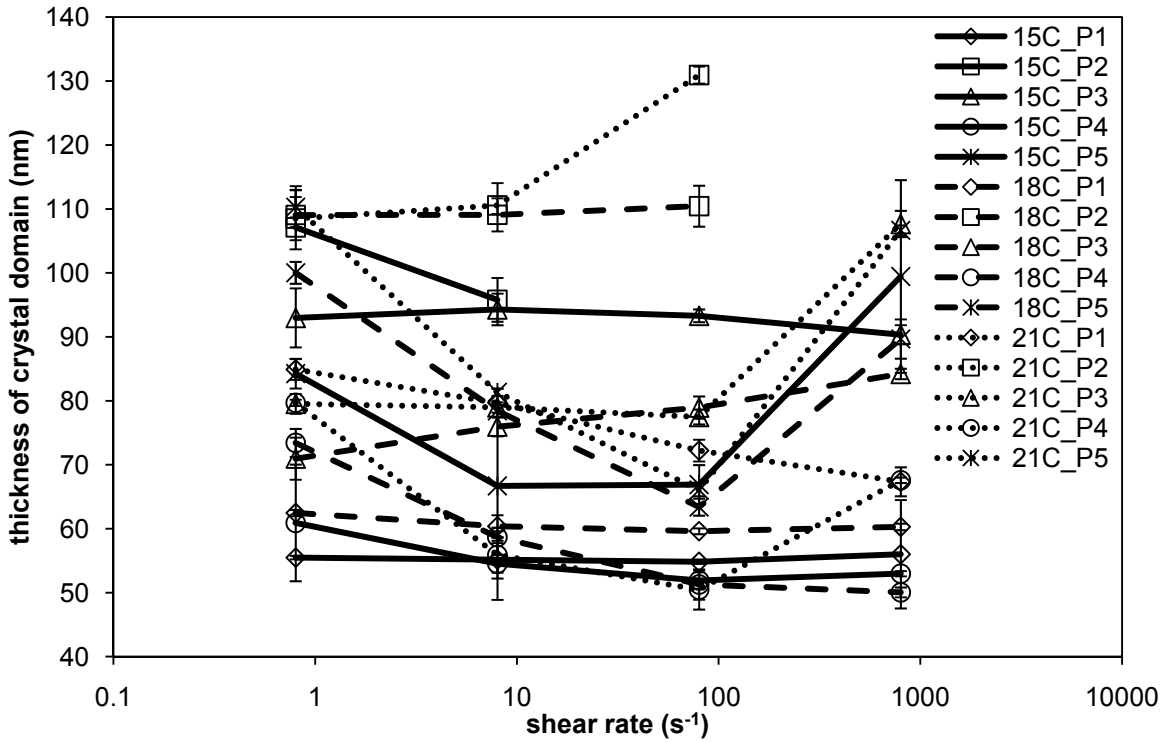

Figure 6-9 The thickness of the crystal domain obtained from the diluted sample 3L7M40 as a function of shear rate.

Figures 6-5 to 6-9 show the thickness of the domain of each sample as a function of shear rates. It is clear that all of them display the same pattern, perhaps less clearly for 3L7M40. The thickness decreases with the shear rate increasing. The shear applied to the system reduces the thickness of the crystals. One can suspect that the change of the thickness is the only reason causing the less orientation effect. However, there was a ten time shear rate increase with only a small proportion of the thickness reduction. The other parameter, the aspect ratio may also play a role in this case. As the aspect ratio has not been measured directly, the Peclet number (Larson, 1999) is introduced to explore this possibility, which is defined as :

$$Pe = \frac{\dot{\gamma}}{D_r} \tag{29}$$

where $\dot{\gamma}$ is the shear rate and D_r is the rotational Brownian diffusion coefficient, which is inversely proportional to viscosity η_s and particle diameter d_p:

$$D_r = \frac{3k_B T}{\pi \eta_s d_p^3} \tag{30}$$

At $Pe > 10$, orientation effects become obvious. For the experiments preformed at the same temperature, parameters k_B, T and η_s should not change at all. Hence, the D_r in inversely proportional to the particle diameter d_p.

Assuming the only change of the crystal size is the thickness between the experiments of sample 7L3M40 at $80s^{-1}$ and $800s^{-1}$, then:

$$\frac{Pe_{800}}{Pe_{80}} = \frac{\frac{\dot{\gamma}_{800}}{D_{r_{800}}}}{\frac{\dot{\gamma}_{80}}{D_{r_{80}}}} = 10 \cdot \left(\frac{d_{p_{800}}}{d_{p_{80}}}\right)^3 = 10 \cdot \left(\frac{45}{65}\right)^3 = 3.32 \quad (31)$$

which means without any change on the aspect ratio, the orientation effects would still be much stronger at the shear rate $800s^{-1}$ than $80s^{-1}$. Therefore, the aspect ratio must have been changed to achieve a less orientation effect at high shear rate as it is observed from the results of this work. There is at least 3.32 times diminishment of the aspect ratio to keep the orientation effect at the same level in this example. All the other samples seem to have the same trend. High shear reduces the orientation effect by cutting down the size of the crystal, including the thickness, but it probably has a more drastic effect on the aspect ratio.

6.2.3.Onset Time of the Phase Transition

In this section, different phases of each sample have been numbered in the order of their d-spacing values decrease, which makes the 'phase1' having the largest d-spacing values obtained from the experiments of this work. It should be noted that the 'phase1's of different samples do not necessarily be the same structure. The onset time was started to count after the sample temperature reaches the goal crystallization temperature of the experiment.

According to this research, different component proportions of the samples may lead to different phases present in the experiments at the same cooling rate and shear rate. They will likely lead to phases of different compositions, even if the polymorphic forms are the same. The binary mixture samples can form more phases than the pure triglycerides samples simply because they can form solid solutions. Both of the pure samples, LLL40 and MMM40, generated 3 different polymorphic phases. In this case there is no compositional variation; therefore the phases can only be different polymorphs. However, the binary mixture samples, 3L7M40,

5L5M40, 7L3M40, and 7L3M60 produced at least 4 different phases during crystallization, yet they seem to exhibit only two different polymorphic arrangements, i.e. β′ and β.

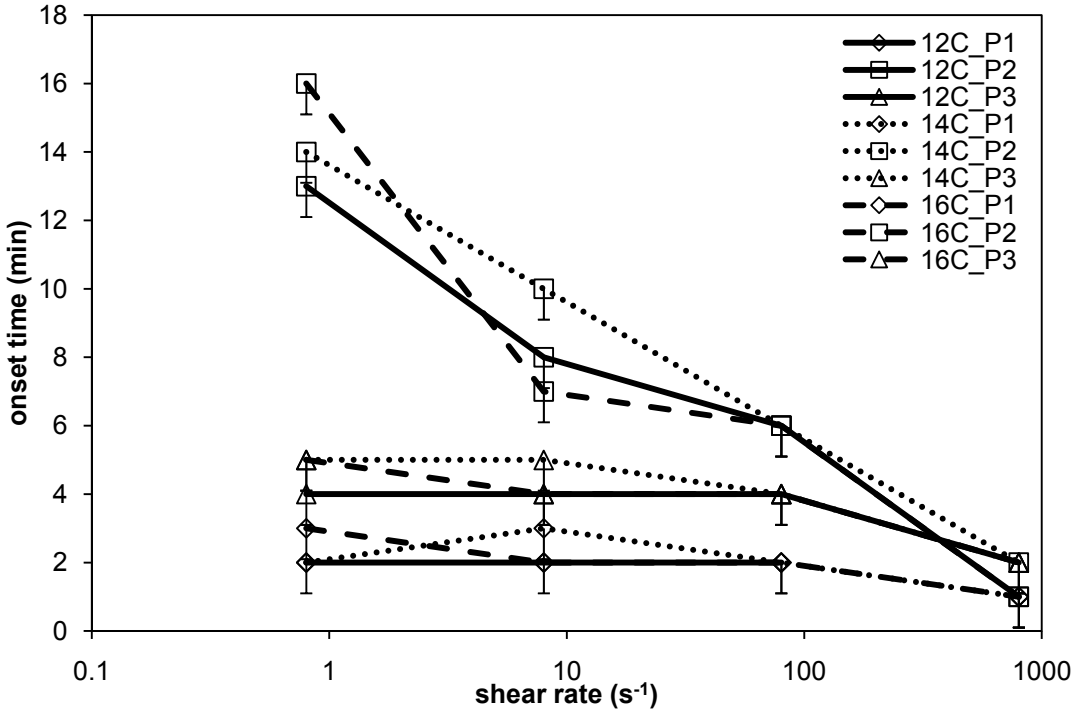

Figure 6-10 The onset time of the three polymorphic phases formed by the diluted sample LLL40 at temperature 12, 14, and 16°C as a function of shear rates.

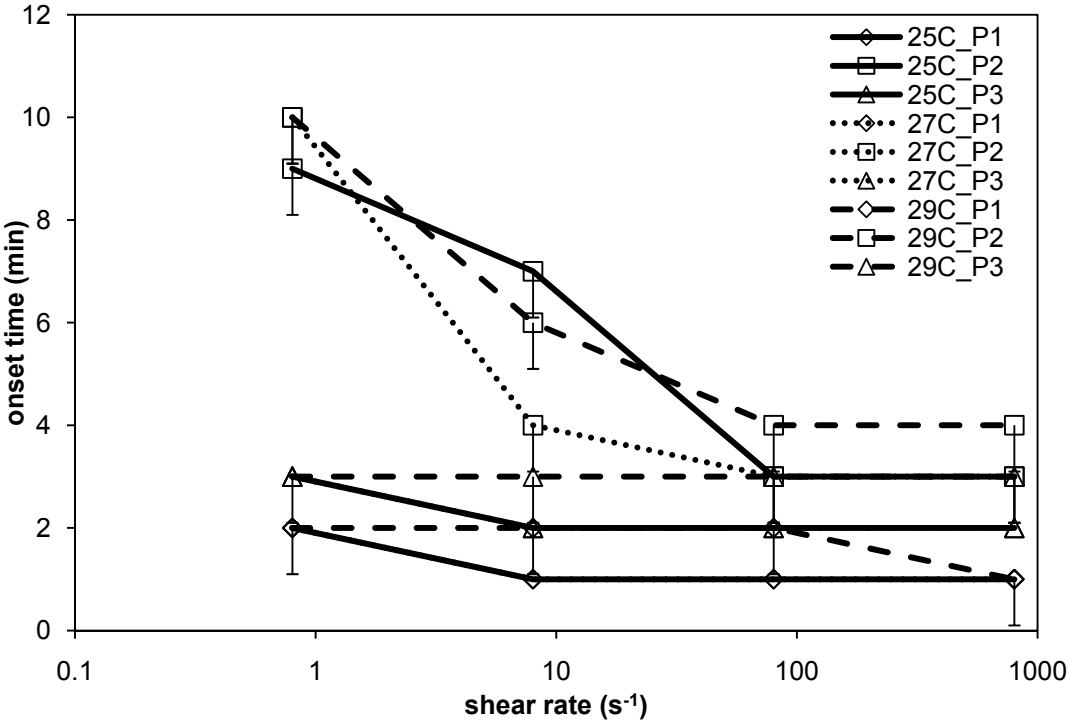

Figure 6-11 The onset time of the three polymorphic phases formed by the diluted sample MMM40 at temperature 25, 27, and 29°C as a function of shear rates.

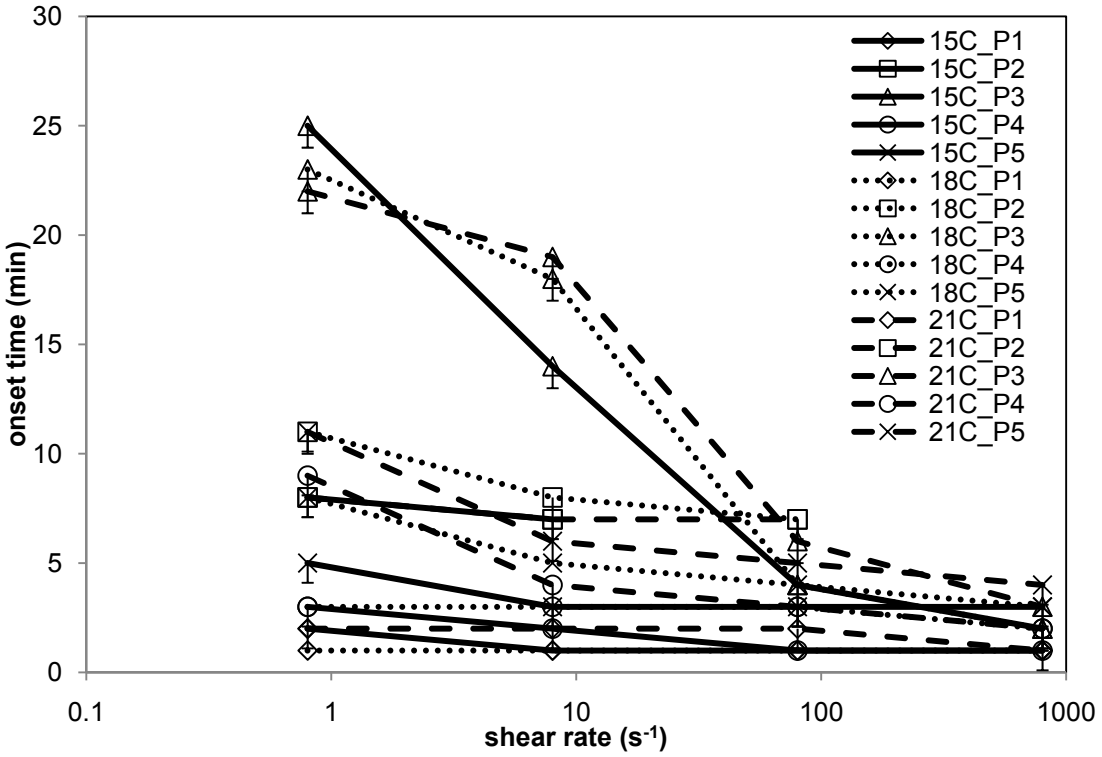

Figure 6-12 The onset time of the five polymorphic phases formed by the diluted sample 3L7M40 at temperature 15, 18, and 21°C as a function of shear rates.

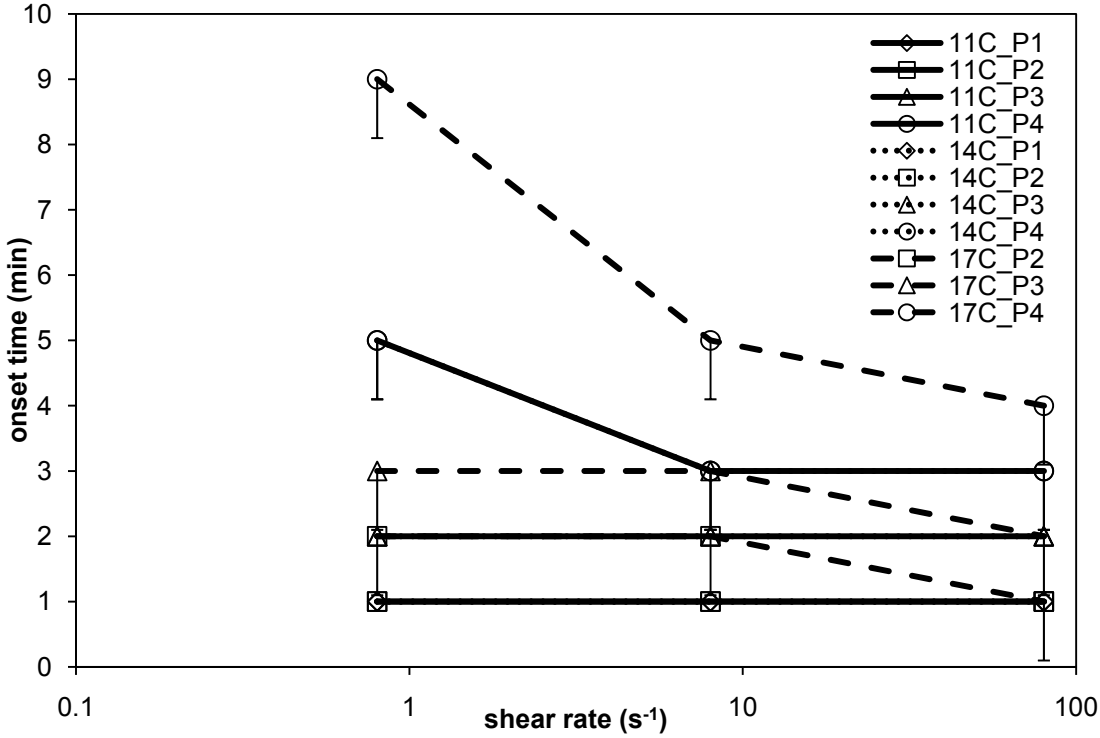

Figure 6-13 The onset time of the four polymorphic phases formed by the diluted sample 5L5M40 at temperature 11, 14, and 17°C as a function of shear rates.

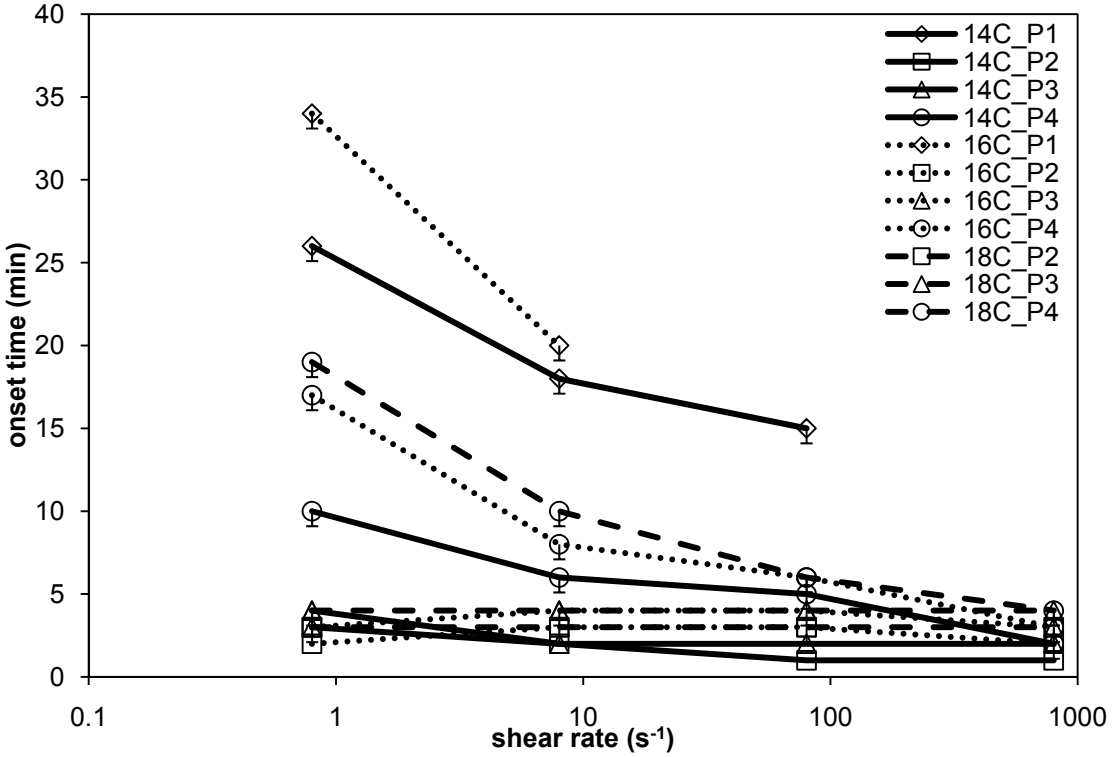

Figure 6-14 The onset time of the four polymorphic phases formed by the diluted sample 7L3M40 at temperature 14, 16, and 18°C as a function of shear rates.

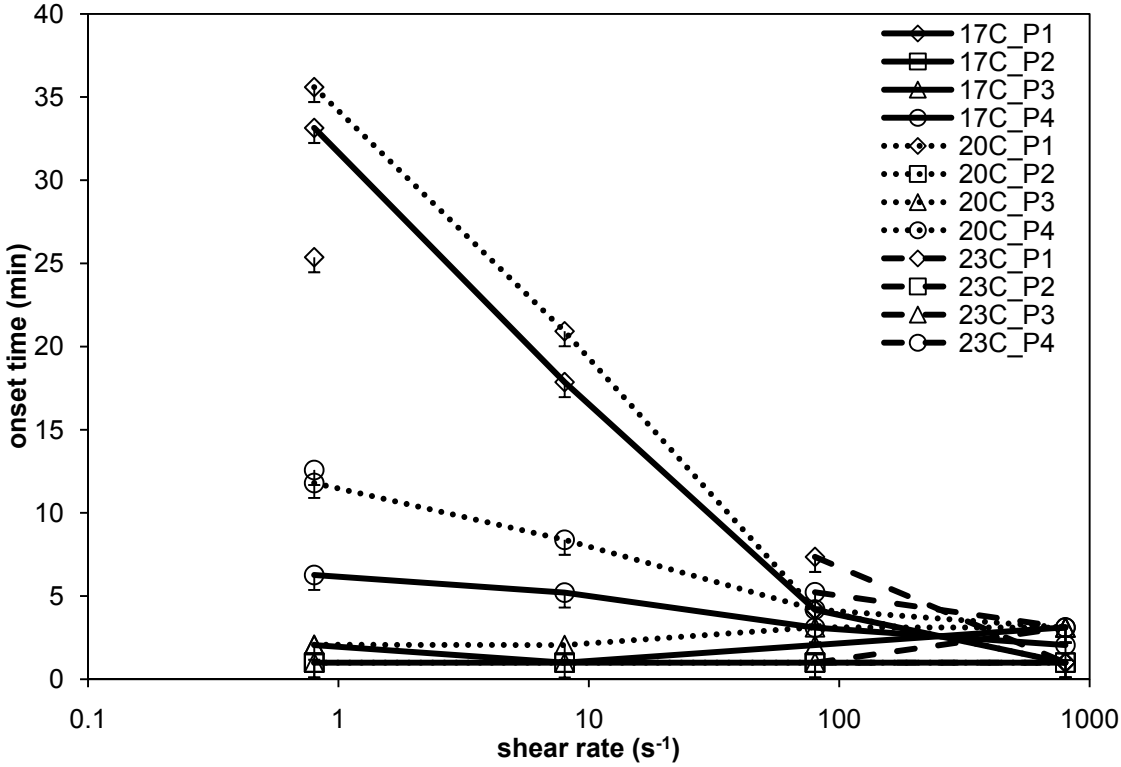

Figure 6-15 The onset time of the four polymorphic phases formed by the diluted sample 7L3M60 at temperature 17, 20, and 23°C as a function of shear rates.

However, there was one thing in common about these different phases on the onset times. It can be seen from Figure 6-10 to Figure 6-15 that the onset times of the more stable phases were observed to be shorter while the shear rates increase, which implies that phase transition happens easier and faster under shear, especially at high shear rates. This result is consistent with the increasing k values found from the NMR measurements. Both of the results present that the shear accelerates the crystallization process, producing large crystallization rate constant and the less onset time of phase formation and transition. The less stable phases, on the other hand, did not reveal much difference in the onset times under various shear rates. The stability of polymorphic phase is normally determined by the lamellar distance, also known as d-spacing value. Smaller d-spacing values denote tighter packed triglycerides molecules which also mean more stable structures in pure triglycerides samples. However, in binary mixtures, the d-spacing values can also be influenced by the different compositions of the solid solution crystals made from the two triglycerides. When crystallized from a triolein solution, trilaurin and trimyristin are inclined to crystallize together, meaning two kinds of triglycerides molecules exist in the same crystal lamellar structure. The proportion of the two kinds of triglycerides affects the molecular packing and then causes different d-spacing values. Since trimyristin has bigger molecules, it is likely that crystals with more trimyristin tend to have bigger lamellar structures. In that case, however, the larger d-spacing values do not necessarily represent less stable phases.

6.2.4.The Lamellar Distance of the Crystals

The lamellar distance, also known as the d-spacing, is a nanostructural characteristic that depends, for a given polymorphic form, on the length of the molecules in the crystal structure. It is in that sense a signature identity of a specific phase of fat crystal. Each phase has its own d-spacing value, and this differentiates it from another. As it was mentioned at the section above there is diversity between the phases formed by different samples. There are also, however, some patterns hidden behind.

Table 0-6 values of the lamellar distance of samples obtained from the SAXD measurements

Sample	d-spacing (nm)							
LLL40	3.14	3.16	3.35	-	-	-	-	-
7L3M40	-	3.16	3.35	3.43	3.55	-	-	-
5L5M40	-	3.16	-	3.43	3.55	-	-	3.75
3L7M40	-	3.16	-	3.43	3.55	3.58	3.63	-
MMM40	-	-	-	-	-	3.58	3.63	3.75

The standard error of the d-spacing values is less than ±0.001.

The samples were presented in the order of the component proportion of trimyristin getting larger in Table 6-1. LLL40 formed three different polymorphic phases. According to the reported d-spacing values from the literatures (Table 2-2), they are likely one β′ form (d-spacing value 3.35) with two β forms (d-spacing values 3.16 and 3.14). MMM40 also formed three phases, which were identified from the WAXD data to be one β′ (3.75nm) and two β forms (3.58 and 3.63nm).

The sample 7L3M40, which has a dominant proportion of trilaurin, shows one of the characteristic d-spacing values of trilaurin, 3.16 and also 3.34 which is shorter than the 3.36 for pure trilaurin. Meanwhile, two more polymorphic phases appear with d-spacing values 3.43 and 3.55. These two particular structures can only be found in the binary mixture samples not in the pure ones. This indicates that the two kinds of triglycerides, trilaurin and trimyristin are inclined to crystallize together instead of crystallizing individually, which is consistent with the previous results. The sample 3L7M40, on the other hand, has a dominant trimyristin proportion, which gives it two fingerprint structures of trimyristin with d-spacing values 3.58 and 3.63. Besides the two phases presented only in binary mixture samples, another phase with d-spacing value 3.16 appears so long as there is trilaurin in the mixture, even only a small proportion (3L7M40) of it.

6.2.5.The Relationship between Mass and Area Fraction of Polymorphic Forms

The diffraction peaks from SAXD reveal another piece of information, the area fraction of the polymorphic forms. The area under each peak over the total area provides the area fraction of the corresponding polymorphic form. However, the area fraction is not directly related to the mass fraction of the polymorphic form, which this research is more interested in. There is

normally a parameter, the ratio of mass to area ψ, defined as $\psi = \frac{\text{mass}}{\text{area}}$, introduced into the computation.

A different molecule packing structure (different polymorphic forms) or a different proportion of molecules of each kind in the same packing structure (same polymorphic form but different composition of the solid solution) influences the value of ψ since the packing determined the proportion of the crystals can be seen under X-rays diffraction measurements. Hence, in the same material, each polymorphic form present has a unique ψ value. The area fractions data were obtained from the results of the multi-peak fitting to find out the mass fractions of different polymorphic forms of the crystals in a sample.

A simplified crystal system, which has only one crystallizable triglyceride with two polymorphic forms, is chosen to demonstrate the relation between the mass of the crystals and the area of the diffraction peaks. The two forms are named as form a and form b. Their relation between the mass and area fractions can be described as:

$$A_a + A_b = A_{total},\ m_a + m_b = m_{total} \tag{32}$$

$$m_a = \psi_a \cdot A_a,\ m_b = \psi_b \cdot A_b \tag{33}$$

where A_a and A_b are the areas of the diffraction peaks of polymorphic forms a and b; m_a and m_b are the mass of the crystals of each form.

If we define $\sigma_a = \frac{A_a}{A_{total}}$, $\sigma_b = \frac{A_b}{A_{total}}$; $S_a = \frac{m_a}{m_{total}}, S_b = \frac{m_b}{m_{total}}$, then for only 2 polymorphic forms system:

$$\frac{m_a}{A_{total}} = \sigma_a \cdot \psi_a + \sigma_b \cdot \psi_b \tag{34}$$

$$1 = A_a \cdot \frac{\psi_a}{m_{total}} + A_b \cdot \frac{\psi_b}{m_{total}} \tag{35}$$

$$S_a = \frac{1}{1 + \left[\frac{1}{\sigma_a} - 1\right]\frac{\psi_b}{\psi_a}} \quad (36)$$

$$S_b = 1 - S_a \quad (37)$$

From Eq. (35), the values of ψ_a and ψ_b can be calculated by the matrix mathematics. Then the only unknown parameter in the equations was $\frac{\psi_b}{\psi_a}$, which can be calculated easily.

The pure triglyceride diluted samples LLL40 and MMM40, which are the ones having 3 polymorphic forms appear under our experiment conditions, present similar patterns. Both of the samples formed three polymorphic forms at the beginning, which were believed to be one β′ and two β forms according to the SAXD and WAXD observations. However, the less stable form β′ tends to disappear after around 20 minutes at the measuring temperature, leaving only two β forms β_a and β_b remained and occupied the total area of diffraction peaks, which fitted the simplified system model just being discussed above. This situation gives us an opportunity to compute at least the ψ values of the two β forms for each sample.

Table 6-2 summarized the values of ψ_{β_a}/m_{total}, ψ_{β_b}/m_{total}, and $\psi_{\beta_b}/\psi_{\beta_a}$ of the two β forms of samples LLL40 and MMM40. The ψ_{β_a}/m_{total}, ψ_{β_b}/m_{total} values of sample LLL40 are larger than the ones of sample MMM40. Considering that most of the crystallisable material has already been solid at that time, which means the total mass of the two samples should be very similar, it estimates that LLL40 produces smaller peak area giving the same amount of crystal mass. It probably can be explained by the smaller molecule size of trilaurin, compared with trimyristin.

Table 0-7 values of $\boldsymbol{\psi_{\beta_b}/\psi_{\beta_a}}$ of diluted samples LLL40 and MMM40

		Shear rate (s^{-1})			
		0	8	80	800
LLL40	ψ_{β_a}/m_{total}	0.017 ±0.001	0.015 ±0.002	0.016 ±0.001	0.018 ±0.001
	ψ_{β_b}/m_{total}	0.019 ±0.000	0.019 ±0.001	0.015 ±0.000	0.017 ±0.001
	$\psi_{\beta_b}/\psi_{\beta_a}$	1.127 ±0.001	1.256 ±0.003	0.946 ±0.001	0.919 ±0.002
MMM40	ψ_{β_a}/m_{total}	0.012 ±0.001	0.013 ±0.002	0.013 ±0.000	0.012 ±0.001
	ψ_{β_b}/m_{total}	0.016 ±0.000	0.015 ±0.001	0.013 ±0.000	0.013 ±0.001
	$\psi_{\beta_b}/\psi_{\beta_a}$	1.321 ±0.001	1.195 ±0.003	0.935 ±0.001	1.086 ±0.002

From the values in Table 6-2, the mass fraction of each β form were calculated and tabulated, seen in Table 6-3. Sample LLL40 experienced an increased β_b form growth with rising shear rates (0, 8, and 80s^{-1}), meaning that the trilaurin crystals tended to form more stable phases during the crystallization when time extended, except the high shear rate 800s^{-1}, which might be explained by the viscous heating of the sample. Sample MMM40, on the other hand, showed the opposite results. The β_a form grew instead of decreasing with arising shear rates. It infers that the β_a form is shear preference phase which can be formed by trimyristin diluted in triolein.

Table 0-8 mass fraction of $\boldsymbol{\beta}$ forms of diluted samples LLL40 and MMM40 at different shear rates

	Shear rates (s^{-1})			
LLL40	0	8	80	800
mass fraction S_{β_a} (%)	28.1 ±0.3	24.0 ±0.2	21.0 ±0.5	43.1 ±0.5
mass fraction S_{β_b} (%)	71.9 ±0.5	75.5 ±0.3	78.9 ±0.6	56.9 ±0.2
MMM40	0	8	80	800
mass fraction S_{β_a} (%)	12.2 ±0.1	12.3 ±0.2	29.0 ±0.3	32.8 ±0.1
mass fraction S_{β_b} (%)	87.7 ±0.1	85.0 ±0.4	70.9 ±0.6	67.0 ±0.2

Both pure triglycerides in solution, LLL40 and MMM40, showed an increasing orientation with increasing shear rate. This behaviour can decrease the ratio of mass fraction to diffraction peak area as shear rate increases. This happens because a larger proportion of the crystals become aligned at the Bragg scattering angle, and is therefore "visible" through XRD.

The slight change of ψ value between different polymorphic forms or phases of the same polymorph but different composition makes it hard to find out from our experimental results, which have at least 3 phases, often in two polymorphic forms. Hence, there is difficulty to compute the ψ values of the polymorphic forms of the binary samples in this work because first there are more phases formed in the experiments of binary samples. Furthermore, a couple structures formed only in binary samples combining two different molecules together, as discussed in section 6.2.4, make this computation even harder.

Despite the complex properties of the solid solutions in the binary triglyceride mixtures, the composition of the solid solution was reported as a function of the d-spacing values of different phases in Anom's work (Anom, 2009). Furthermore, the values of the parameter ψ for the β' polymorph were found for the LLL/MMM binary mixture to establish the relationship between the mass and area fraction for each phase. However, the diluted samples (40% crystallizable material) used in the current work made it difficult to find the ψ values for the β polymorph, compared to the pure powder samples used in Anom's work, because of the reduced signal intensity of XRD measurements. Furthermore, the total mass value, m_{total}, changed in this work due to the shear effect and the solvent effect. Therefore, analyzing the data with reduced signal and various total mass values requires an amount of work and time that was deemed to exceed the limits of this Thesis. However, the data resulting from this work will be used in the future to continue this analysis.

CHAPTER 7 DISCUSSION OF COMBINED RESULTS FROM THE TWO INSTRUMENTAL SYSTEMS

The two systems introduced in this work, rheo-NMR system and rheo-XRD system, offered a great chance to observe the structures of the phases of lipids and their formation crystallization process at the same time. The two systems might not be able to operate simultaneously yet, but the very similar configurations and settings of these two systems with the same temperature control system made it possible to put the results together and complement each other. Therefore, some observation has only been found when the rheo-NMR and rheo-XRD results are analyzed together. These results are very important for us to understand the characteristics of fat crystallization under shear in a dilute binary system.

7.1.Nucleation Dominates the Crystallization Process

Figure 7-1 shows an example of the FWHM dataset for one experiment cycle of sample 7L3M40 at shear rate $80s^{-1}$, crystallization temperature at 18ºC. The thickness of the crystal domain stayed constant before the temperature started to increase at the end. It thus indicates that there was no much change on the thickness of the crystals during the process. Once a crystal formed and reached a certain thickness, it did not grow any thicker. The decline of the thickness at the end of the experiment was caused by the temperature increase. The increase progressively melted the crystals. But before that, the thickness stayed constant from the 1st minute the crystals show up. This indicates that there is natural limit to the thickness of the crystals, depending on the composition and the crystallization conditions.

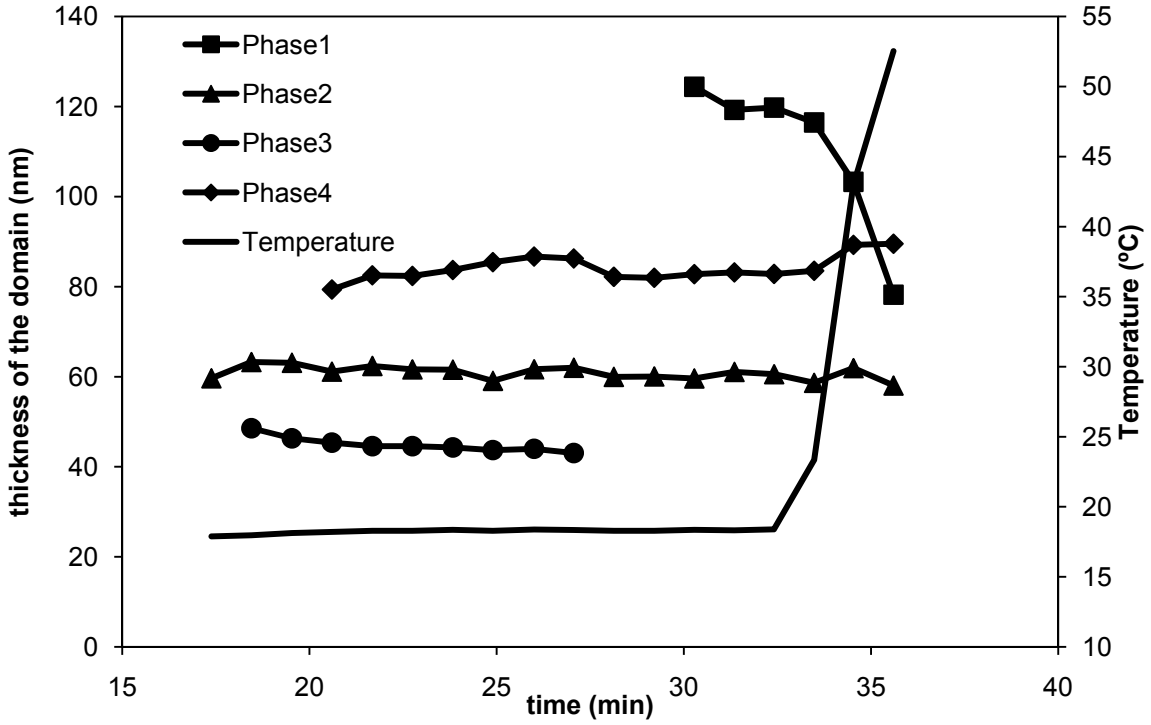

Figure 7-1 The thickness of the crystal domain formed by the diluted sample 7L3M40 at temperature 18°C, shear rate $80s^{-1}$. The black solid line shows the experimental temperature.

The solid fraction data gained from the NMR device for the same experimental condition indicate that it took more than 5 minutes to achieve the maximum SF value from the first crystal been detected. Even during this period of time, the thickness of the crystal domains did not change much, as seen in Figure 7-2. The SF started to grow from 18th to about 24th minute as shown as the black line in this figure. Meanwhile, the three thickness values of crystal domains of different phases remained essentially constant. It is clear that the increase of the SF values was not caused by the crystals growing thicker. Hence, the fat samples generated more nuclei continuously during the crystallization process instead of growing bigger on the crystals already existed. SF value growth thus represents more crystals in the system not thicker crystals. The crystals may have been growing laterally, thus changing its total surface area, so to speak. The aspect ratio of crystals, however, has been found so far to remain more or less constant for a set of crystallization conditions, at least in the case of tristearin (Acevedo and Marangoni, 2010). It is therefore more likely that the total number of crystals is growing.

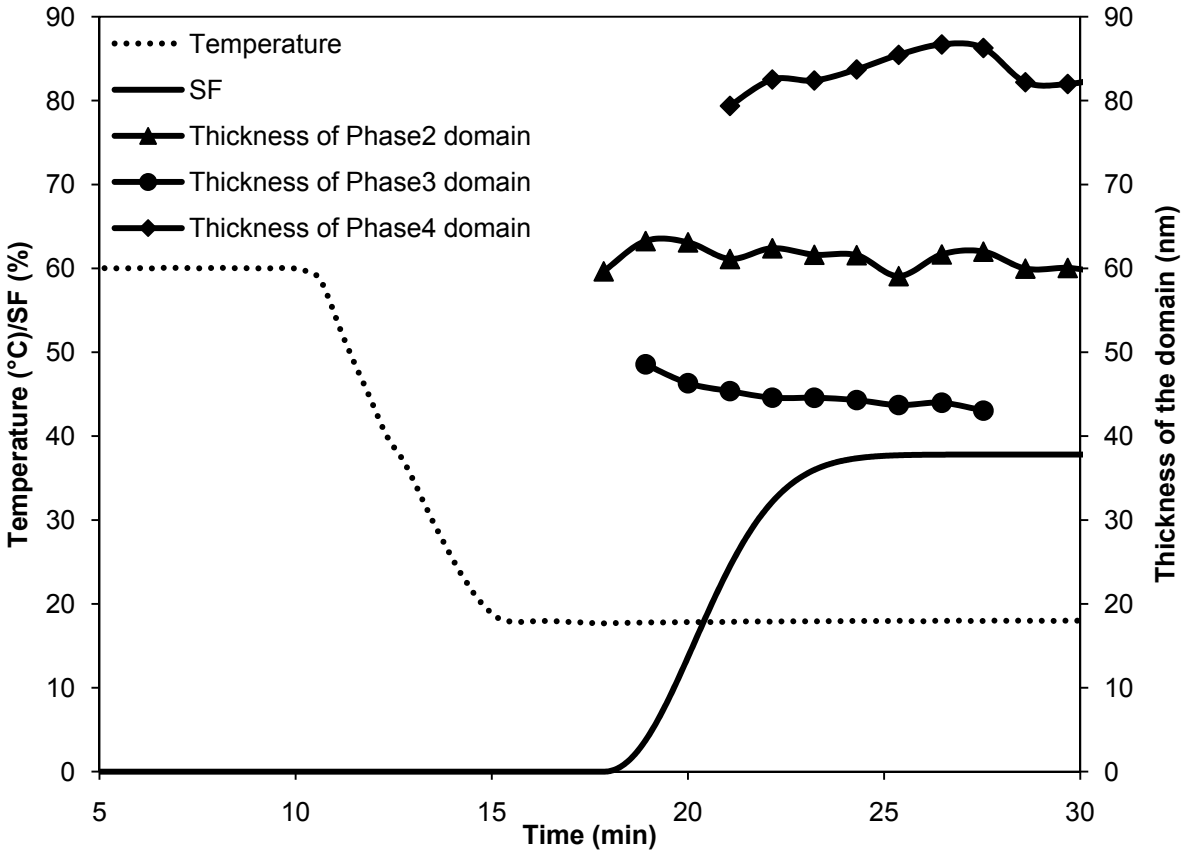

Figure 7-2 The thickness of the crystal domain formed by the diluted sample 7L3M40 at temperature 18°C, shear rate 80s^{-1}. The SF result from the same experiment was also presented in this figure. The black solid line represents the SF values while the black broken line represents the experimental temperature.

7.2.Shear and Temperature Effect on the on the Size of the Crystal Particle and the Intrinsic Viscosity of the Fat Sample Dispersion

It has already been mentioned in section 6.2.2 that the crystal sizes were reduced by the shear rates, both on the thickness and the length-width aspect ratio, which caused a reduced orientation effect on the samples when under high shear.

The Krieger-Dougherty model (section 2.4.2.) was used to analyze the rheological data obtained from this work. From the Krieger-Dougherty equation:

$$ln\left(\frac{\eta}{\eta_s}\right) = -[\eta] \cdot \phi_m \left[ln\left(1 - \frac{\phi}{\phi_m}\right)\right] \quad (38)$$

The solid fraction data ϕ was collected from the NMR device while the viscosity of the fat dispersion was measured by the rheometer. Yet the value of ϕ_m, which is the maximum volume fraction that fat crystals would theoretically achieve under shear, was not precisely determined in this work. The results from the rheometer certainly show the mobility of the sample 7L3M60 as a suspension, which indicates that the binary mixture of LLL and MMM has not reached the maximum volume fraction with 60% crystals. It is consistent with the reported ϕ_m value 0.6-0.7 (Larson, 1999). The viscosity of the solvent was estimated by observing the measured viscosity at the moment when there were no crystals. Therefore, the only unknown, the intrinsic viscosity value in the Krieger-Dougherty equation became easy to calculate by plotting $\ln\left(1-\frac{\phi}{\phi_m}\right)$ versus $\ln\left(\frac{\eta}{\eta_s}\right)$. Figure 7-3 shows one of these experimental charts from sample 7L3M40. The diamonds in the figure represent experimental data points while the black line was added afterwards to show the linear relation between $\ln\left(1-\frac{\phi}{\phi_m}\right)$ and $\ln\left(\frac{\eta}{\eta_s}\right)$ during the crystallization. The slope of that line was $(-[\eta]\cdot\phi_m)$. Since ϕ_m is an unknown constant for the samples, the constant 0.7 from the publications was chosen for computation in this work. The values of intrinsic viscosity of the sample $[\eta]$ were eventually calculated and present in Table 7-1.

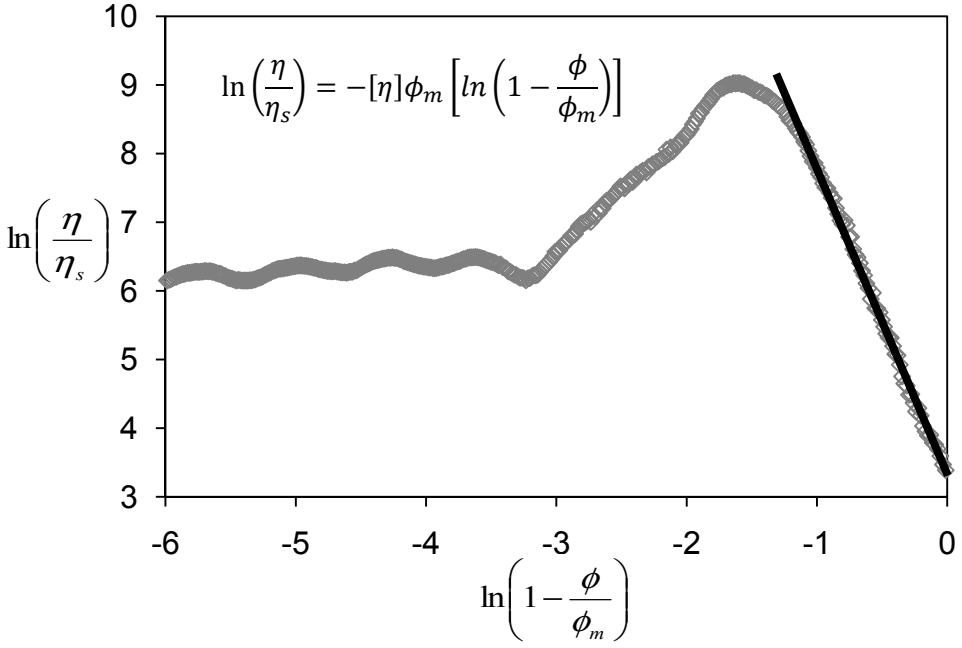

Figure 7-3 The Krieger-Dougherty plot of sample 7L3M40 at crystallization temperature 14°C, shear rate $8s^{-1}$. The slope of the black line equals to $(-[\eta]\cdot\phi_m)$.

The Krieger-Dougherty model requires the change of the volume fraction of particles, which is the solid fraction of the crystals in this work, thus it can only be used during the period of the viscosity increasing due to the crystal formation. After that, the solid fraction reached a plateau and changed only slightly or not at all. The in-flow microstructures formed by the crystals then began to break down due to the shear. This made the calculation of intrinsic viscosity using the Krieger-Dougherty model not feasible in that regime.

Table 0-9 values of intrinsic viscosity [$\boldsymbol{\eta}$] obtained from Krieger-Dougherty model for sample 7L3M40 at three different shear rates (8, 80, and 800s^{-1}) and temperature (14, 16, and 18°C).

Sample 7L3M40	Temperature (°C)		
shear rate (s^{-1})	14	16	18
8	7.73 ±0.07	8.00 ±0.13	8.72 ±0.05
80	6.36 ±0.06	5.58 ±0.07	4.66 ±0.10
800	15.11 ±0.08	9.83 ±0.09	3.94 ±0.08

The different [η] values between experiments represent the differences between the crystal sizes and shapes.

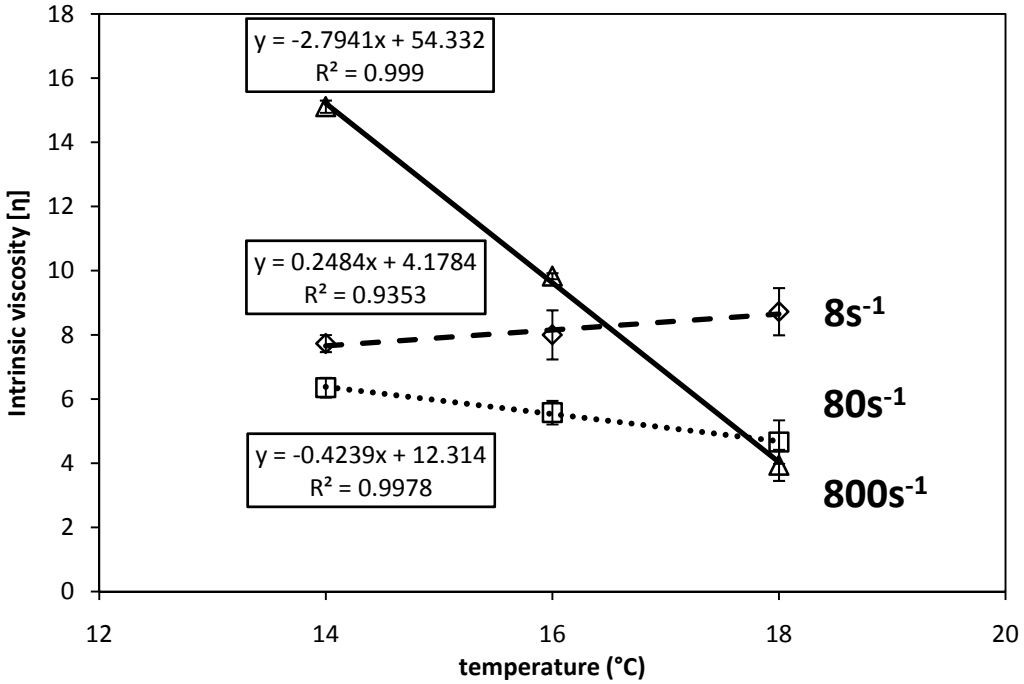

Figure 7-4 The relation between intrinsic viscosity and shear rate of sample 7L3M40 as a function of temperature.

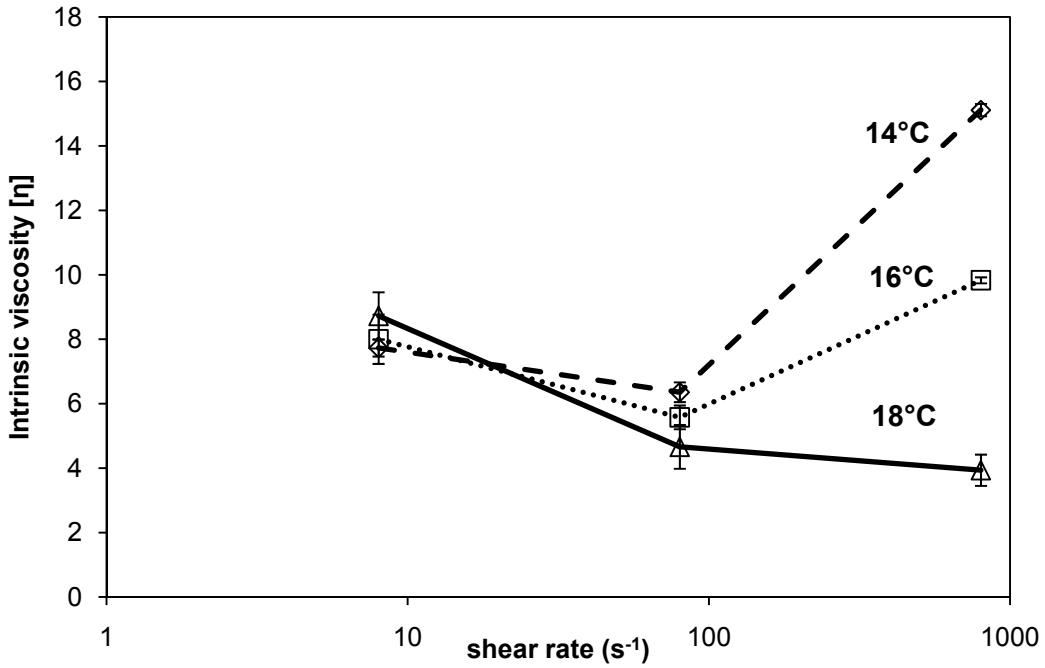

Figure 7-5 The relation between intrinsic viscosity and temperature of sample 7L3M40 as a function of shear rate.

The intrinsic viscosity summary in Table 7-1 can also be seen in Figure 7-4 and 7-5 as a function of temperature and shear rate, respectively. The intrinsic viscosity values obtained from the three different measuring temperatures stay as similar to each other with a slight trend of increasing at shear rate $8s^{-1}$, which is the low one in this work. It estimates that the low shear rate does not affect the size of the crystals a lot. It may actually encourage the larger particle formation by moving the crystals around and helping them get into each other. The slight trend of intrinsic viscosity increasing may also be explained by the rising temperature. However, from the experiments performed at the shear rate 80 and $800s^{-1}$, the intrinsic viscosity starts to decrease when the temperature goes higher. This opposite trend in the intrinsic viscosity values is probably caused by the shear, working against the temperature. Shear can hinder the crystal growing into large particle and even stop the formation of the cluster structure when a high shear rate applied. However, the reason that the smaller intrinsic viscosity values found at shear rate $80s^{-1}$ rather than $800s^{-1}$ in this work is that the heat generated by shear at high shear rate $800s^{-1}$ is not negligible anymore in the Couette system that the samples have been heated up, causing some deviations. Furthermore, this deviation has been proved by the results from the NMR measurements in the same work. Although with an increasing Avrami rate constant k, the

Avrami exponent n, a function of the number of dimensions in which growth takes place, is not following the sample trend when the shear rate rises. Instead, the maximum n value is found at shear rate $80s^{-1}$ again, which represents that the crystals have more freedom to grow. By putting the two parts of results together, it is likely to estimate that the small size of particle gives more dimensions in which growth takes place as happening at shear rate $80s^{-1}$, whereas the bigger particle forms and reduces the freedom of growth at shear rate $800s^{-1}$ because of the viscous heat of samples.

CHAPTER 8 SUMMARY AND CONCLUSION

The goal of this work was to investigate the characteristics of crystalline nanostructures and microstructures formed by binary triglyceride mixtures crystallized from a solution under shear flow. The same rheometer was used to provide shear flow during synchrotron radiation X-ray diffraction and nuclear magnetic resonance experiments in geometrically similar cells. This has enabled us to study the crystallization process and resultant phases (polymorphism and composition) obtained from the crystallization of binary mixtures of trilaurin and trimyristin dissolved in triolein.

The materials were subjected to shear flow and examined with the XRD instrumentation described in section 3.3. As has been observed in natural lipid systems, a reduction of the onset time for the formation of crystalline phases was found as the shear rate was increased. This effect was especially notorious for the most stable β phase in the pure diluted trilaurin and trimyristin samples and also in the diluted binary mixture samples. It supports the universal fact that shear flow does accelerate the phase formation and transition. Mazzanti and coworkers (Mazzanti*, et al.*, 2003) had stated that the shear forces applied to the crystal surfaces may be responsible for the acceleration of the phase transitions. However, in their later papers (Mazzanti*, et al.*, 2005, Mazzanti*, et al.*, 2007), the aggregation-segregation competing mechanisms were discussed as a more likely determinant factor in the modification of the kinetics of phase transitions. If the crystals are tightly clustered, as in a static system, it is more difficult to produce large structural changes. Furthermore, the concentration gradients induced in the liquid span longer distances, making the transport processes more difficult than for a collection of segregated particles in contact with a well-mixed liquid, as in a shear-induced system. A small amount of shear is enough to enhance mixing in the presence of crystals in a suspension. The segregation also results in a much larger active interface area between the liquid and the solid phases than under static conditions where agglomeration is present. This larger area increases the number of nucleation sites available for new phases to appear and thus boosts the probability of nucleation onset. Shear is also likely to produce a significant enhancement of heat transfer and to foster crystallite collisions.

The solid fraction of the materials was measured with the NMR instrument described in section 3.4. Most of the results were described accurately by the Arvami Model. However, in four cases the presence of two regimes was observed, where diffusion controlled growth dominated the later times. The Avrami rate constant k increased with rising shear rate and decreased with rising crystallization temperature. High values of k often appear when there is a large nucleation and growth rate. Sample 5L5M40 displayed k values from 0.47 (high temperature 19ºC) to 0.81 (low temperature 11ºC) at shear rate $8s^{-1}$ indicating that high crystallization temperature produces a lower level of supercooling. The fat sample then has less driving force to crystallize. Same trend is found in sample 7L3M40. On the other hand, Sample 7L3M40 showed k values from 0.20 (high temperature 18ºC, low shear rate $8s^{-1}$) to 0.75 (low temperature 14ºC, high shear rate $800s^{-1}$). This indicates that besides the temperature effect, applied shear also promotes the nucleation and growth rate during the crystallization, which is consistent with the data from XRD measurements. How exactly this is happening is still a matter of speculation.

The data from the rheo-NMR crystallization experiments were used to compute the intrinsic viscosities from the Krieger-Dougherty equation for different shear rates and temperatures. The intrinsic viscosity is related mostly to the shape and, to some extent, to the size of the crystalline nanoparticles. The small values of the intrinsic viscosity (4.66-6.36) were observed at shear rate $80s^{-1}$ showing that the particles were small in size compared to the intrinsic viscosity values at shear rate $8s^{-1}$ (7.73-8.72), which supports the hypothesis that shear reduces the particle size. It is consistent with the largest Avrami exponent n value found at shear rate $80s^{-1}$, since smaller crystals increase the chance for a tridimensional growth due to the less chance for the crystals interfering with each other. There is no doubt that viscous heating was the main reason which larger particle size and limited numbers of crystal growth dimensions were found at the higher shear rate of $800s^{-1}$. It is also likely that the crystallization went through an instantaneous nucleation stage at shear rate $800s^{-1}$ due to the shear-accelerated crystallization process, resulting on much smaller n values.

Wide angle X-ray diffraction measurements allowed us to identify the polymorphic forms that appeared during the crystallization in the diluted triglycerides samples. The forms observed in the final crystallization stages were the forms β′ and β. It was also observed that at least two

sub-modifications of polymorphic forms β and β′ were present in both of the diluted pure triglycerides samples, trilaurin and trimyristin in this work. Furthermore, the d-spacing results from the small angle X-ray diffraction measurements showed clear evidence of the formation of solid solutions in the β form, previously considered unlikely, in the binary mixtures. However, as was observed with undiluted triglycerides, different submodifications did not appear in the mixtures, but only in the pure triglycerides. There were at least 3 different phases obtained from pure triglycerides samples, which have to be different polymorphs or sub-modifications of a polymorph. The number of phases observed was larger for the binary mixtures, but not because they exhibited many polymorphic forms. In fact, only two polymorphic forms were found at the end of the crystallization process. The different phases in the mixtures have different compositions, i.e. they are solid solutions. This situation made it difficult to find the relation between the area of the diffraction peak and the mass of a given phase. This ratio is necessary for quantitative evaluation of the proportions and compositions of the phases. The ratio depends on the experimental setup (which was common to all experiments) and on the structure factor of each specific phase. It was done by this work, to compute at least the ratios of mass fraction to area fraction for pure triglycerides samples.

The orientation of sheared samples was also examined using X-ray diffraction technique. In all of the temperature sets, orientation was present for shear rates of $80s^{-1}$ and higher in all the measured samples. In some of the samples (3L7M40 and 5L5M40), the orientation effect was clear to see even at a shear rate of $8s^{-1}$.

BIBLIOGRAPHY

Acevedo, N. C. and Marangoni, A. G. (2010). "Characterization of the Nanoscale in Triacylglycerol Crystal Networks." Cryst Growth Des **10**(3): 327.

Ackerson, B. J. and Pusey, P. N. (1988). "Shear-Induced Order in Suspensions of Hard Spheres." Physical Review Letters **61**(no. 8): 1033.

Andereck, C. D*., et al.* (1986). "Flow Regimes in a Circular Couette System with Independently Rotating Cylinders." Journal of fluid mechanics **164**: 155

Anom, E. (2009). "Comparison of the Theoretical and Experimental Composition of Crystallizing Lipid Mixtures." Emmanuel Anom's MSc. Thesis.

Avrami, M. (1939). "Kinetics of Phase Change. I General Theory." J. Chem. Phys **7**: 1103.

Avrami, M. (1940). "Kinetics of Phase Change. Ii Transformation - Time Relations for Random Distribution of Nuclei." J. Chem. Phys **8**: 212.

Avrami, M. (1941). "Granulation, Phase Change, and Microstructure Kinetics of Phase Change. Iii." J. Chem. Phys **9**: 117.

Barnes, H. A*., et al.* (1989). "An Introduction to Rheology." Elsevier: New York: 119.

Blaak, R*., et al.* (2004). "Crystal Nucleation of Colloidal Suspensions under Shear." Physical Review Letters **93**(6): 1.

BNLWebsite "www.bnl.gov."

Bragg, W. L. (1913). "The Structure of Some Crystals as Indicated by Their Diffraction of X-Rays." Proceedings of the Royal Society of London **89**(610): 248.

Briggs, J. L. (2003). "Influence of Shearing and Time on the Rheological Properties of Milk Chocolate During Tempering." 3rd International Symposium on Food Rheology and Structure.

Buchheim, W. (1970). "Distribution of High-Melting Triglycerides in Fat Globules of Milk." Naturwissenschaften **57**(1): 41.

Cebula, D. J*., et al.* (1992). "Neutron Diffraction Studies of Liquid and Crystalline Trilaurin." Journal of American Oil Chemists' Society **69**(no.2): 130.

Christian, J. W. (1965). "The Theory of Transformations Iin Metals and Alloys." Pergamon Press, London.

Clarkson, C. E. and Malkin, T. (1948). "An X-Ray and Thermal Examination of the Glycerides. Part I X. The Polymorphism of Simple Triglycerides."

Corkery, R. W*., et al.* (2007). "A Case for Discotic Liquid Crystals in Molten Triglycerides." Langmuir **23**: 7241.

Couette, M. M. (1890). "Études Sur Le Frottement Des Liquides." Ann. Chem. Phys. **6**(Ser. 21): 433.

Cullity, B. D. and Stock, S. R. (1978). "Elemnets of X-Ray Diffraction. 2 Ed." Addison-wesley publishing company, Inc.

DeGraef, V*., et al.* (2006). "Rheological Behavior of Crystallizing Palm Oil." European Journal of Lipid Science and Technology **108**: 864.

DeGraef, V*., et al.* (2008). "Development of a Rheological Method to Characterize Palm Oil Crystallizing under Shear." European Journal of Lipid Science and Technology **110**: 521.

DeGraef, V*., et al.* (2009). "Influence of Shear Flow on Polymorphic Behavior and Microstructural Development During Palm Oil Crystallization." European Journal of Lipid Science and Technology **111**.

DeKruif, C. G*., et al.* (1985). "Hard Sphere Colloidal Dispersions: Viscosity as a Function of Shear Rate and Volume Fraction." Journal of Chemical Physics **83**(9): 4717.

Dhonsi, D. and Stapley, A. G. F. (2006). "The Effect of Shear Rate, Temperature, Sugar and Emulsifier on the Tempering of Cocoa Butter." J Food Eng **77**: 936–942.

Erofeev, B. (1946). "Generalized Equation of Chemical Kinetics and Its Application in Reactions Involving Solids." Compt Rend Acad Sci USSR **52**: 511.

Feuge, R. O*., et al.* (1962). "Tempering Triglycerides by Mechanical Working." Journal of the American Oil Chemists Society **39**(7): 310.

Fisher, D. J. and Kurz, W. (1992). "Fundamentals of Solidification, 3rd Edition." Trans Tech Publications, Switzerland.

Flöter, E. (2009). "The Role of Physical Properties Data in Product Development." European Journal of Lipid Science and Technology **111**: 219.

Garbolino, C*., et al.* (2000). "Ultrasonic Determination of the Effect of Shear on Lipid Crystallization." Journal of American Chemists' Society **77 No.2**: 157–162.

Garside, J. (1987). "General Principles of Crystallization." Food Structure and Behaviour. J.M.W.Blanchard and S. Lillford, editors, London. Academic Press.

Guthausen, A*., et al.* (2004). "Measurement of Fat Content of Food with Single-Sided NMR." Journal of American Oil Chemists' Society **81**: 727.

Guthausen, G., *et al.* (2000). "Soft-Matter Analysis by the NMR-Mouse." Macromol. Mater. Eng. **276**: 25.

Guthrie, S. E. (2008). "Physical Properties of Shear Oriented Cocoa Butter." Ph.D Thesis, University of Waterloo.

Hagemann, J. W. and Rothfus, J. A. (1983). "Polymorphism and Transformation Energetics of Saturated Monoacid Triglycerides from Differential Scanning Calorimetry and Theoretical Modeling." Journal of American Chemists' Society **vol. 60, no. 6**: 1123.

Hartel, R. W. (2001). Crystallization in Foods. Gaithersburg, MD, Aspen Publishers, Inc.

Haw, M. D., *et al.* (1998). "Direct Observation of Oscillatory-Shear-Induced Order in Colloidal Suspensions." Physical Review E **57**(no. 6): 6859.

Hernqvist, L. (1984). "On the Structure of Triglycerides in the Liquid State and Fat Crystallization." Fette, Seifen, Anstrichmittel **86**(8): 297.

Hernqvist, L. (1988). "Crystal Structures of Fats and Fatty Acids." N. Garti, K. Sato, Editors, Crystallization and Polymorphism of Fats and Fatty Acids, Marcel Dekker, New York: 97.

Hornak, J. (1997). "The Basic of NMR." http://www.cis.rit.edu/htbooks/nmr/inside.htm.

Johnson, W. A. and Mehl, R. F. (1939). "Reaction Kinetics in Processes of Nucleation and Growth." Transactions of the American Institute of Mining **135**: 416.

Kawamura, K. (1979). "The DSC Thermal Analysis of Crystallization Behavior in Palm Oil." 753.

Kellens, M., *et al.* (1991). "Synchrotron Radiation Investigations of the Polymorphic Transitions in Saturated Monoacid Triglycerides. Part 2: Polymorphism Study of a 50:50 Mixture of Tripalmitin and Tristearin During Crystallization and Melting." Chemistry and Physics of Lipids **58**: 145.

Kellens, M., *et al.* (1990). "Time Resolved X-Ray Diffraction Studies of the Polymorphic Behaviour of Tripalmitin Using Synchrotron Radiation." Chemistry and Physics of Lipids **52**: 79.

Kellens, M. and Reynaers, H. (1992). "Study of the Polymorphism of Saturated Triglycerides Ii: Polymorphic Behaviour of a 50/50 Mixture of Tripalmitin and Tristearin." Fat. Sci. Technol. **94**(8): 186.

Kolmogorov, A. M. (1937). "On the Statistical Theory of Metal Crystallization." Izv. Akad. Nauk. SSSR: 355.

Larson, R. G. (1999). "The Structure and Rheology of Complex Fluids." Oxford University Press.

Larsson, K. (1972). "Molecular Arrangement in Glycerides." Fette, Seifen, Anstrichmittel **73**(3): 136.

Larsson, K. (1992). "On the Structure of the Liquid State of Triglycerides." Journal of American Oil Chemists' Society **69**(no.8): 835.

Larsson, K. (1997). "Food Emulsions, 3rd Edition." S. Friberg and K. Larsson, Editors. Marcel Dekker, New York: 111.

Larsson, K. A. (1966). "Classification of Glyceride Crystal Forms." Chemica Scandinavia: 2255.

Lockett, T. J*., et al.* (1992). "The Stability of Inelastic Non-Newtonian Fluids in Couette Flow between Concentric Cylinders: A Finite-Element Study." Journal of Non-Newtonian Fluid Mechanics **43**: 165.

Lutton, E. S. (1948). "Triple Chain-Length Structures of Saturated Triglycerides." Journal of American Chemists' Society **70**: 248.

Lutton, E. S. (1950). "Review of the Polymorphism of Saturated Even Glycerides." Journal of American Oil Chemists' Society **27**: 276.

Lutton, E. S. and Fehl, A. J. (1970). "The Polymorphism of Odd and Even Saturated Single Acid Triglycerides, C8-C22." Lipids **5**(1): 90.

MacMillan, S. D*., et al.* (2002). "In Situ Small Angle X-Ray Scattering (SAXS) Studies of Polymorphism with the Associated Crystallization of Cocoa Butter Fat Using Shearing Conditions." Cryst Growth Des **2**: 221.

Maleky, F. and Marangoni, A. G. (2008). "Process Development for Continuous Crystallization of Fat under Laminar Shear." J Food Eng **89**: 399.

Mallock, A. (1888). "Determination of the Viscosity of Water." Proc. R. Soc. Lond. **A**(45): 126.

Mallock, A. (1896). "Experiments on Fluid Viscosity." Phil. Trans. R. Soc. Lond. **A**(187): 41.

Martini, S*., et al.* (2002). "Structure and Properties of Fat Crystal Networks." Advances in food and nutrition research **44**: 33.

Mazzanti, G. (2005). "Crystallization of Bulk Fats under Shear Chapter3."

Mazzanti, G*., et al.* (2003). "Orientation and Phase Transitions of Fat Crystals under Shear." Cryst Growth Des **3**(5): 721.

Mazzanti, G*., et al.* (2005). Crystallization of Bulk Fats under Shear. Soft Materials - Structure and Dynamics. J. R. Dutcher and A. G. Marangoni. N.Y., Marcel Dekker, Inc. **Chapter 3**.

Mazzanti, G*., et al.* (2005). "Modeling Phase Transitions During the Crystallization of a Multicomponent Fat under Shear." Physical Review E **71**.

Mazzanti, G*., et al.* (2008). "Modeling of a Two-Regime Crystallization in a Multicomponent Lipid System under Shear Flow." Eur. Phys. J. E **27**: 135.

Mazzanti, G*., et al.* (2008). "In Situ Rheo-NMR Measurements of Solid Fat Content." Journal of American Oil Chemists' Society **85**: 405.

Mazzanti, G*., et al.* (2007). "A Conceptual Model for Shear-Induced Phase Behavior in Crystallizing Cocoa Butter." Cryst Growth Des **7**(7): 1230.

Metin, S. (1998). "Thermal Analysis of Isothermal Crystallization Kinetics in Blends of Cocoa Butter with Milk Fat or Milkj Fat Fractions." Journal of American Oil Chemists' Society **75**(No.11): 1617.

Metin, S. and Hartel, R. W. (2005). "Crystallization of Fats and Oils." Bailey's Industrial Oil and Fat Products. F.B. Shahidi, Editor, Wiley Interscience, New York.

Metin, S. and Hartel, R. W. (2005). "Fat Crystallization Technology." Healthful Lipids. Oi-Ming Lai and Casimir C. Akoh, Editor. AOCS Publishing 2005 **Chapter 8**.

Minato, A*., et al.* (1997). "Thermal and Structural Properties of POP and OPO Binary Mixtures Examined with Synchrotron Radiation X-Ray Diffraction." Journal of American Oil Chemists' Society **74**: 1213.

Mooney, M. (1951). "The Viscosity of a Concentrated Suspension of Spherical Particles." Journal of colloid science **6**(2): 162.

Mudge, E. M. and Mazzanti, G. (2009). "Rheo-NMR Measurements of Cocoa Butter Crystallized under Shear Flow." Cryst Growth Des **9**(7): 3111.

Mullin, J. W. (1993). "Crystallization, 3rd Edition." Butterworth-Heineman Ltd., Oxford, U.K.: 172.

Mutaftschiev, B. (1993). "Nucleation Theory." In: Hurle, D.T.J., Editor, 1993. Handbook of crystal growth **1**.

Narine, S. S*., et al.* (2006). "Modification of the Avrami Model for Application to the Kinetics of the Melt Crystallization of Lipids." Journal of American Chemists' Society **83**: 913–921.

Narine, S. S. and Marangoni, A. G. (1999). "Relating Structure of Fat Crystal Networks to Mechanical Properties: A Review." Food Research International **32**: 227.

Okubo, T. and Ishiki, H. (1999). "Kinetic Analyses of Colloidal Crystallization in a Sinusoidal Electric Field as Studied by Reflection Spectroscopy." Journal of colloid and interface science **211**: 151.

Palberg, T*., et al.* (1995). "Grain Size Control in Polycrystalline Colloidal Solids." Journal of Chemical Physics **102**(no. 12): 5082.

Papir, Y. S. and Krieger, I. M. (1970). "Rheological Studies on Dispersions of Uniform Colloidal Spheres : Ii. Dispersions in Nonaqueous Media." Journal of Colloid and Interface Science **34**(1): 126.

Pascal, J. P. (1993). "Unsteady Rotating Shear Flow of Power Law Fluids." Mathl. Comput. Modelling **18**(9): 31.

Recktenwald, A*., et al.* (1993). "Taylor Vortex Formation in Axial through-Flow: Linear and Weakly Nonlinear Analysis " Physical Review E **48**: 4444.

ResonanceSystemsLtd. (2007). "Determination of Solid Fat Content (Sfc) in Oils and Fats by Spin Track Nmr Analyzer." Information Flyer (Food industry).

Rousset, P. (2002). "Modeling Crystallization Kinetics of Triglycerides." Physical properties of lipids. A.G. Marangoni, Narine, S.S., Editors, New York, Marcel Dekker Inc. .

Rowe, E. M. and Mills, F. E. (1973). "Tantalus L: A Dedicated Storage Ring Synchrotron Radiation Source." Particle Accelerators **4**: 211.

Saggin, R. and Coupland, J. N. (2004). "Shear and Longitudinal Ultrasonic Measurements of Solid Fat Dispersions." Journal of American Chemists' Society **81**: 27–32.

Saitô, H. (1986). "Conformation-Dependent 13c Chemical Shifts: A New Means of Conformational Characterization as Obtained by High-Resolution Solid -State 13C NMR." Magnetic Resonance in Chemistry **24**: 835.

Sato, K. (2001). "Crystallization Behavior of Fats and Lipids - a Review." Chemical Engineering Science **56**: 2255.

Sato, K. and Garti, N. (1988). "Crystallization and Polymorphism of Fats and Fatty Acids." Marcel Dekker Inc Pod.

Sato, K. and Ueno, S. (2005). "Polymorphism in Fat and Oils." Bailey's Industrial Oil and Fat Products. F.B. Shahidi, Editor, Wiley Interscience, New York.

Sato, K.*, et al.* (1999). "Molecular Interactions and Kinetic Properties of Fats." Prog. Lipid Res. **38**: 91.

Small, D. M. (1986). "The Physical Chemistry of Lipids: From Alkanes to Phospholipids." Plenum Press, New York: 345.

Sonwai, S. and Mackley, M. R. (2006). "The Effect of Shear on the Crystallization of Cocoa Butter." Journal of American Chemists' Society **83**: 583–596.

Takeuchi, M.*, et al.* (2002). "Binary Phase Behavior of 1,3-Distearoyl-2-Oleoyl-Sn-Glycerol (SOS) and 1,3-Distearoyl-2-Linoleoyl-Sn-Glycerol (SLS)." JAOCS **79**: 627–632.

Takeuchi, M.*, et al.* (2003). "Synchrotron Radiation SAXS/WAXS Study of Polymorph-Dependent Phase Behavior of Binary Mixtures of Saturated Monoacid Triacylglycerols." Cryst Growth Des **3**(3): 369.

Taylor, G. I. (1923). "Stability of a Viscous Liquid Contained between Two Rotating Cyliners." Philos. Trans. R. Soc. **London**(Ser. A, 223): 289.

Timms, R. E. (1995). "Developments in Oils and Fats." R. J. Hamilton, Editor, Chapman & Hall, Glasgow, U.K.: 204.

Todt, H.*, et al.* (2001). "Quality Control with Time-Domain NMR." European Journal of Lipid Science and Technology **103**(12): 835.

Todt, H.*, et al.* (2006). "Water/Moisture and Fat Analysis by Time-Domain NMR." Food Chemistry **96**(3): 436.

Toro-Vazquez, J. F.*, et al.* (2000). "Crystallization Kinetics of Palm Stearin in Blends with Sesame Seed Oil." Journal of American Oil Chemists' Society **77**(no. 3): 297.

Toro-Vazquez, J. F.*, et al.* (2002). "The Avrami Index and the Fractal Dimension in Vegetable Oil Crystallization." Journal of American Oil Chemists' Society **79**(9): 855.

Toro-Vazquez, J. F.*, et al.* (2004). "Rheometry and Polymorphism of Cocoa Butter During Crystallization under Static and Stirring Conditions." Journal of the American Oil Chemists Society **81**(2): 195.

Ueno, S.*, et al.* (1997). "Synchrotron Radiation X-Ray Diffraction Study of Liquid Crystal Formation and Polymorphic Crystallization of SOS (Sn-1,3-Distearoyl-2-Oleoyl Glycerol)." Physical Chemistry B **101**: 6847.

Unruh, T.*, et al.* (2002). "Self-Assembly of Triglyceride Nanocrystals in Suspension." Langmuir **18**: 1796.

VanPutte, K. and Enden, J. V. D. (1974). "Fully Automated Determination of Solid Fat Content by Pulsed Nmr." Journal of American Oil Chemists' Society **51**(7): 316.

Walstra, P. (1987). "Food Structure and Behaviour." J.M. Blanshard and P. Lillford, Editors, Academic Press, Orlando, Florida: 67.

Walton, A. G. (1969). "Nucleation in Liquids and Solutions." A.C.Zettlemoyer Editor, Nucleation, Marcel Dekker, New York: 225.

Wildemuth, C. R. and Williams, M. C. (1984). "Viscosity of Suspensions Modeled with a Shear-Dependent Maximum Packing Fraction." Rheol. Acta **23**: 627.

Wille, R. L. and Lutton, E. S. (1966). "Polymorphism of Cocoa Butter." Journal of the American Oil Chemists Society **43**(8): 491.

Woods, M. E. and Krieger, I. M. (1970). "Rheological Studies on Dispersions of Uniform Colloidal Spheres I. Aqueous Dispersions in Steady Shear Flow." Journal of colloid and interface science **34**(1): 91.

Wright, A. J.*, et al.* (2000). "The Effect of Minor Components on Milk Fat Crystallization." JAOCS **77**: 463–475.

APPENDICES

Appendix A. Rheo-NMR System Signal Fittings and Calibrations

10.1. Gaussian Function Fitting of the Free Induction Decay Signals from NMR

The relaxation signal after a 90° pulse is well fitted by Gaussian function, which has been used to fit the proton free induction decays of fat samples. The liquid signal has been fitted by a Gaussian function to find the background, which is the offset value in the Eq. (25). The values of LS and SS in this equation were obtained from the Gaussian fitting of the solid signal.

10.2. Rheo-NMR Calibration Details

10.2.1. Attenuation (ATT) Value Determination

The very weak NMR radio frequency signals from the sample must be greatly amplified first and then an attenuator reduces the signal strength. The ATT value defines the attenuation level for the signal input. An analog-to-digital converter (ADC) in the NMR device translates the NMR signal into a voltage level that changes with time. Since the ADC can convert voltages from about -5 volts up to +5 volts, to get a reasonable voltage value, the attenuation parameter must be adjusted so that the signal is not too strong for the ADC or so weak that the ADC cannot provide meaningful output to the microprocessor. The amount of attenuation required depends on how strong the original signal is: stronger signals require more attenuation. If the attenuator value is set too low, the final signal amplitude will be too large and will exceed the range of the ADC, which will cause a “CLIP” error during the measurement. On the other hand, if the attenuator is set too high, the signal amplitude will be reduced more than is necessary, in which case that the validity of the data will be reduced. Hence, a calibration of its effect was needed

since there was a possibility that the attenuation value need to be adjusted due to the variable signal strengths between experiments and samples.

Several tests were performed with a sample of pure triolein in the tube and the temperature control system on. The Galden fluid running through the device was kept at constant temperature for the duration of each set of measurements. Over 100 NMR FID curves were captured for each point.

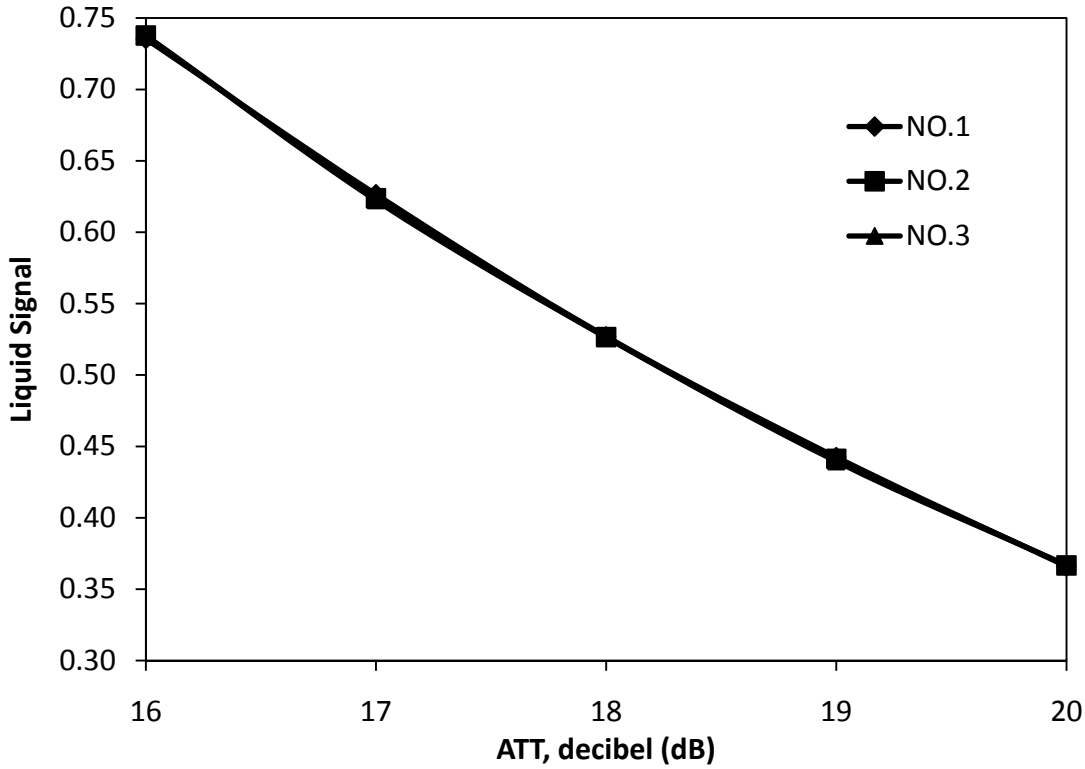

Figure 10-1 Calibration test to find the proper ATT value with a sample of triolein. No.1, No. 2, and No. 3 represent experiments in the triplicate.

When ATT value was set as 15, the device suffered from a "clip" error, which means the voltage is over the maximum value. When ATT value was 16, the average voltage value was about 4V, which is a good signal value range. After that, the increasing ATT values reduce the liquid signal from the sample. This series of tests were repeated 3 times with very similar results. Hence, the ATT value 16 was chosen to use in all the experiments of this work.

The ATT value normally is about 30 for our NMR instrument operated with a 13 mm tube sample completely filled. However, the NMR signals (solid and liquid) are reduced

dramatically in our rheo-NMR system, because of several facts: a) the shaft of the rheometer placed in the middle of the sample decreases the amount of sample occupied; b) The glass of the 10 mm tube and the Galden Fluid surrounding this sample tube occupy space that would otherwise be filled with sample providing NMR signal; c). The RF coil of the probe was designed for a 13mm tube, but a 10 mm sample tube was used so the temperature control system could be built in. The signal received from the protons closer to the coil is stronger than that from the core, thus these modifications further reduced the intensity. Since NMR signals are weaker, the signal to noise ratio increased. As calculated earlier in section 3.4.1.2., NMR signals of the samples in this research are only about one third comparing to a normal case. Therefore, the ATT values chosen in our work needed to be much lower than those at typical operation. This situation is not ideal, but it is worth sacrificing the time and signal resolution for the temperature control and the shear introduced into this research.

10.2.2.Best Position for Sample Tube

Bruker PC/20 NMR was designed as a convenient sample measuring device in which simply introducing the sample tube into the electromagnetic field would trigger the instrument and produce a reading on its display. The position where the tube is located in the field affects the signal strength because of the amount of sample in that field, and the coil location. For the NMR device itself, there is a sample injection hole fit perfectly for the 10mm sample tube. Hence, the horizontal position of the system is fixed once the sample tube is centered from the injection hole. However, the vertical position of the sample tube can make a big difference of the strength of sample signals. In the un-modified probe the depth was adjusted with a Teflon screw at the bottom. In our system, to get the strongest signal for better and easier analysis, a test was executed to find the best sample location.

The sample was put into a 10mm of glass tube for the NMR measurement. The amount of sample was about 1.7mL which gives a height about 4.5cm (with the shaft of the measuring head inside) in the tube. Edible canola oil was used for the position calibration.

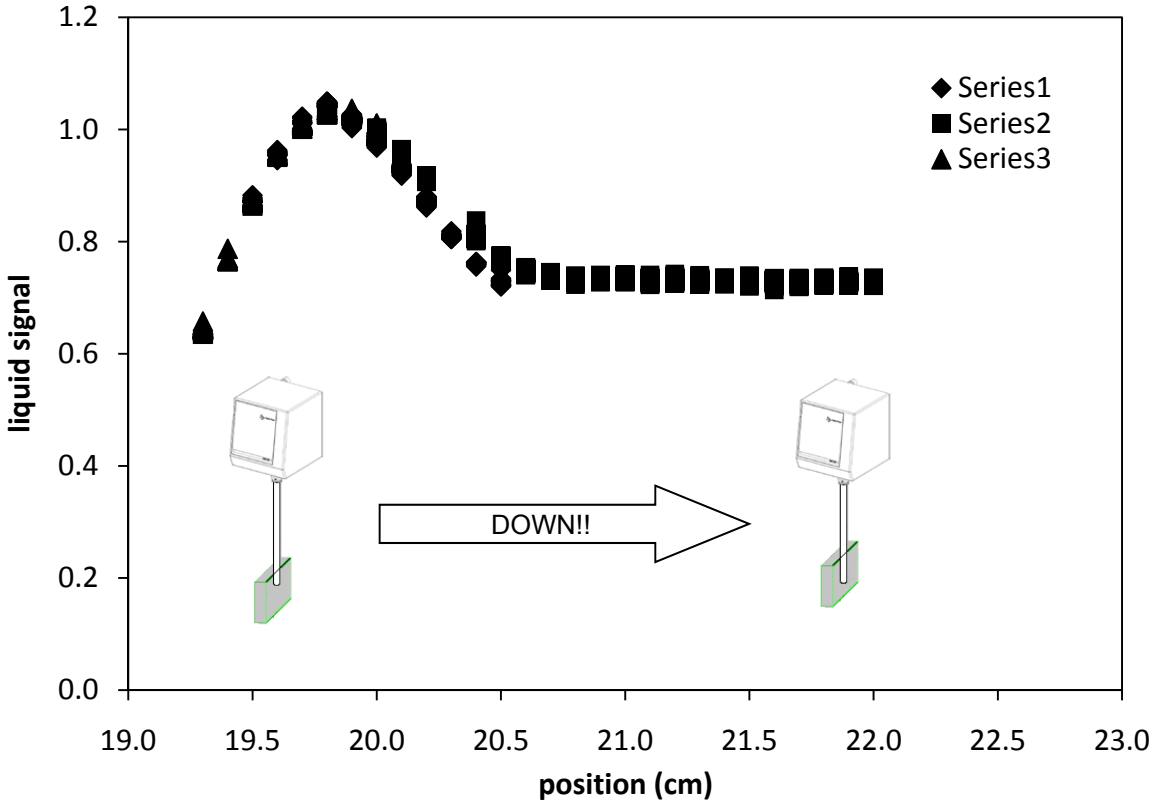

Figure 10-2 Calibration test to find the best sample position with a sample of canola oil. Series 1, 2, and 3 represent three parallel experiments which show a high reproduction estimating the same best position for the sample at 19.8cm. X axis is the position of the measuring head with sample tube connected at the bottom from marked "0" position on the 2-dimension motion stage down to 19.0–23.0 cm below.

From Figure 10-2, the liquid signal of the sample reached its maximum value at the position 19.8cm down from the "0" position. This was the best position found, which was kept for all the experiments performed.

10.2.3.Temperature vs. Signal

Finding the relation between the signal strength and temperature is crucial for the development of a calibration of NMR signal versus temperature. Canola oil was used as the sample for the test. NMR signal was recorded every 2s for 5 minutes at each temperature from 10 to 70°C at intervals of 10°C. This range (10 to 70°C) was chosen because it was the same as

the experimental one. This test was performed using the system with the shaft of the rheometer without any shearing involved. The calibration test was repeated 3 times for precision.

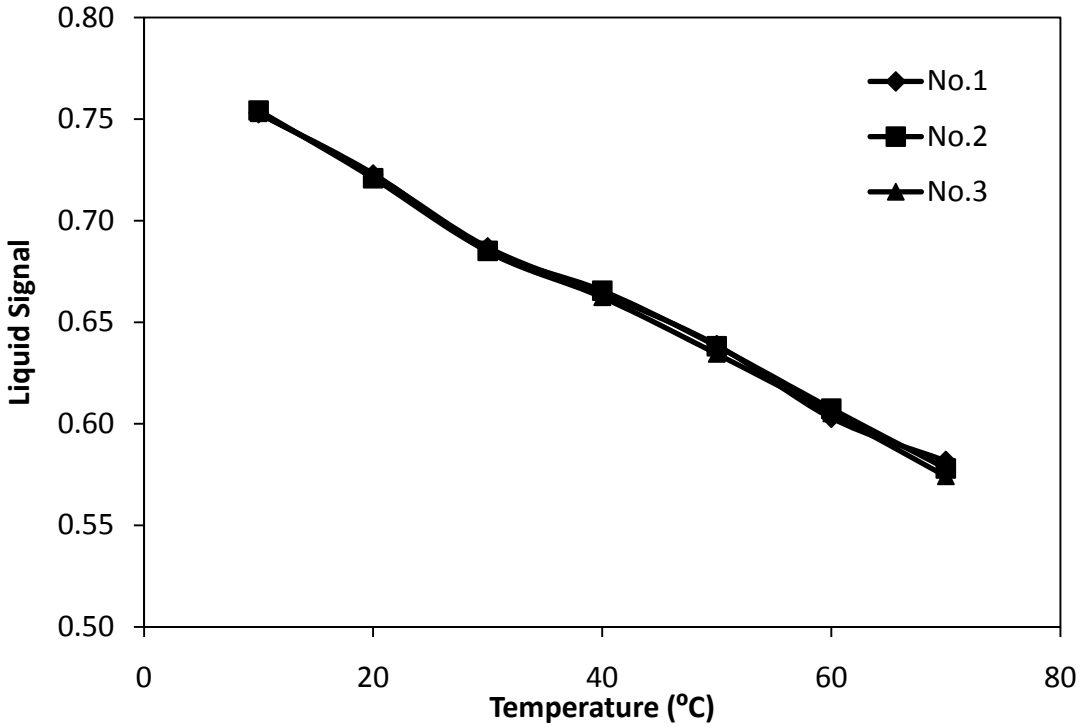

Figure 10-3 Calibration test to find the temperature effect on the intensity of liquid signal with a sample of canola oil. No. 1, 2, and 3 represent three parallel experiments which show the same pattern.

The liquid signal (LS) was obtained by averaging liquid values between 70 and 100 microseconds for each measurement, which lasts 2 seconds. The data were collected for 5 minutes, so 150 points were averaged. LS reduces from 0.75 to 0.57 as the temperature increases from 10°C and 70°C as seen from Figure 10-3. The explanation for this can be twofold. Firstly, it can be that the density of the sample decreases due to the temperature increasing causing less detectable protons existing in a fixed volume of sample. It can also be explained as the partition of the protons change. When the temperature increases, the partition coefficients of the unbalanced protons will become smaller meaning that less signal will be detected. These two effects combine together, causing the liquid signal of the sample to decrease as temperature increases.

10.2.4.Thermo Devices Calibration

A thermistor and a fiber optic temperature sensor (FOT) were used as the temperature measuring devices in the Rheo-NMR system. The thermistor was located at the center of the canola oil sample in the 10mm tube while the fiber optic temperature sensor was placed at the bottom of the sample holder to measure the temperature of the sample. Both of the devices were read and recorded by the LabVIEW software. However, regardless of the precision of the devices themselves, temperature readings are slightly different due to their characteristic. For a better understanding of the disagreement of temperature readings caused by the difference between the two devices, another calibration test was performed as putting both of the devices at a certain temperature and keeping recording the reading from them. The set point values were the temperatures inputted to the LabVIEW software which commands the controller, which in turn delivered the necessary power to the active theat exchanger. The fiber optic temperature sensor was used as the device to measure the temperature. The LabVIEW program also recorded the readings from the thermistor device placed next to the fiber optic. The plot below showed the fiber optic temperature sensor and the thermistor temperature readings. There was a slight difference between the readings.

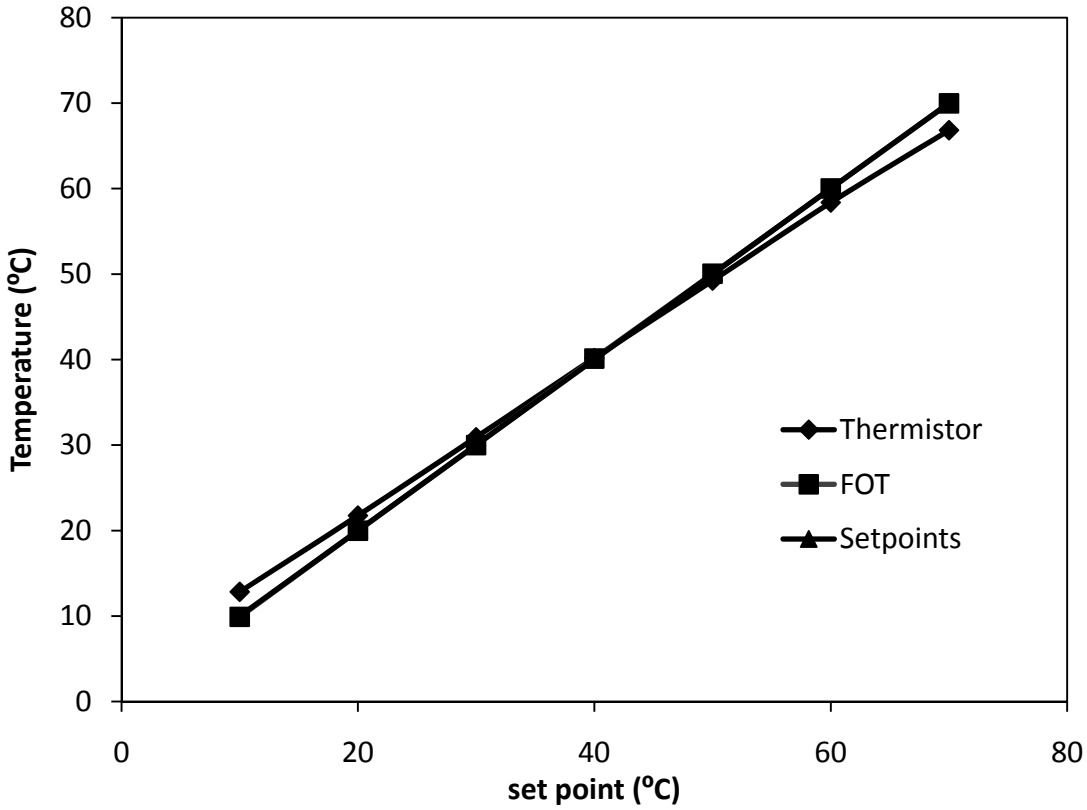

Figure 10-4 Calibration of the two temperature reading devices, the thermistor and the fiber optic temperature sensor, with the set points of temperature.

Another plot was used to estimate the relationship between the temperature readings from the thermistor and the ones from the fiber optic temperature sensor.

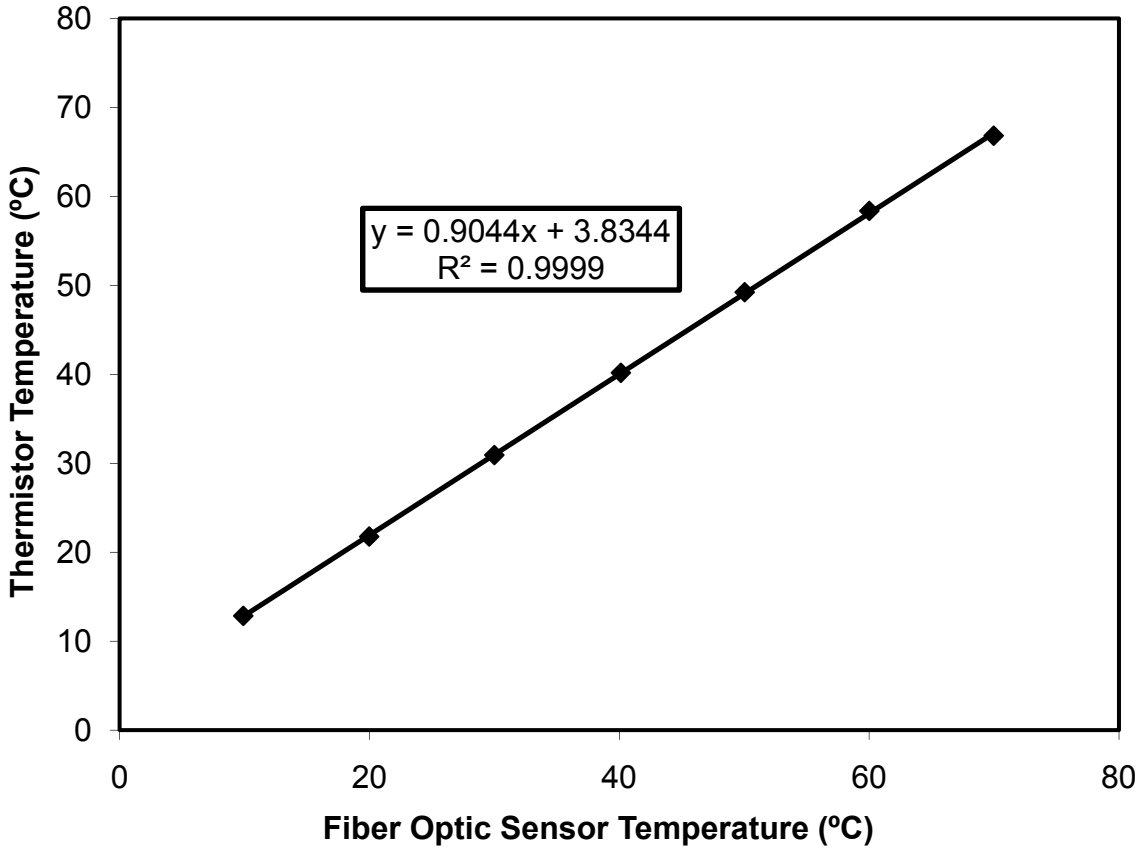

Figure 10-5 The temperature reading relation between the thermistor and the fiber optic temperature sensor.

These measurements are averages of 1000 points taken every 1 second from both the sensors.

Appendix B. Methodology for Data Analysis of the XRD Measurement

10.3. BNL SMART Software for Data Collection

From the 2D CCD camera located in the X-ray beam hutch, the X-ray Diffraction patterns collected as image data were recorded by the Bruker-Siemens (BNLWebsite) SMART software from the BNL control computer. This software was able to command the detector camera collecting data and save them as BS (Bruker-Siemens) images at certain time interval, which was 63 seconds in our case.

10.4. ImageJ Plug-in for XRD Image Analysis

ImageJ software was designed with an open architecture that provides extensibility via Java plug-ins. It is a public domain, Java-based image processing program developed by Wayne Rasband as the core author at the National Institutes of Health of the United States. Plug-ins can add support for new file formats or they can filter or analyze images. The XR2D plug-in for ImageJ was developed by Maochen Hannah Wang, Gianfranco Mazzanti and Kisun Park, and later modified by Gianfranco Mazzanti. It was used to open the BS images for further analysis, including opening, filtering, and centering images, etc.

10.4.1.Opening the Images

The BS images corresponding to the crystallization sequence for each cycle were placed in single folders. The XR2D plug-in could open the images in one same folder as a stack (a series of images that share a single window) of 16-bit grey-scale images of size 512 × 512 pixels, which can be browsed using a scroll bar. The horizontal and vertical directions of an image defined the x and y axis, and the pixels located by the coordinates were named from (0, 0) (the top left corner of an image) to (512, 512) (the bottom right corner).

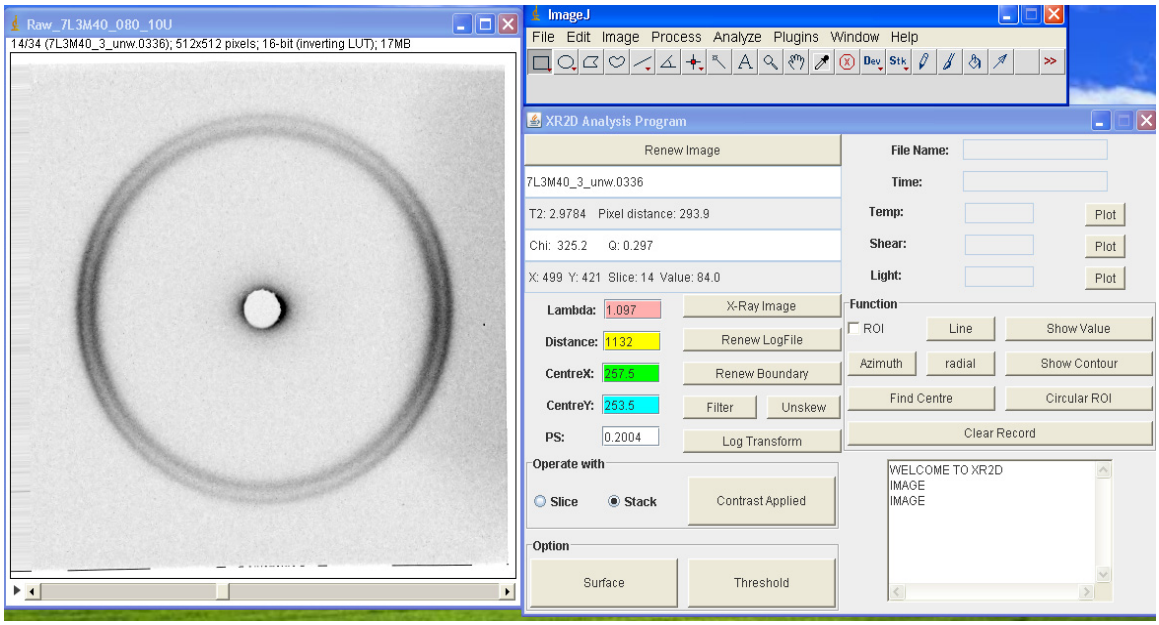

Figure 10-6 User interface for the XR2D plug-in for ImageJ displaying a stack of images corresponding to SAXD of 7L3M40 at $80s^{-1}$.

10.4.2.Filtering the Images

The image stack was filtered using a macro developed to remove 'bad pixels' which were the abnormal pixels appearing in every single image due to imperfections in the detector. These bad pixels were first picked by checking every stack of images and located them manually by the coordinates, and then recorded them into a list, which the macro created used. After running the macro, the abnormal pixels on the list were replaced by the average value of the 8 pixels around it. The real value of that pixel should not be a huge difference from the average value of its neighbours.

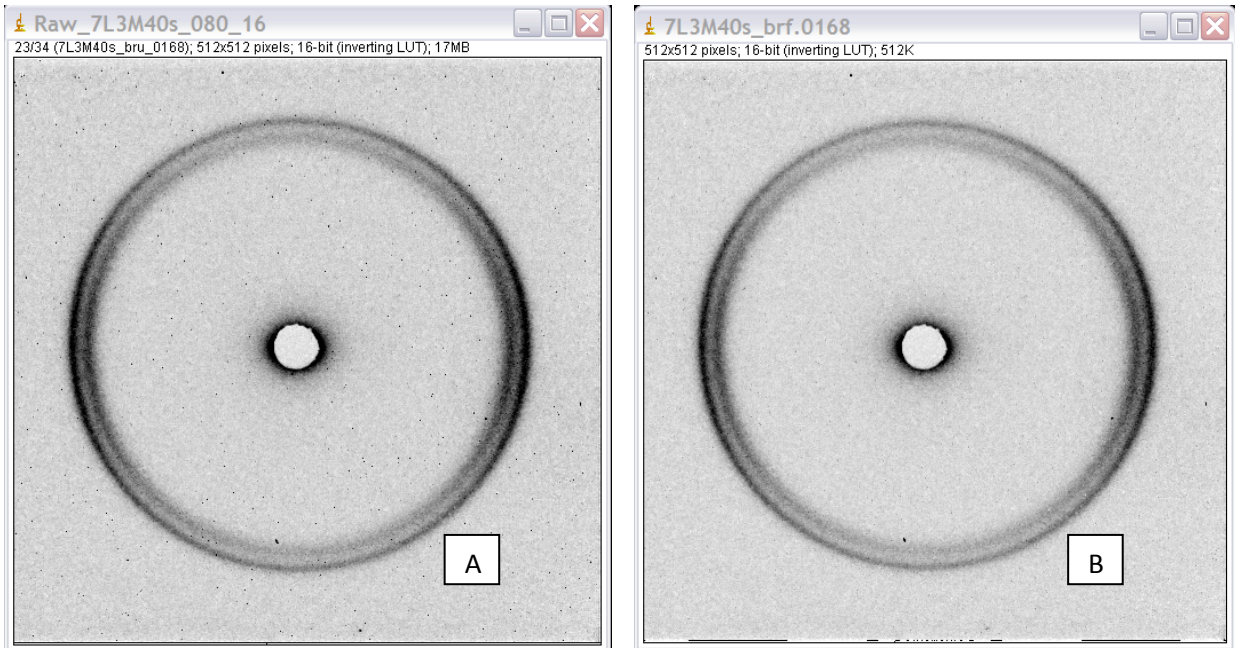

Figure 10-7 Raw scatter ring image (A) and filtered scatter ring image (B) example (SAXD of 7L3M40 at $80s^{-1}$).

10.4.3.Unwarping the Images

The SMART software was called by the ImageJ plug-in by the unwarping process macro developed by Dr. Gianfranco Mazzanti. The macro activated through the ImageJ interface could bring up SMART software to unwarp the filtered images and save them into the commanded directory. After filtering and unwarping, the image files were ready for further analysis.

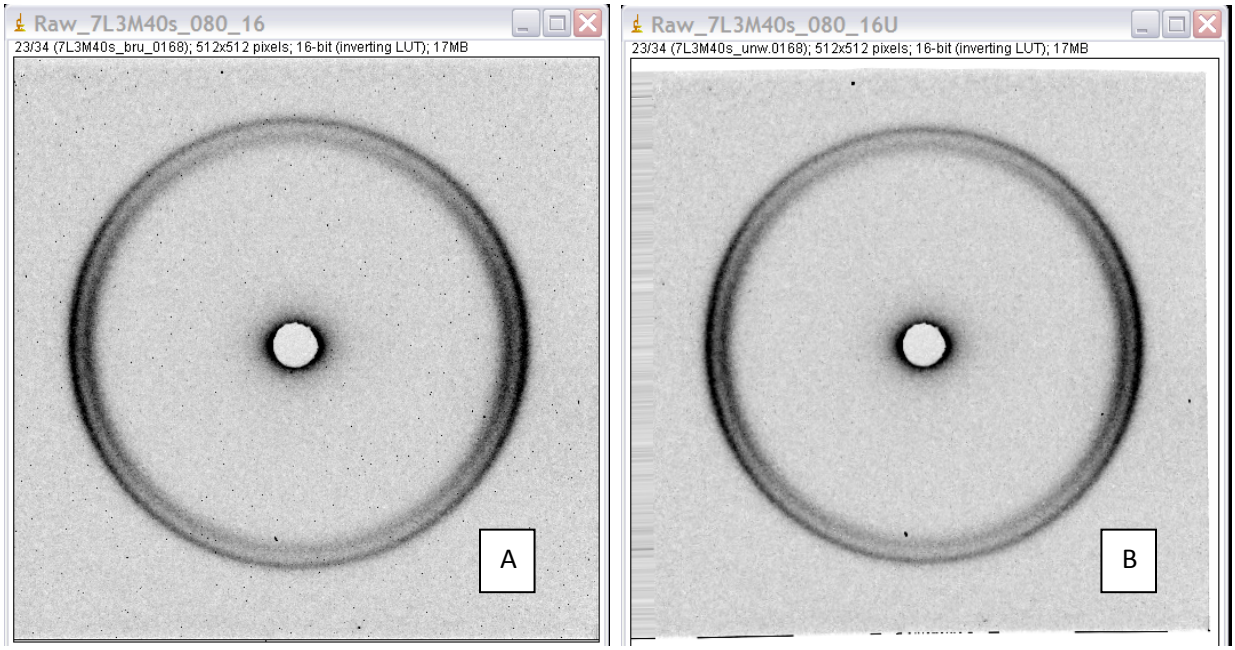

Figure 10-8 Raw scatter ring image (A) and unwarped scatter ring image (B) example (SAXD of 7L3M40 at $80s^{-1}$).

10.4.4.Centering the Images

The unwarped images normally had a damaged edge area creating noise with no valuable data included. A boundary was set to cut all the four edges and keep the center area untouched before centering the image. It was to ensure the exclusion of noise in the averaging process from the noise outside the specified boundary during the unwarping process.

The XRD patterns obtained from the experiments were almost circular so the centering process could be easily done. A range of radii in q values (starting and ending) was provided which included an approximate scattering circle inside. The plug-in XR2D has a function for searching the maximum intensity ring inside the given range and find the center of the ring based on that. The centering process was repeated 3 times for each stack of images to obtain accurate measurements.

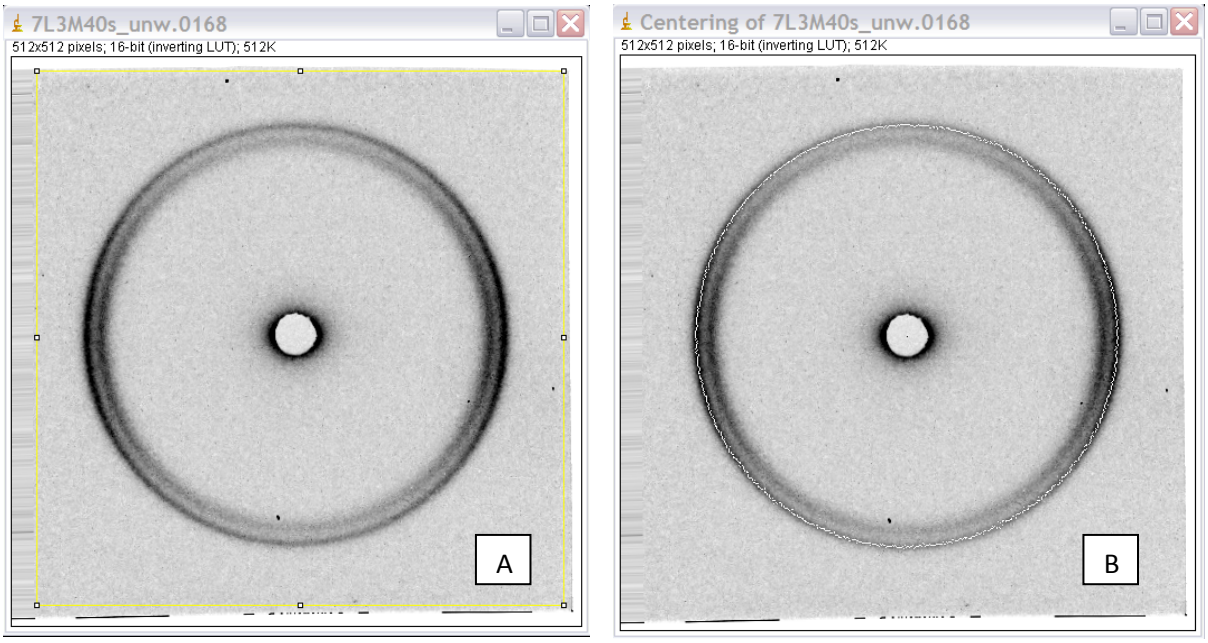

Figure 10-9 Scatter ring image with boundary renewal (A) and centered scatter ring image (B) (SAXD of 7L3M40 at $80s^{-1}$).

10.4.5.Creating the Radial and Azimuth Plot

Radial plot and azimuth plot were created after the images were centered. A Radial plot (Metin, 1998) is formed by integrated intensities around concentric rings as a function of distance from its center. The integrated intensity was defined as the sum of pixel values around a ring at any given distance from the center. By inputting the start and end radii in q values after clicking the "radial" button on the XR2D control panel, the RP profiles, which are plots of the scattering vector q versus the scattering intensity, can be created for all images in a stack and display them together. The RP profile was saved as a text image for further analysis. It provides information on the peak position, area, X-ray scattering intensity, full width half maximum (FWHM) and provides a time sequence for studying the kinetics of the process.

The azimuth profile records the intensity along the scattering ring as a function of the scattering angle and shows the degree of orientation of crystallites. Using the "azimuth" button on the XR2D control panel, an azimuth profile was created by specifying the initial angle and arc angular length as well as the width in pixels to average. The obtained AP file was saved as a text image.

10.4.6.Creating the log File

The log (MacMillan, *et al.*, 2002) file contains time, temperature, and the monitor values of beam intensity exactly corresponded to the scattering image information. They were recorded during all the experiments by the computer at NSLS as text files. After separating the LG files into text files correspond to each experiment cycle, they were saved as tab delimited text files.

10.4.7.Normalizing the Radial and Azimuth Plot

The incident beam intensity was monitored and recorded as 'monitor values' by a scintillation detector which was placed before the X-ray beam reached the second set of slits. The value deceases after every beam refill. The monitor information was recorded as a part of variables in the log files.

Normalized radial plot (NRP) was created from the RP and LG file using a macro developed for ImageJ, and normalized azimuth plot (NAP) was created from the AP and LG file. This activated macro shows four buttons N, S, T and P. N, the normalization tool, normalizes the text; T, the text image tool, opens a text image; S, the stack radial tool, opens the text image and creates the stack of radial plots (no normalization) and P, the NRP stack tool, opens an NRP text image and creates a stack with temperatures. To normalize the RP and AP data, the macro divides the multiple sets of data by a common variable to allow for data comparison.

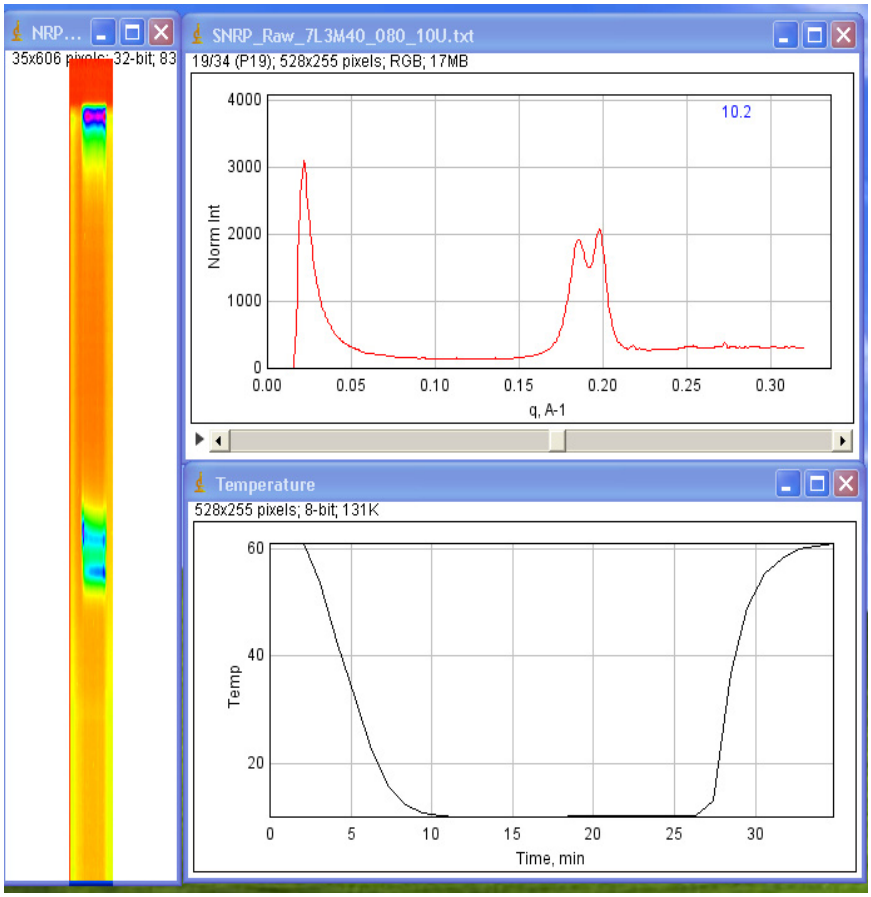

Figure 10-10 NRP, SNRP image stack and temperature as a function of time corresponding to SAXD of 7L3M40 at 80s^{-1}**.**

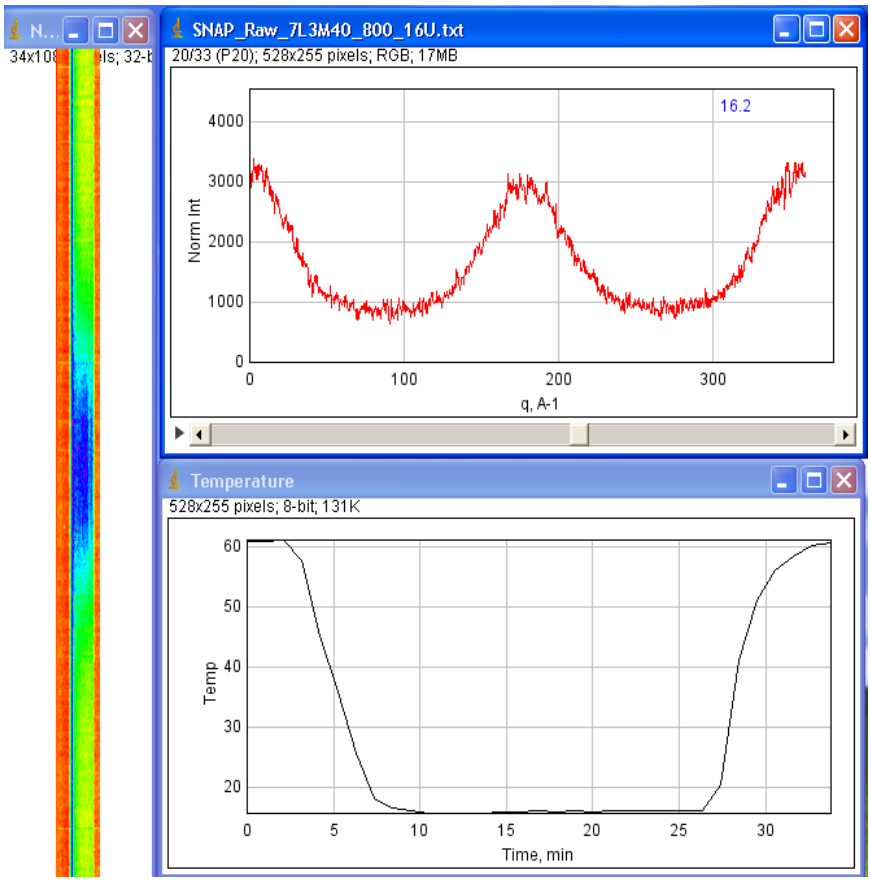

Figure 10-11 NAP, SNAP image stack and temperature as a function of time corresponding to SAXD of 7L3M40 at $80s^{-1}$**.**

10.5.Igor Pro 6.0 for Peak Fitting

Igor Pro 6.0 is a scientific data analysis software package produced by Wavemetrics Inc., for curve fitting and peak fitting. The software program operates using the Levenberg-Marquardt Algorithm (LMA), which is an iterative technique that locates the minimum of a multivariate function that is expressed as the sum of squares of non-linear real-valued functions. LMA can be thought of as a combination of steepest descent and the Gauss-Newton Algorithm (GNA). The LMA is more robust than the GNA, which means that it finds a solution even if it starts very far off the final minimum. On the other hand, the LMA tends to be slower than the GNA for well-behaved functions and reasonable starting parameters. The LMA is a very popular curve-fitting

algorithm used in many software applications for solving generic curve-fitting problems (Igor Pro Manual).

The domains of fat crystals scatter light to product peaks, which represent the number of crystal arrangements present. In this analysis, it is assumed that each peak corresponds to a particular phase characterized by a given polymorphic form and composition. In most of the experiments, more than 3 different types of phases were observed. The largest conceptual problem, however, is peak overlapping. If the complete peak is not separated, the only possible solution is to try to reconstruct the original peaks from the blended result. This requires some assumption on the peak-profile shape, which introduces bias into the method.

Igor Pro 6.0 software was chosen because of its ability to separate and quantify hidden peaks that standard instrumentation would miss. In the literature is not unusual to find composite peaks reported as single peaks (Takeuchi, *et al.*, 2002, 2003). Fitting the multiple peaks involved fitting the data to a function that was a sum of functions. Each function represented one peak. The NRP files created by the ImageJ plug-in program contained all the multiple peaks information and were loaded to the Igro Pro peak fitting program for further analysis.

10.5.1.Baseline Calibration

There are three different baseline options provided by the Igor Pro 6.0 peak fitting program: constant, linear, and cubic. The background can be any function that represents the shape of the trend the peaks are sitting on. Hence, the peak fitting will not be accurate unless the background is accounted for. It is known that the slow-varying background is much more complicated than a constant one, linear and cubic background calibration was tested and the linear one was finally determined because there was no significant difference between the errors from each background. Moreover, the linear function was easier for the peak fitting program to operate.

10.5.2.Types of Function (Voigt, Gaussian, Lorentzian)

All normalized line profiles can be considered as probability distributions. A Gaussian profile is equivalent to a Gaussian or normal distribution and a Lorentzian profile is equivalent to

a Lorenz (or Cauchy) distribution. Without loss of generality, only centered profiles which peak at zero are need to be considered.

The centered Gaussian distribution with a characteristic bell shape is defined by two parameters: the frequency from line center (x) and variance (σ^2), expressed as:

$$G(x;\sigma) = \frac{e^{-x^2/(2\sigma^2)}}{\sigma\sqrt{2\pi}} \tag{39}$$

The Lorentzian distribution is a continuous probability distribution symmetric with a width characterized by its full width at half maximum (γ). The centered Lorentzian probability function is defined as:

$$L(x;\gamma) = \frac{\gamma}{\pi(x^2 + y^2)} \tag{40}$$

The Voigt profile is a convolution of a Lorentz and a Gaussian profile. The Voigt profile can be expressed as:

$$V(x;\sigma,\gamma) = \int_{-\infty}^{\infty} G(x';\sigma)L(x - x';\gamma)dx' \tag{41}$$

The defining integral can be evaluated as:

$$V(x;\sigma,\gamma) = \frac{Re[\omega(z)]}{\sigma\sqrt{2\pi}} \tag{42}$$

where $Re[\omega(z)]$ is the real part of the complex error function of z and $z = \frac{x+i\gamma}{\sigma\sqrt{2}}$.

The observed X-ray diffraction profiles cannot be well represented with a simple Lorentz or Gauss function (Klug and Alexander 1974; Young and Wiles 1982). Experience shows that the Voigt function fits very well the peak profiles in X-ray diffraction cases (Wertheim, *et al.* 1974; Hall, *et al.* 1977).

10.5.3.Multi-peak Fit Procedure

In Igor, the NRP files were loaded as “waves” which were sets of text or numeric values. Individual values within a wave were referred to as points. The waves were later renamed to “rp_number” (eg. rp_1, rp_2, etc.) and displayed in a table. SAXD image included information

from q value 0 to 0.32 Å. The information was plotted as a function of q value and normalized intensity as shown in Figure 10-12:

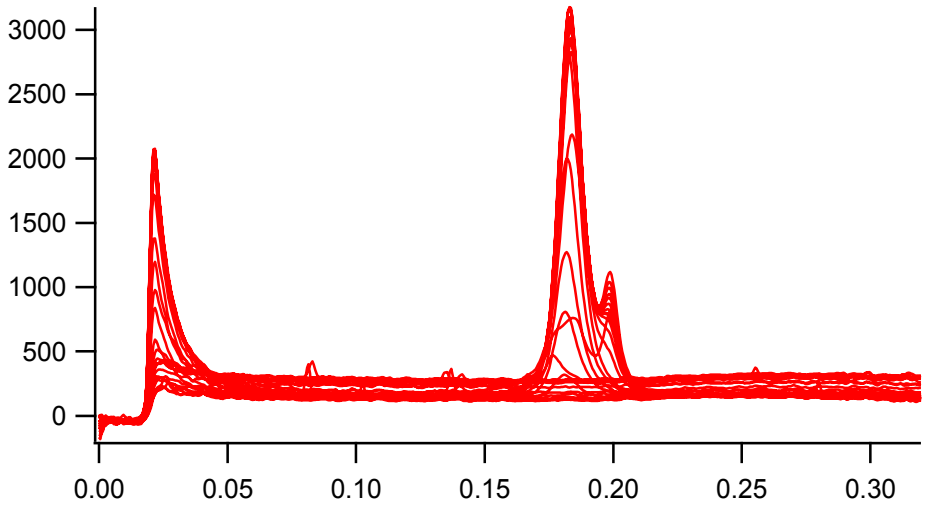

Figure 10-12 NRP file plot of normalized intensity as a function of ***q*** value to SAXD of 7L3M40 at 16°C at shear rate $80s^{-1}$.

The two main peak areas were the scattering rings observed at the center (0.02-0.04Å) and in small angle scatter area (0.17-0.22Å). The scattering ring at the center is due to diffuse scattering from the contrast between the solid particles and the liquid. It is not Bragg diffraction from a crystalline lattice. Though it contains some information on the size and shape distribution of the crystals, it was not the target of this study, and thus was mostly obscured by the beam stop. The small angle area, on the other hand, included the peaks produced by the Bragg scattering coming from within the nanostructures of the crystals. To focus on working at the small angle range, a q value range from 0.14 to 0.22Å was kept while the other part of the curves was chopped. The graph contained each diffraction pattern as one curve for an experiment cycle, which had the liquid background from the melt as seen as the curves without peaks in the graph. Our research objective was the fat crystal characterization during the crystallization process. Thus, the peak fitting analysis started from the curve that had the first crystal (peak) observed (solid black curve marked in Figure 10-13) and went on to the one that had the last crystal evidence (solid grey curve marked in Figure 10-13).

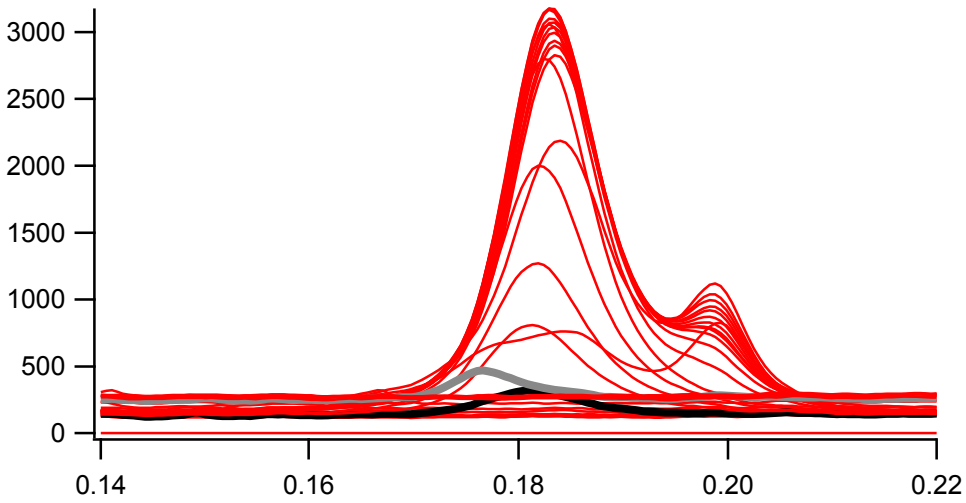

Figure 10-13 NRP file plot of normalized intensity as a function of certain $\boldsymbol{q}$ value range (0.14-0.22Å) to SAXD of 7L3M40 at 16°C, shear rate $80s^{-1}$. The black curve was the first crystal observed curve and the grey one was the last one.

Multi-peak Fit, part of Igor Pro, has a function named "auto locate peaks" which can automatically locate any positive positioned peak in one curve file. However, the type of baseline needed to be set as "liner" manually, and also the type of each peak. All the peaks started with the type of Voigt. The Multi-peak Fit program executed the peak fitting by minimizing the error with fixed baseline and peak types.

Peak results reported several parameters as peak location, amplitude, area, and FWHM. Further analysis was performed in Microsoft Office Excel for parameters obtained from Igor Pro Multi-peak Fit.

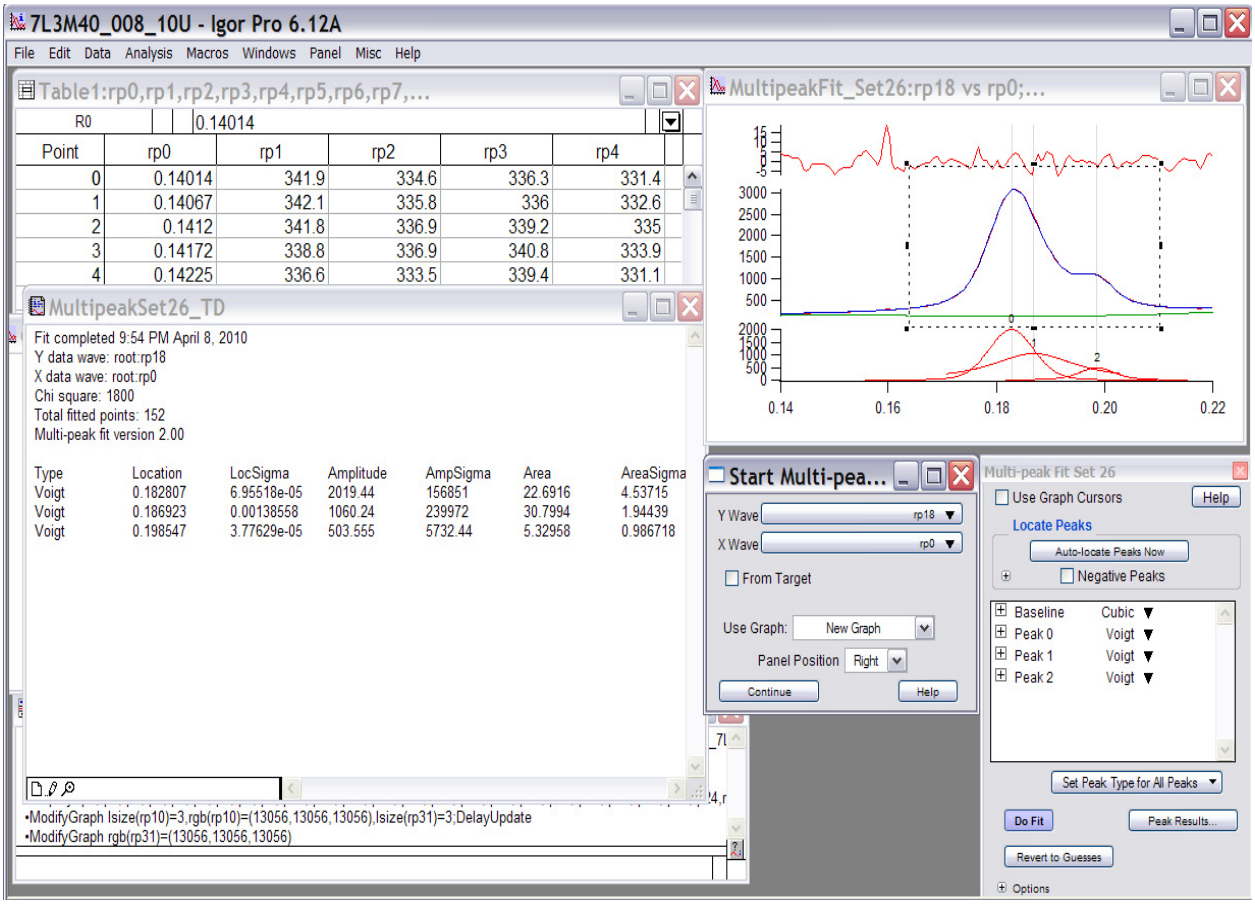

Figure 10-14 User interface for Igor Pro Multi-peak fit displaying a curve plot corresponding to SAXD of 7L3M40 at 8s $^{-1}$ at 14ºC.

Appendix C. Calculation of the K_σ Factor of the Rheometer

K_σ is the conversion factor between torque and shear stress calculated by the Rheoplus software based on the geometrical configuration of the experimental system like the type of sample tube, the amount of sample, etc.

In the software RheoPlus, there is a setup option "change measuring system" as shown in Figure 10-15. Several parameters are required by the system to calculate the C_{ss} and C_{sr} values, such as Length Cylinder Part, Radius Ra, and Radius Rt.

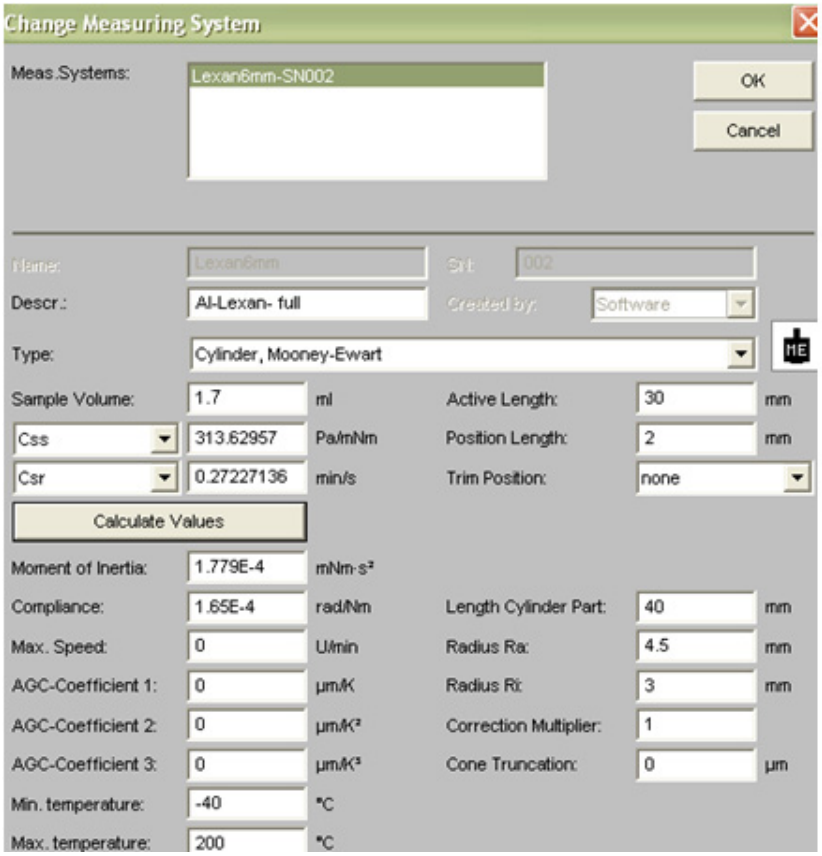

Figure 10-15 User interface for Rheoplus "Changing Measuring System" displaying the calculation parameters.

10.6. Calculation of the Torque for the Cylinder Part

It has been given that $R = 0.0045\text{m}$, radius of the sample tube (cylinder); $r = 0.003\text{m}$, radius of the shaft. The amount of sample is 1.7 mL, angle of the cone part of the shaft α is 45°, the gap between the bottom of the tube and the bottom of the shaft δ_0 is 0.002m. The height of the sample in the cylinder is 0.045m from the bottom and 0.04m from the top of the cone part of the shaft.

If the torque was calculated only by considering the cylinder part of the shaft, then:

$$\sigma = \frac{F}{A} = \frac{\tau}{r} \cdot \frac{1}{A} = \frac{\tau}{2\pi r^2 h} \tag{43}$$

$$\frac{1}{2\pi r^2 h} = \frac{1}{2 \cdot \pi \cdot 0.003^2 \cdot 0.04 \cdot 1000} = 442.097\left(\frac{Pa}{mNm}\right) \tag{44}$$

where τ is torque, σ is shear stress, $r = 0.003\text{m}$ (the radius of the shaft), and $h = 0.04\text{m}$ (the length of the cylinder part).

10.7. Calculation of the Torque for the Cone Part

However, in this work, the real torque should be measured as the sum of the torque from the cylinder part of the shaft and the cone part of the shaft. The cone part of the shaft is more complicated than the cylinder part.

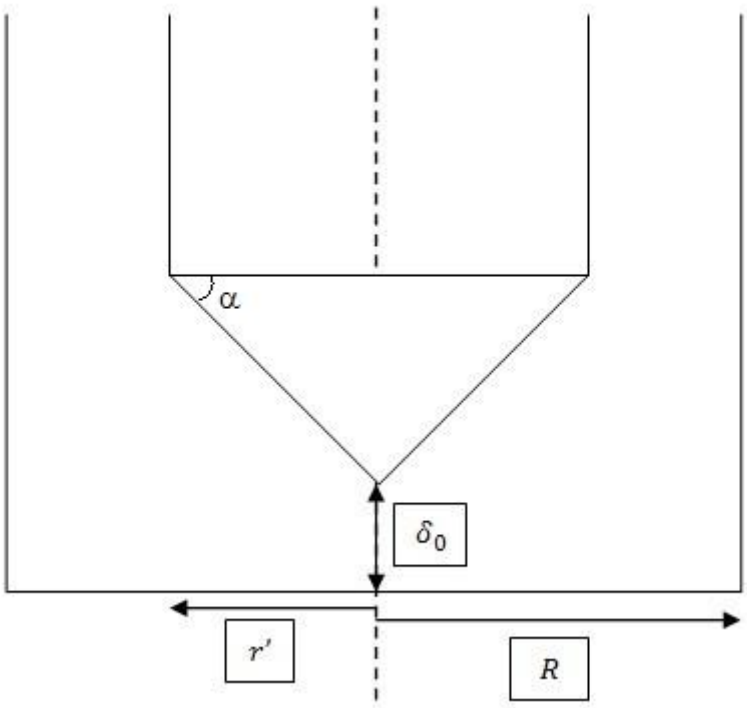

Figure 10-16 Diagram of the bottom part of the sample tube with the rheometer shaft in it.

$$\alpha = 45°, \therefore \delta = \delta_0 + r \tag{45}$$

$$\dot{\gamma} = \frac{v}{\delta} = \frac{\omega \cdot r'}{\delta_0 + r'} \tag{46}$$

$$\sigma = \mu \cdot \dot{\gamma} = \mu \cdot \frac{\omega \cdot r'}{\delta_0 + r'} = \frac{F}{A} \tag{47}$$

$$A = \pi r\sqrt{r^2 + h^2} = \sqrt{2}\pi r^2 \tag{48}$$

$$\therefore \mu \cdot \frac{\omega \cdot r'}{\delta_0 + r'} = \frac{F}{\sqrt{2}\pi r^2} = \frac{\tau_{cone}}{r'} \cdot \frac{1}{\sqrt{2}\pi r^2} \tag{49}$$

Calculate the average value when $r' = r/2$,

$$\mu \cdot \frac{\omega \cdot r/2}{\delta_0 + r/2} = \frac{F}{\sqrt{2}\pi r^2} = \frac{\tau_{cone}}{r/2} \cdot \frac{1}{\sqrt{2}\pi r^2} \tag{48}$$

$$\tau_{cone} = \frac{\sqrt{2}\pi\mu \cdot \omega r^4}{4\delta_0 + 2r} \tag{49}$$

10.8.Find the Kσ Value

The cylinder part:

$$\tau_{cylinder} = \tau \cdot A \cdot r = \mu \cdot \dot{\gamma} \cdot 2\pi r^2 h = \mu \cdot \frac{\omega r}{R - r} \cdot 2\pi r^2 h = 2\pi\mu\omega \cdot \frac{r^3 h}{R - r} \tag{50}$$

The cone part:

$$\tau_{cone} = \frac{\sqrt{2}\pi\mu \cdot \omega r^4}{4\delta_0 + 2r} \tag{51}$$

The total torque:

$$\tau_{total} = \tau_{cylinder} + \tau_{cone} = \pi\mu\omega r^3 \cdot \left(\frac{2h}{R - r} + \frac{\sqrt{2}r}{4\delta_0 + 2r}\right) \tag{52}$$

$$\mu = \frac{\sigma}{\dot{\gamma}} = \frac{\sigma \cdot (R - r)}{\omega \cdot r} \tag{53}$$

$$\therefore \tau_{total} = \pi\omega r^3 \cdot \left(\frac{2h}{R - r} + \frac{\sqrt{2}r}{4\delta_0 + 2r}\right) \cdot \frac{\sigma \cdot (R - r)}{\omega \cdot r} = \sigma \cdot [(R - r) \cdot \pi \cdot R^2 \cdot \left(\frac{2h}{R - r} + \frac{\sqrt{2}r}{4\delta_0 + 2r}\right)] \tag{54}$$

The parameter $1/[(R - r) \cdot \pi \cdot R^2 \cdot \left(\frac{2h}{R-r} + \frac{\sqrt{2}r}{4\delta_0+2r}\right)]$ can be calculated as the relationship between the shear stress and the toque, which is 440.69 Pa/mNm.